



# LUND UNIVERSITY

## Advanced Laser-based Multi-scalar Imaging for Flame Structure Visualization towards a Deepened Understanding of Premixed Turbulent Combustion

Zhou, Bo

2015

[Link to publication](#)

*Citation for published version (APA):*

Zhou, B. (2015). *Advanced Laser-based Multi-scalar Imaging for Flame Structure Visualization towards a Deepened Understanding of Premixed Turbulent Combustion*. [Doctoral Thesis (compilation), Combustion Physics].

*Total number of authors:*

1

**General rights**

Unless other specific re-use rights are stated the following general rights apply:

Copyright and moral rights for the publications made accessible in the public portal are retained by the authors and/or other copyright owners and it is a condition of accessing publications that users recognise and abide by the legal requirements associated with these rights.

- Users may download and print one copy of any publication from the public portal for the purpose of private study or research.
- You may not further distribute the material or use it for any profit-making activity or commercial gain
- You may freely distribute the URL identifying the publication in the public portal

Read more about Creative commons licenses: <https://creativecommons.org/licenses/>

**Take down policy**

If you believe that this document breaches copyright please contact us providing details, and we will remove access to the work immediately and investigate your claim.

LUND UNIVERSITY

PO Box 117  
221 00 Lund  
+46 46-222 00 00

Advanced Laser-based Multi-scalar Imaging for Flame  
Structure Visualization towards a deepened  
Understanding of Premixed Turbulent Combustion

Doctoral Dissertation

Bo Zhou

Division of Combustion Physics  
Department of Physics



LUND UNIVERSITY

© Bo Zhou

Printed at Tryckeriet i E-huset, Lund, Sweden

January 2015

Lund Reports on Combustion Physics, LRCP-180

ISSN1102-8718

ISRN LUTFD2/TFCP-180-SE

ISBN(print) 978-91-7623-227-9

ISBN(pdf) 978-91-7623-228-6

Bo Zhou

Division of Combustion Physics, Lund University

P.O. Box 118

SE-221 00 Lund, Sweden



*To my family, my parents and grandparents*

和靜清寂

# Abstract

The work presented in the thesis concerns the developments of laser-based diagnostics and its application to the study of turbulent premixed combustion.

The diagnostic developments, mainly concerned with planar laser-induced fluorescence (PLIF), are intended to provide instantaneous visualization of the key species originating from the combustion processes involved in the burning of hydrocarbons and nitrogen-containing fuels under turbulent conditions. For the burning of hydrocarbons, these species include HCO, hot O<sub>2</sub> etc. and for the burning of nitrogen-containing fuels, these include NH<sub>3</sub>, NH and CN. In connection with this, the potential for instantaneous temperature mapping using two-line atomic LIF (TLIF) with a novel seeding system are also demonstrated.

The study of turbulent premixed combustion involves simultaneous imaging of such scalars as HCO, CH, CH<sub>2</sub>O and OH as well as temperature. Laboratory-scale premixed CH<sub>4</sub>/air flames stabilized on the Lund University Pilot Jet burner (LUPJ) and the Low-Swirl Burner (LSB) were investigated over a wide operational range and various combustion regimes. The results from both the LUPJ and the LSB flames provide the first experimental evidences for its being possible to appreciably broaden the reaction zone of premixed flames can be significantly broadened through rapid turbulence mixing, the results being verified by observations of broadened/distributed short-lived radicals, HCO and/or CH. The observations obtained for the two clearly different burner configurations suggest that distributed reactions can be a common combustion mode. For the LUPJ flames, the dependence of the reaction zone broadening on the jet speed and the equivalent ratio was investigated systematically. Spatial correlations between the scalars that were measured were investigated, and the detailed local flame structures with and without the presence of distributed reactions were analyzed and compared. It was found that having a temperature above ~ 1000 K is important for sustaining the distributed reactions. The build-up of radical pools through rapid turbulence transport in regions containing (intermediate) reactants was found to be responsible for the distributed reactions occurring. In addition, a study of Mild combustion that has similarities with the distributed reaction concept was

performed using optical diagnostics. Certain insights concerning the reaction zone structure of Mild combustion are discussed.

# List of papers

- I. **B. Zhou**, J. Kiefer, J. Zetterberg, Z.S. Li and M. Aldén, *Strategy for PLIF single-shot HCO imaging in turbulent methane/air flames*, Combustion and Flame 161, 1566-1574 (2014).
- II. J. Kiefer, **B. Zhou**, J. Zetterberg, Z.S. Li and M. Aldén, *Laser-induced fluorescence detection of hot molecular oxygen using a multimode alexandrite laser*, Applied Spectroscopy 68, 1266-1273 (2014).
- III. **B. Zhou**, C. Brackmann, Z.S. Li and M. Aldén, *Development and application of CN PLIF for single-shot imaging in turbulent flames*, Combustion and Flame, 162, 368-374 (2015)
- IV. C. Brackmann, O. Hole, **B. Zhou**, Z.S. Li and M. Aldén, *Characterization of ammonia two-photo laser-induced fluorescence for gas-phase diagnostics*, Applied Physics B-Lasers and Optics 115, 23-33 (2014).
- V. **B. Zhou**, C. Brackmann, Z.S. Li, M. Aldén and X.S. Bai, *Simultaneous multi-species and temperature visualization of premixed flames in distributed reaction zone regime*, Proceedings of the Combustion Institute, 35, 1409-1416, (2015)
- VI. **B. Zhou**, C. Brackmann, Q. Li, Z.K. Wang, P. Petersson, Z.S. Li, M. Aldén, and X.S. Bai, *Distributed reaction in highly turbulent premixed methane/air flames: Part I. Flame structure characterization*, Combustion and Flame, In press, 2014

- VII. **B. Zhou**, C. Brackmann, Z.S. Li, M. Aldén and X.S. Bai, *Multi-scalar imaging of small-scale structures in turbulent premixed flames from flamelet to distributed reactions*, submitted to Combustion and Flame, 2014
- VIII. **B. Zhou**, Q. Li, Y. He, P. Petersson, Z.S. Li, M. Aldén, and X.S. Bai, *Visualization of multi-regime turbulent combustion in swirl-stabilized lean premixed flames*, submitted to Combustion and Flame, 2014
- IX. C. Brackmann, **B. Zhou**, Z.S. Li and M. Aldén, *Strategies for quantitative planar laser-induced fluorescence of NH radicals in flames*, accepted by 9<sup>th</sup> Mediterranean Combustion Symposium for oral presentation, 2014

## Related work

- A. R. Whiddon, **B. Zhou**, J. Borggren, Z.S. Li and M. Aldén, *Vapor phase Indium seeding system using Tri-methyl-indium suitable for quantitative combustion diagnostics*, to be submitted.
- B. **B. Zhou**, M. Costa, Z.S. Li and M. Aldén, *Characteristics of flameless combustion in a laboratory combustor using optical diagnostics*, in manuscript.
- C. **B. Zhou**, Z.W. Sun, Z.S. Li, B. Li, Y. He, Z. Wang, S. Lindecrantz, H. Nilsson, H. Hartman and M. Aldén, *High resolution emission spectroscopy in 1800-6000 cm<sup>-1</sup> from lifted one-dimension laminar CH<sub>4</sub>/O<sub>2</sub>/N<sub>2</sub> flames*, to be submitted.
- D. J. Kiefer, **B. Zhou**, Z.S. Li and M. Aldén, *Impact of plasmas dynamics on equivalence ratio measurements by laser-induced breakdown spectroscopy*, submitted to Applied Optics, 2014
- E. C. Brackmann, V.A. Alekseev, **B. Zhou**, E. Nordström, P-E. Bengtsson, Z.S. Li, M. Aldén and A. Konnov, *Structures of premixed ammonia/air flames at atmospheric pressure – laser diagnostics and kinetic modeling*, submitted to Combustion and Flame, 2014

- F. H. Carlsson, E. Nordström, A. Bohlin, Y. Wu, **B. Zhou**, Z.S. Li, M. Aldén, P-E. Bengtsson and X.S. Bai, *Numerical and experimental study of flame propagation and quenching of lean premixed turbulent low swirl flames at different Reynolds numbers*, submitted to Combustion and Flame, 2014
- G. Q. Li, **B. Zhou**, Z.K. Wang, Z.S. Li, C. Brackmann, P. Petersson, M. Richter, Z.G. Wang, X.S. Bai and M. Aldén, *Flow field characteristics in axisymmetric highly turbulent premixed reacting flows*, to be submitted
- H. C. Brackmann, **B. Zhou**, P. Samuelsson, V.A. Alekseev, A. Konnov, Z.S. Li and M. Aldén, *NH<sub>2</sub> detection in fuel-nitrogen combustion using an Alexandrite laser*, to be submitted



# Contents

Abstract .....	i
List of papers .....	iii
Contents.....	vii
Abbreviations .....	ix
Chapter 1 Introduction .....	1
Chapter 2 Equipment.....	3
2.1 Lasers .....	3
2.1.1 Nd:YAG Laser .....	3
2.1.2 Dye Laser .....	3
2.1.3 Solid-state Alexandrite Laser.....	4
2.2 Detectors .....	4
2.2.1 ICCD Cameras .....	4
2.2.2 Spectrometers .....	5
2.3 Laboratory Combustors .....	6
2.3.1 Lund University Piloted Jet Burner (LUPJ).....	6
2.3.2 Low-swirl Burner (LSB) .....	7
2.3.3 Flameless Combustor .....	7
Chapter 3 Turbulent Premixed Combustion.....	9
3.1 Flame Chemistry.....	9
3.2 Turbulent Scales and Combustion Regimes.....	12
3.3 Limits of the Combustion Regime Diagram .....	16
Chapter 4 Laser Techniques and Their Developments for Turbulent Combustion Diagnostic .....	19
4.1 Introduction .....	19
4.2 Planar Laser-induced Fluorescence.....	20
4.2.1 Formyl (HCO) radical .....	22
4.2.2 Hot Oxygen Molecule (O <sub>2</sub> ) .....	26
4.2.3 Cyano (CN) radical.....	28

4.2.4 Gaseous Ammonia ( $\text{NH}_3$ ) .....	32
4.2.5 Nitrogen Monohydrate (NH) Radical.....	35
4.2.6 Two-line Atomic LIF (TLIF) of Indium .....	38
4.3 Concentration Quantification from a LIF signal.....	41
4.3.1 General discussion .....	41
4.3.2 $\text{CH}_2\text{O}$ Quantification .....	44
4.4 Laser Rayleigh Scattering Thermometry .....	45
4.5 Laser Doppler Anemometry.....	46
 Chapter 5 Understanding of Turbulent Premixed Combustion in Different Regimes.....	47
5.1 Turbulent Premixed Jet Flames (LUPJ Flames) .....	48
5.1.1 Flow Field Characteristics.....	50
5.1.2 Multi-scalar Visualizations: Laser diagnostics .....	53
5.1.3 Multi-scalar Visualizations: Jet speed dependence .....	54
5.1.4 Multi-scalar Visualizations: $\Phi$ dependence .....	63
5.1.5 Flame tip structures .....	65
5.1.6 Flame front Markers.....	67
5.1.7 Small-scale flame structures .....	70
5.2 Lean Premixed Low-swirl Flames.....	73
5.3 Concluding Remarks of Distributed Reactions in Turbulent Premixed Flames.....	77
5.4 Similarities with Other Combustion Concepts .....	81
 Chapter 6 Summary and Outlook.....	87
Acknowledgements.....	91
Appendix.....	95
References .....	99
Summary of papers.....	111

# Abbreviations

<b>CDC</b>	Colorless Distributed Combustion	<b>LUPJ</b>	Lund University Piloted Jet burner
<b>DNS</b>	Direct Numerical Simulation	<b>LIF</b>	Laser-induced Fluorescence
<b>DRZ</b>	Distributed Reaction Zone	<b>LSB</b>	Low-swirl Burner
<b>EGR</b>	Exhaust Gas Recirculation	<b>LSF</b>	Low-swirl Stabilized Lean Premixed Flame
<b>FC</b>	Flame Chemiluminescence	<b>MCP</b>	Micro-Channel Plate
<b>FLOX</b>	Flameless Oxidation	<b>MIE</b>	Minimum Ignition Energy
<b>FTE</b>	Flame Trailing Edge	<b>MILD</b>	Moderate or Intense Low-oxygen Dilution combustion
<b>HAB</b>	Height above burner	<b>Nd:YAG</b>	Neodymium-doped Yttrium Aluminium Garnett
<b>HiCOT</b>	High Temperature Combustion Technology	<b>OD</b>	Outer Diameter
<b>HITAC</b>	High Temperature Air Combustion	<b>OPO</b>	Optical Parametric Oscillator
<b>HRR</b>	Heat Release Rate	<b>QE</b>	Quantum efficiency
<b>ICCD</b>	Intensified Charge-Coupled Device	<b>RST</b>	Rayleigh Scattering Thermometry
<b>ID</b>	Inner Diameter	<b>SE</b>	Stimulated Emission
<b>JPDF</b>	Joint Probability Density Function	<b>SNR</b>	Signal-to-Noise Ratio
<b>K<sub>a</sub></b>	Karlovitz number	<b>TLIF</b>	Two Line Atomic LIF
<b>LDA</b>	Laser Doppler Anemometry	<b>TRZ</b>	Thin Reaction Zone
<b>LES</b>	Large Eddy Simulation	<b>TMI</b>	Trimethylindium
<b>LFF</b>	Leading Flame Front	<b>VUV</b>	Vacuum Ultraviolet
<b>LiDAR</b>	Light Detection and Ranging		

# Nomenclature

$A_{21}$	Einstein coefficient for spontaneous emission	$T_u$	Temperature of unburnt reactants
$B_{21}$	Einstein coefficient for absorption	$t_\eta$	Kolmogorov time scale
$D$	Thermal diffusivity	$t_0$	Integral time scale
$D_m$	Mass diffusivity	$t_c$	Chemical time scale
$Da$	Damköhler number	$U$	Axial velocity of jet flow
$d$	Jet diameter	$\nu'$	Root-mean-square (rms) of streamwise velocity, i.e. turbulent velocity
$f$	Boltzmann factor/Focus length	$\nu$	Kinematic viscosity
$f_\#$	f-number	$\delta_L$	Thermal thickness
$g$	Statistical weight of energy state	$\delta_r$	Reaction zone thickness
$h$	Planck's constant	$\sigma$	Rayleigh scattering cross sections
$l$	Characteristic length scale of flow	$\Phi$	Equivalence ratio
$l_0$	Integral length scale	$\chi$	Mole fraction of species
$l_T$	Taylor scale		
$l_\eta$	Kolmogorov scale		
$k$	Wavenumber, $2\pi/l$		
$Q$	Quenching rate		
$Re_{jet}$	Reynolds number at jet exit		
$Re_t$	Turbulent Reynolds number		
$S_L$	Laminar flame speed		
$T_b$	Temperature of burnt products		

# Chapter 1

## Introduction

The utilization by human beings of energy extracted from combustion has a long history [1]. A dramatic expansion of human activities occurred since then. Nowadays, combustion represents about 90% of the global energy production and in the foreseeable future will surely be an indispensable source of energy in the continuous development of human civilization [2]. However, combustion also brings environmental issues due to the polluting by-products. Public awakening to the effects of combustion pollutions has led to the demand for improvements in combustion efficiency and an accompanying reduction in the production of pollution. To fulfill this, it is crucial to understand the fundamentals of combustion processes. Despite the impressive long period of time during which human beings have attempted to control combustion, our knowledge of combustion processes is still only very limited. One of the major reasons roots in the multi-scale nature of combustion [3]. Practical combustion processes typically consist of thousands of chemical reactions and species involved that interact with turbulence within a continuous spectrum of both time and length scales. Accordingly, temporally and spatially resolved techniques are required in order to understand combustion processes. Due to the advantages of high temporal and spatial resolution, laser-based diagnostics has been employed to deepen the understanding of combustion processes. In contrast to probe techniques, critical parameters such as temperature, species concentration and velocity etc. can be obtained both non-intrusively and remotely. Since turbulent combustion is inherently three-dimensional, the visualization ability further strengthens the uniqueness of laser-based diagnostics as a valuable tool for combustion research.

The work presented in the thesis concerns the development of laser-based techniques and their applications within the context of turbulent combustion. The results obtained provide insight into the flame structures involved in different turbulent combustion regimes. In particular, experimental evidence for the

distributed reaction zone through strong turbulence/flame interaction was documented for the first time. The outline of the thesis is described briefly as follows. The instruments employed are presented in Chapter 2. A brief introduction to turbulent premixed combustion is given in Chapter 3. The results obtained are discussed in Chapter 4 and 5; Chapter 4 being concerned with the development of laser based techniques and Chapter 5 with their use in the investigation of turbulent premixed combustion. A summary of the work conducted and the outlook for further researches are provided in Chapter 6.

# **Chapter 2**

## **Equipment**

**I**n this chapter, a brief presentation of the equipment employed in the present study is provided. In Section 2.1, various laser systems are described, followed by the description in Section 2.2 of detector systems employed and in Section 2.3 of the laboratory combustors involved.

### **2.1 Lasers**

#### **2.1.1 Nd:YAG Laser**

The Nd:YAG laser is a solid-state laser named after its lasing medium of the neodymium-doped yttrium aluminum garnet crystal ( $\text{Nd:Y}_3\text{Al}_5\text{O}_{12}$ ) giving a fixed-frequency radiation at 1064 nm. Higher harmonics at 532 nm, 355 nm, 266 nm and 213 nm can be achieved by use of harmonic generation crystals. Species excitations, photolysis, laser Rayleigh scattering and particle imaging can be attained by use of these radiations, as will be discussed in the following chapters. In addition, the laser radiations of 532 nm or 355 nm are frequently employed as pump sources for a dye laser system or an optical parametric oscillator (OPO) system so as to achieve a broader range of wavelength operations. The Nd:YAG laser systems employed have a repetition rate of 10 Hz, and typically a  $\sim 10$  ns pulse duration and a  $\sim 1 \text{ cm}^{-1}$  line width.

#### **2.1.2 Dye Laser**

The dye laser utilizes organic dyes dissolved in liquid solutions as the lasing medium. In contrast to most of solid-state lasers, the dye laser is widely tunable typically from 390 nm to 900 nm by employing various dye solutions. Frequency-

doubling/tripling achieved through the use of harmonic generation crystals further extends the operation wavelength range of the dye laser. The dye laser system employed from Sirah (Cobra Stretch-G-2400) has an 8 ns pulse duration and a ~ 0.3 cm<sup>-1</sup> line width.

### 2.1.3 Solid-state Alexandrite Laser

The Alexandrite crystal, the common name for chromium-doped chrysoberyl, Cr<sup>3+</sup>:BeAl<sub>2</sub>O<sub>4</sub> is the lasing medium of the solid-state alexandrite laser. Being particular among most solid-state lasers, the alexandrite laser has a continuous wavelength tunability from 700 nm to 810 nm which originates from broad vibronic transitions between electronic states at an elevated temperature of ~ 400K [4, 5]. The alexandrite laser is complementary to the dye laser as dye lasing mediums typically have weak efficiency within this wavelength range whereas a solid-state alexandrite laser provides substantially stronger energy output ~250 mJ per pulse. Single-longitudinal-mode alexandrite lasers with a linewidth of ~ 60 MHz have been developed and been employed for filtered Rayleigh scattering thermometry [6] and Light detection and ranging (LiDAR) [7]. In addition to the narrow linewidth alexandrite laser, the alexandrite laser currently employed features a broad ~ 2.5 cm<sup>-1</sup> linewidth and a relatively long pulse duration of ~ 50 ns which abates the possible saturation of laser-induced fluorescence (LIF) and therefore enhances the LIF signal strength. Advantages originated from the unique characteristics of the alexandrite laser will be elaborated further in Chapter 4.2.

## 2.2 Detectors

### 2.2.1 ICCD Cameras

An intensified charge-coupled device (ICCD) integrates an image intensifier with a CCD camera. An intensifier includes a photocathode, a micro-channel plate (MCP) and a phosphor screen. For laser-based imaging measurements, the collected signals (i.e. photons) are converted into electrons by the photocathode, which are multiplied in the MCP section and then hit the phosphor screen. The phosphor translates the multiplied electrons back to photons which are read out on the CCD. This configuration of the ICCD cameras enables an ultra-fast gating of a few nanoseconds and delivers high photon-sensitivity even in the ultraviolet (UV) region. The short gating favors the detection of laser-induced signals by rejecting

background emissions, for example, from flame chemiluminescence. As shown in Figure 2-1, the quantum efficiency (QE) of the intensifier as a function of the wavelength varies with different phosphor coatings. The selection of an ICCD camera which has a QE curve optimized for the wavelength range of the detected signals is preferable particularly when the signal-to-noise ratio (SNR) of the detected species is limited.

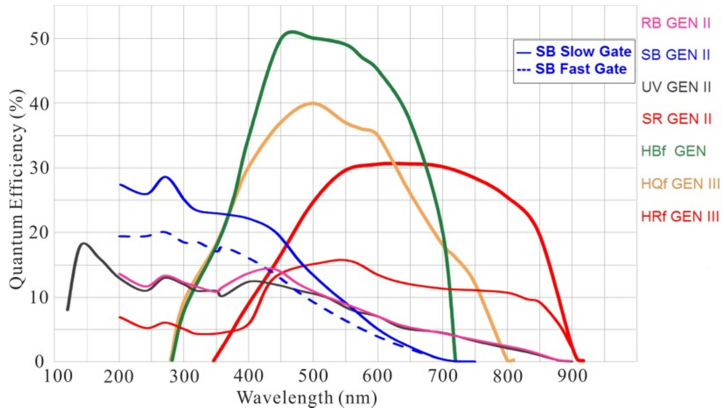


*Figure 2-1 The quantum efficiencies of intensifiers of an CCD camera with different phosphor coatings, adapted from [8].*

### 2.2.2 Spectrometers

The grating-based spectrometers employed (Acton 2300i and 2500i, Princeton Instrument) are based on the common Czerny-Turner design. The signals are collected from a narrow front slit and imaged onto the grating system which disperses the colors (i.e. the wavelengths) of the signals spatially. The spatially dispersed signals are then projected onto an ICCD camera. Accordingly, a two-dimensional spectrum is formed with one dimension being within the wavelength domain, whereas the other dimension contains spatial information. As combustion processes include numerous chemical reactions and species, spectral and spatial discriminations of detected signals are important for laser-based diagnostics, for example, LIF measurements to ensure the fidelity of the signals that are detected. Different spectral resolutions can be achieved by employing different gratings. The gratings most commonly employed in the present work are those with 150 grooves/mm and 1200 grooves/mm, giving an actual spectral resolution of 2 nm and 0.25 nm, respectively.

## 2.3 Laboratory Combustors

### 2.3.1 Lund University Piloted Jet Burner (LUPJ)

The Lund University Piloted Jet burner (LUPJ) is a hybrid McKenna-type jet burner which consists of a 1.5-mm inner-diameter (ID) stainless central nozzle having an outer-diameter (OD) of 7-mm that sits 2 mm above the surrounding 61-mm ID coflow porous plug. Mixtures are fed into the central nozzle and the coflow plug independently. A schematic plot of the LUPJ and photographs of the laminar and the turbulent jet flames stabilized on it are shown in Figure 2-2. Shielded and sustained by the hot products from the surrounding pilot coflow flame, both stable laminar flames and shear-driven highly turbulent flames can be stabilized on the jet. A series of piloted premixed highly turbulent jet flames (LUPJ series flames) stabilized on this burner were investigated using laser diagnostics in our laboratory, and the results are presented in Section 5.1.

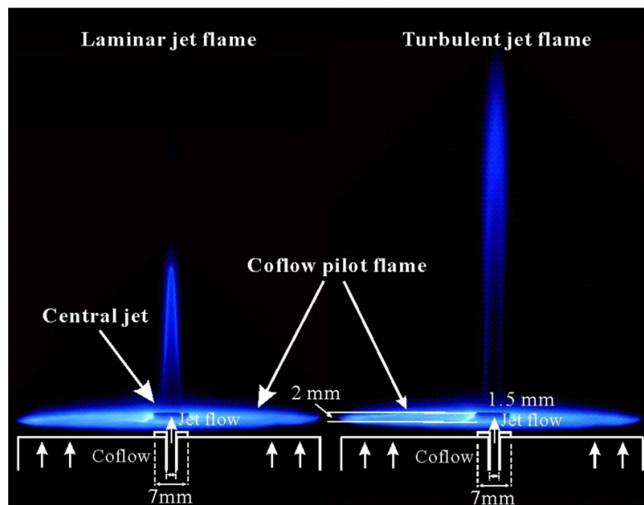


**Figure 2-2** A schematic plot of the Lund University Piloted Jet burner (LUPJ) and photographs of laminar and turbulent jet flames stabilized on it.

### 2.3.2 Low-swirl Burner (LSB)

The low-swirl burner (LSB) was originally developed by Bedat and Cheng [10, 11] to facilitate ultra-lean premixed flames which exhibit the feature of low NO<sub>x</sub> emission. The LSB employed in our laboratory [12] at Lund University was developed cooperatively with the Lawrence Berkeley National Laboratory and the Technical University Darmstadt, serving the joint purpose of establishing a collection of experimental data on turbulent premixed flames for model validation. As shown in Figure 2-3, the premixed mixtures are fed into the chamber of the LSB and then transported through perforated grids to ensure a steady laminar flow. The swirler having 50 mm OD contains eight swirl vanes in the outer part and a 38 mm ID central perforated plate so that swirl is imparted to the outer part of the flow while the central flow remains non-swirling. The exit nozzle is located at 68 mm downstream of the swirler. The lifted flames are stabilized ~ 30 mm above the nozzle exit plane regardless of inlet flow speeds. Experimental results for the LSB are presented in Section 5.2.

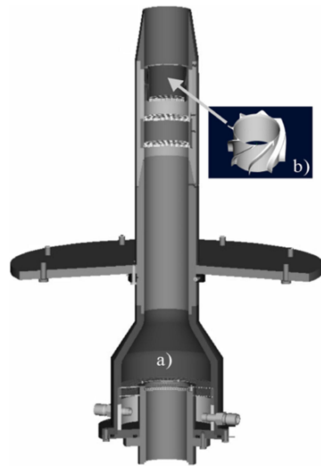


**Figure 2-3** (a) A cross-sectional view of the LSB and (b) its swirler installed at the location marked by the arrow. Reprinted from [9]

### 2.3.3 Flameless Combustor

A combustor, termed a flameless combustor was investigated in the present work. As shown in the schematic plot of Figure 2-4, the flameless combustor consists of a quartz cylinder combustion chamber having an ID of 100 mm and a length of 340 mm. The quartz cylinder was surrounded by a 30-mm thick ceramic fiber blanket to sustain the chamber temperature during operation. The air was preheated to 673 K and was issued from the central orifice (10 mm ID) located at the top of the combustion chamber. Surrounding the central orifice are 16 small orifices with 2 mm ID positioned axial-symmetrically on a circle with a radius of 15 mm for fuel (i.e. methane) injection. A convergent nozzle with 150 mm in length and an angle of 15 degree is located at the bottom of the chamber serving as the exhaust gas exit. Depending on different excess levels, three distinct combustion modes can be achieved, namely a flameless combustion mode (Figure 2-4 (b)) in which the flame

emission is invisible, a conventional combustion mode (Figure 2-4 (d)) with the visible flame emission and a transition combustion mode (Figure 2-4 (c)) operated in between the former two modes. The OH<sup>\*</sup> emission of the three combustion modes are shown in Figure 2-5. During the experiment, the inlet fuel velocity is fixed at 6.2 m/s, whereas the inlet air velocities are 162.8, 126.5 and 96.2 m/s to achieve the conventional, transition and flameless combustion modes, respectively. The experimental results obtained for the flameless combustor are presented in Section 5.4.

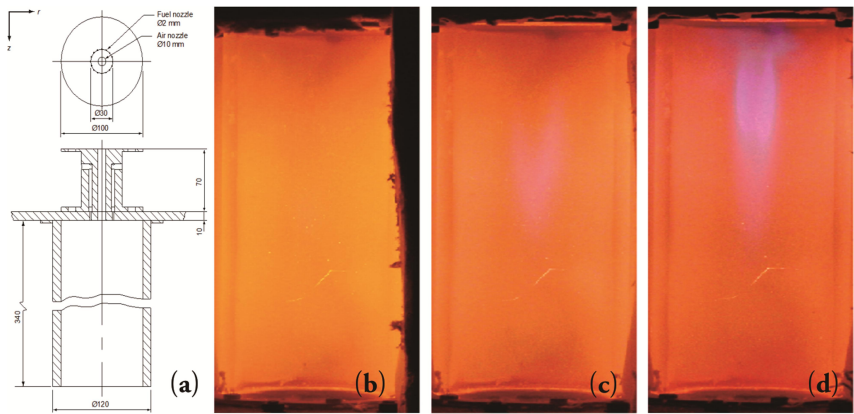


**Figure 2-4** (a) Schematic of a flameless combustor (b-c) three operational flame conditions: (b) the flameless mode (d) the conventional flame mode with visible flame emission and (c) a transient mode between the former two combustion modes.

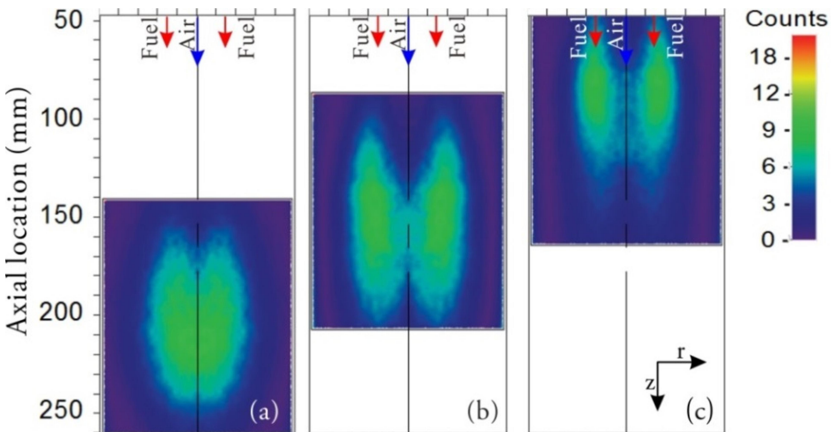


**Figure 2-5** OH<sup>\*</sup> emission as measured for (a) the flameless mode (b) the transient mode and (c) the conventional mode of flames, as adapted from [13].

# Chapter 3

## Turbulent Premixed Combustion

**D**espite the turbulence phenomena being so widespread in nature, from, for example, the terrestrial atmospheric circulation to a smoke of a cigarette, a precise definition of turbulence is difficult to be arrived at because of its chaotic nature. Several definitions of turbulence based on more or less intuitive characterizations have been proposed. For example, Hinze [14] suggested a definition of turbulence as follows:

*“Turbulence fluid motion is an irregular condition of the flow in which the various quantities show a random variation with time and space coordinates, so that statistically distinct average values can be discerned.”*

Flow motions in the context of turbulence are expected to be sensitive to both the initial and the boundary conditions and are chaotically evolving over a large range of length and time scales. In contrast to the diffusion-dominated cases encountered in the laminar flows, turbulence enhances the diffusion processes of, e.g. heat and species. Also, when combustion is engaged in, the occurrence of reactions on various chemical time scales and the associated heat-release effects make the interaction between turbulence and combustion virtually intractable. To obtain a better understanding of such interaction requires sophisticated investigations of both turbulence and combustion to be carried out. In this chapter, discussions will be limited to those of turbulent premixed combustion. A brief introduction to flame chemistry is provided in section 3.1 which is followed by a discussion of turbulence/chemistry interaction under different combustion regimes.

### 3.1 Flame Chemistry

The complete global single-step reaction of methane, the simplest hydrocarbon fuel, with oxygen can be expressed as:



In premixed flames, the fuel and the oxidizer are mixed prior to the occurrence of combustion. The equivalence ratio,  $\Phi$ , is introduced to quantify the fuel-to-oxidizer ratio with regard to the stoichiometric condition which is referred to as the complete reaction case. Mathematically,

$$\Phi = \frac{\text{m}_{\text{fuel}}/\text{m}_{\text{oxidizer}}}{(\text{m}_{\text{fuel}}/\text{m}_{\text{oxidizer}})_{\text{st}}} \quad (3.2),$$

where  $m$  represents the mass fraction and  $\Phi < 1$  fuel-lean conditions, conditions in which  $\Phi > 1$  being termed fuel-rich.

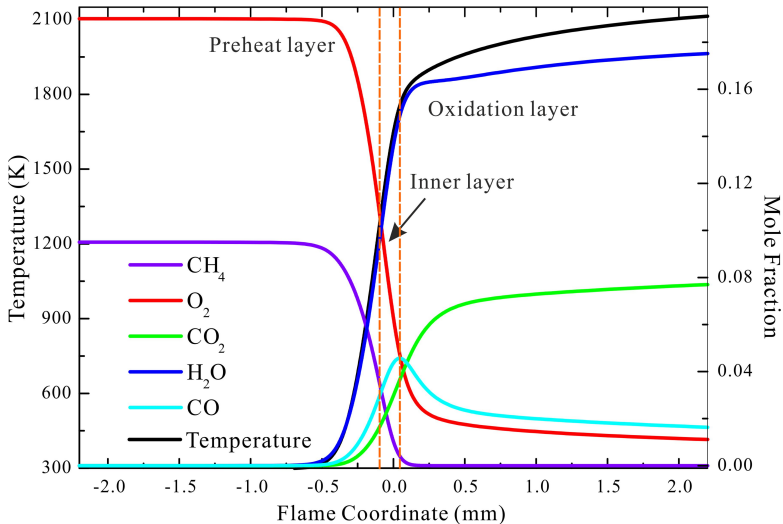


**Figure 3-1** The overall structure of a planar free-propagating methane/air stoichiometric flame.

The overall structure of a planar free-propagating methane/air stoichiometric flame is shown in Figure 3-1. At the center of the flame coordinate,  $\text{CH}_4$  and  $\text{O}_2$  are consumed rapidly, resulting in the formation of combustion products such as  $\text{H}_2\text{O}$  and  $\text{CO}_2$  along with a dramatic increase in temperature. This process occurs in a thin region, typically less than 1 mm in thickness, termed the inner layer or the reaction zone, where the consumption of fuel and radicals occurs [15]. The temperature of the inner layer corresponds approximately to the cross-over temperature above which chain-branching reactions dominate over chain-terminating reactions so that reactions are accelerated. Upstream of the inner layer, there is a layer termed preheat layer in which reactants are preheated by the heat

diffused and conducted from the reaction zone. A very limited number of reactions, however, occur in this region since there the temperature is typically lower than the cross-over temperature so that reactive radicals are quickly consumed. Slightly downstream of the reaction zone, stable species such as H<sub>2</sub> and CO are formed and continue to be oxidized in the oxidation layer since the temperature is high. In short, the major reactions associated with large amounts of heat release occur in the thin reaction zone less than 1 mm in thickness which separates the unburnt from the hot combustion products. The internal structure of the thin reaction zone is further illustrated in Figure 3-2. At the start of the reaction zone, fuel starts to decompose along with the production of CH<sub>2</sub>O. Later on, the formation of reactive radicals like OH accelerates reactions, leading to CH<sub>2</sub>O together with other (intermediate) reactants being quickly consumed, and to a peak of the heat release rate (HRR) at the center of the reaction zone. As can be seen in Figure 3-2, profiles of HCO and CH and of the OH gradient correlate well with the profile of HRR, there being a maximum discrepancy of less than 100  $\mu\text{m}$ . In turbulent premixed flames, these quantities are referred to frequently as the flame front markers which reflect the primary HRR. It has also been demonstrated in laminar flames that the formation of HCO can be mainly attributed to the reaction [16]



Because of the experimental feasibility, the product of OH and CH<sub>2</sub>O has been proposed to mimic HCO and therefore indirectly correlates with the HRR. Detail discussions of this matter are presented in Section 5.1.6.

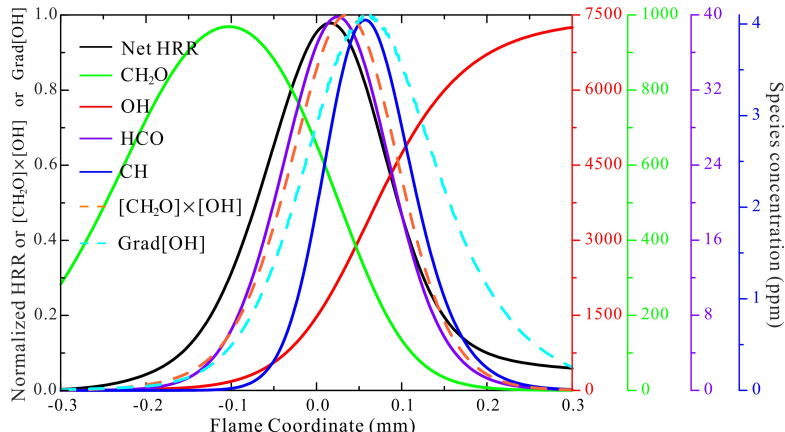


**Figure 3-2** Profiles of different species, the product of CH<sub>2</sub>O and OH, the net heat release rate (HRR) and the OH gradient in the thin reaction zone.

Two intrinsic quantities, the laminar flame speed,  $S_L$  and flame thickness,  $\delta$ , are commonly employed in quantifying unstretched laminar premixed flames.  $S_L$  represents the speed at which the unstretched flame front propagates towards the unburnt region. Experimental methods such as the heat flux method [17] and the slot-burner method [18] have been developed for measuring  $S_L$  based on the idea that the velocity of the incoming flow normal to the flame front balances with  $S_L$ . The flame thickness  $\delta$  represents the characteristic length scale for flame chemistry. Two thicknesses, i.e. the thermal thickness  $\delta_L$  and the reaction zone thickness  $\delta_r$  can be experimentally determined. The thermal thickness, also termed the flame thickness is defined as

$$\delta_L = \frac{T_b - T_u}{\max \left| \frac{dT}{dx} \right|} \quad (3.4),$$

where  $T_b$  and  $T_u$  are the temperature of the burnt and the unburnt regions of a flame, respectively.  $\delta_L$  can be approximated as the sum of the thicknesses of the reaction zone and preheat layer in laminar flames.  $\delta_r$  is experimentally estimated on the basis of the thickness of the flame front markers, such as CH and HCO.  $S_L$  and  $\delta_L$  are related to one another in terms of the thermal diffusivity  $D$ , through  $S_L \sim D/\delta_L$  and the chemical time scale  $\tau_c = \delta_L / S_L \sim \delta_L^2 / D$ .

## 3.2 Turbulent Scales and Combustion Regimes

As quoted from Richardson [19] regarding turbulence flows,

*“Big whirls have little whirls, which feed on their velocity. And little whirls have lesser whirls, and so on to viscosity in the molecular sense.”*

This reflects the energy cascade concept in regard to turbulence flows where the turbulent kinetic energy contained in large scales (or eddies) is transferred successively to the smaller and smaller scales until the energy can be effectively dissipated by molecular viscosity. How the turbulent kinetic energy distributed among the scales of different sizes is depicted by the turbulent energy spectrum as shown in Figure 3-3. Conventionally, the energy spectrum  $E(k)$  is plotted as a function of the wavenumber,  $k$ , which is defined as  $k=2\pi/\ell$ , where  $\ell$  is the characteristic length scale of the flow. The energy spectrum can be divided by  $\ell_{EI}$  (i.e.  $k_{EI}$  in wavenumber) into two ranges, i.e. the energy containing range and the universal equilibrium range. In the energy containing range, the eddies are large in size and might be anisotropic, containing the majority of the turbulent kinetic energy. The integral scale,  $\ell_0$ , in this range represents the length scale of the

turbulent flow that contains the most turbulent kinetic energy. In the universal equilibrium range, the motions of small-scale eddies are assumed to be statistically isotropic. The smallest scale in this range is termed the Kolmogorov scale  $\ell_\eta$ , scales below which will be smeared out swiftly by viscous dissipation. Two subranges, the inertial subrange and the dissipation subrange are further demarcated by  $\ell_{DI}$ . It is argued that the eddy motions in the dissipation subrange sense viscous effects, whereas the motions in the inertial subrange are barely affected by molecular viscosity. The Taylor length scale,  $\ell_T$  can also be introduced, its often being referred to as the length scale between  $\ell_{EI}$  and  $\ell_{DI}$  which delimits the length scales which are either resolved or modeled in large-eddy simulation (LES).

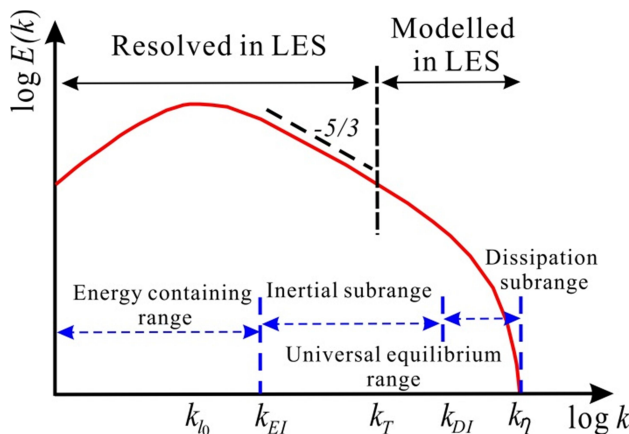


**Figure 3-3** The turbulent energy spectrum which indicates the turbulent kinetic energy distribution over different length scales (or wavenumbers).

In addition to the aforementioned turbulence length scales, a few dimensionless quantities are also frequently utilized. The Reynolds number ( $Re$ ) is defined as

$$Re = \frac{U \times l}{\nu} \quad (3.5),$$

where  $U$  is the velocity and  $\nu$  the kinematic viscosity. In calculating the turbulent Reynolds number ( $Re_t$ ), substituting  $\nu=S_L \times \delta_L$ ,  $U=\bar{u}$  and  $l=\ell_0$  into Equation (3.5) gives

$$Re_t = (\bar{u} \times \ell_0) / (S_L \times \delta_L) \quad (3.6),$$

where the turbulence velocity is represented by the root-mean-square velocity ( $\bar{u}$ ) of the flow. In order to project the associated quantities to the same context as the

Borghi diagram which will be discussed later, the kinematic viscosity  $\nu$  is estimated as  $S_L \times \delta_L$  which is approximately equal to the kinematic viscosity at a flame temperature  $\sim 1800$  K. On the basis of the dimensional analysis, the Kolmogorov length scale  $\ell_\eta$  and the Taylor length scale  $\ell_T$  can be approximated from the integral scale as

$$\ell_\eta \sim \ell_0 \times \text{Re}_t^{-3/4} \quad (3.7) \text{ and}$$

$$\ell_T \sim \ell_0 \times \text{Re}_t^{-1/2} \quad (3.8).$$

Two other dimensionless quantities, the Karlovitz number ( $Ka$ ) and the Damköller numbers ( $Da$ ) are also introduced in order to quantify the extent of the turbulence/chemistry interaction.  $Ka$  is defined as the ratio of the chemical time scale,  $\tau_c$ , to the Kolmogorov time scale,  $\tau_\eta$  (i.e. the smallest turbulence time scale).  $Da$  is the ratio of the integral time scale  $\tau_0$  (i.e. the time scale associated with the integral length scale) to  $\tau_c$ . Mathematically,

$$Ka \equiv \tau_c / \tau_\eta = \{(u'/S_L)^3 \times (\delta_L / \ell_0)\}^{1/2} \quad (3.9) \text{ and}$$

$$Da \equiv \tau_0 / \tau_c = \text{Re}_t^{1/2} / Ka \quad (3.10).$$

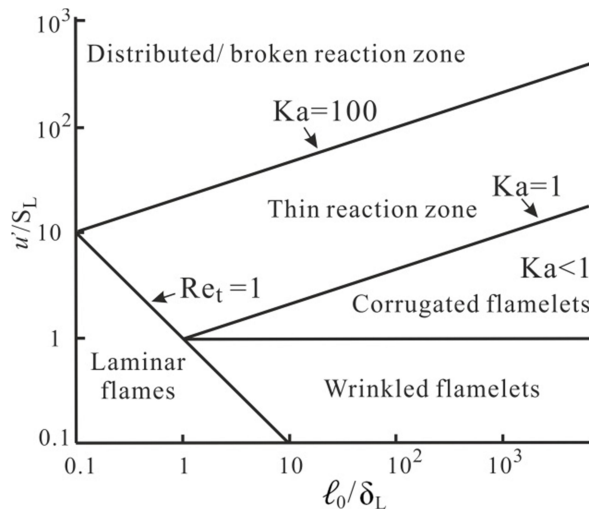


**Figure 3-4** The Borghi diagram pertaining to premixed turbulent combustion.

A diagram defining the regimes of premixed turbulent combustion using the velocity ( $u/S_L$ ) and the length scale ( $\ell_0/\delta_L$ ) ratios was proposed by Borghi [20] and was later modified by Peters [21], known as the Borghi diagram shown in Figure

3-4. Turbulent premixed flames occur in the region in which  $Re_t > 1$ , for which several turbulence combustion regimes have been proposed as listed in the following:

- **Flamelet regimes ( $Ka < 1$ )**

With  $Ka < 1$ , the Kolmogorov length scale is larger than the flame thickness, therefore the smallest eddies are not able to affect the internal structure of the thin flame front. The flame front appears to be solely wrinkled by the presence of turbulence. In the corrugated flamelet regime, the wrinkling of the flame front is increased, and pockets can be formed due to flame front interactions. As the flame front is typically thin for flames in the flamelet regimes, the laminar flamelet concept has been proposed and been widely applied in the numerical modeling of turbulent flames [22, 23]. An important assumption for this concept is that the fresh unburnt and burnt gases are separated by a thin reaction zone layer where major reactions take place. Consequently, local flame front structures in turbulent flames can be seen as a laminar flamelet. The models developed based on the flamelet concept have been reviewed in Ref. [24].

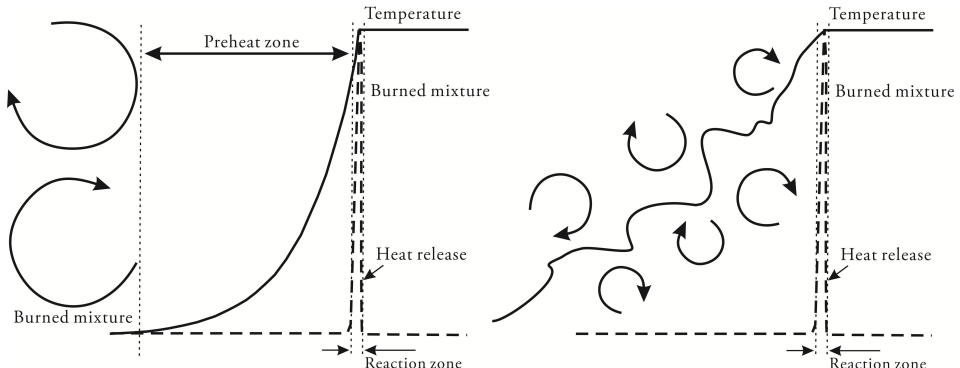


**Figure 3-5** Schematic of the flame front interacting with eddies in the flamelet (left) and the TRZ regimes (right), as modified from [25].

- **Thin reaction zone (TRZ) regime ( $1 < Ka < 100$ )**

The line  $Ka=1$  is called the *Klimov-Williams* criterion, which states a boundary condition in which the Kolmogorov length is equal to the flame thickness. The upper boundary  $Ka=100$  has been estimated by Peters who considered the reaction zone thickness  $\delta_r$  of a  $\text{CH}_4/\text{air}$  flame to be about one-tenth

of the flame thickness  $\delta_L$  [15]. At  $Ka=100$ , the  $\ell_\eta$  is equal to  $\delta_r$ . Accordingly, for  $1 < Ka < 100$ , the flame front can be expected to be distorted by turbulence. Flames with a thickened flame preheat layer and a thickened thermal layer in the TRZ regime have been found in experiments reported on [26-28]. However, both experimental observations [29-34] and direct numerical simulations [35, 36] indicate the reaction zone to remain thin in this regime, extending the applicability of the flamelet concept to the region beyond the *Klimov-Williams* criterion. Schematic of the flame front interacting with turbulent eddies in the flamelet and the TRZ regime is shown in Figure 3-5.

- ***Distributed/broken reaction zone regime ( $Ka>100$ )***

If  $Ka>100$ , the Kolmogorov scale is smaller than the reaction zone thickness. Therefore, the reaction zone can be expected to be distorted by the penetration of small eddies so that a broadened or broken reaction zone might be expected if a flame can be properly sustained. The present thesis prefers to use the term “distributed reaction zone (DRZ)” regime. The DRZ regime is relatively unexplored both experimentally and numerically, whereas theoretical predication of combustion in this regime have been presented in several pioneering works [37-39]. In brief, it has been characterized as (1) the elimination of the sharp interface between the unburnt and the combustion products owing to the rapid turbulence-dominated mixing; (2) the relatively broadened heat-release region in which the local burning rate is reduced; and consequently (3) the reduced maximum flame temperature and homogenized temperature field. In the present thesis, experimental investigations of flames in the DRZ regime have been conducted. The results and discussions are presented in Chapter 5.

### 3.3 Limits of the Combustion Regime Diagram

The Borghi diagram is useful as a rule of thumb, but the regimes demarcated in the diagram are based solely on a qualitative analysis which cannot be interpreted as a precise guidance for the following reasons:

- The dimensional analysis of turbulence length scales assumes an isotropic and isothermal turbulence flow, which might not be fully valid in the case of turbulent flames.
- The heat release from the combustion processes imposes complexities on turbulence. Owing to the gas expansion, the dilation effect has been observed

as turbulence eddies are greatly weakened after passing through the flame front [40, 41]. In addition, the streamwise history effect could affect the flame structures downstream. No account is taken of such effects in the Borghi diagram.

- The estimation of the thermal thickness or the reaction zone thickness is based on an order-of-magnitude analysis. Noticeable changes could be introduced by uncertainties in the estimates of the layer thicknesses. In addition, the relationship,  $\delta_r=0.1\delta_L$  is deduced for the methane/air flames. Care should be taken when applying the  $Ka=100$  boundary to other fuels as the flame chemistry could be different.
- The Lewis number ( $Le$ ), which is defined as the ratio of thermal diffusivity ( $D$ ) to the mass diffusivity ( $D_m$ ), has been shown to have considerable effects on the local flame speed and the flame structures especially when  $Le$  deviates substantially from unity [42-45]. This has not been taken account of in delimiting the regimes in the Borghi diagram.
- The analysis of  $Ka$  is based on comparing the Kolmogorov turbulence time scale with the global chemical time scale. However, in reality turbulence scales could interact with elementary reactions each of which has its individual chemical time scale. Hints of the limitations in predicting flame behavior with use of different fuels but with the same global  $Ka$  have been demonstrated in the reference [46], in which it was proposed that the species-specific Karlovitz number could be used instead.



# Chapter 4

## Laser Techniques and Their Developments for Turbulent Combustion Diagnostic

This chapter encloses a brief introduction to a few laser-based techniques such as laser-induced fluorescence (LIF), laser Rayleigh scattering thermometry and laser Doppler anemometry. Towards the aim of being able to be utilized for turbulent combustion diagnostics, single-shot based, interference-free and high quality planar laser-induced fluorescence (PLIF) of some “new” species have been developed. These include formyl radicals ( $\text{HCO}$ ), thermally-excited hot  $\text{O}_2$  molecules, cyano radicals ( $\text{CN}$ ), gaseous ammonia ( $\text{NH}_3$ ) and nitrogen monohydrate radical ( $\text{NH}$ ) for hydrocarbon flames and flames burning nitrogen-containing fuels. In addition, two-line atomic LIF of indium as a promising tool for instantaneous temperature mapping with a novel seeding system is also presented.

### 4.1 Introduction

Combustion processes which involve numerous species are adequate with spectroscopic information. An example is presented in Figure 4-1 (a) in which a flat lifted one-dimensional  $\text{CH}_4/\text{N}_2/\text{O}_2$  flame is shown, whose flame chemiluminescence in the UV/visible spectral range and flame thermal emission in the infrared range are presented in Figure 4-1 (b) and (c), respectively. The flame chemiluminescence originates from radicals such as  $\text{OH}^*$ ,  $\text{CH}^*$  and  $\text{C}_2^*$  which are excited by extracting the excessive energy from chemical reactions and are typically not under thermal equilibrium state. In contrast to the flame chemiluminescence, the flame emission in the infrared (IR) region comes from the thermally excited molecules the vibrational states of which are thermally populated in accordance with the Boltzmann distribution at the corresponding temperature. A detail analysis of such spectra could give information such as flame temperature, the

species concentration, the equivalence ratio and the heat release regions. However, more information can be extracted from species which are not naturally irradiating. Interrogation of such species requires external excitation sources, such as lasers, to be employed. The laser wavelength can be adjusted to be coupled with, for example, the electronic transition of certain species. The species are excited by absorbing photons from laser radiation, and the subsequent de-excitation process which could occur naturally by way of spontaneous emission which releases signals to be detected. This is indeed the principle of laser-induced fluorescence (LIF). The development and application of LIF technique are presented in the next section.

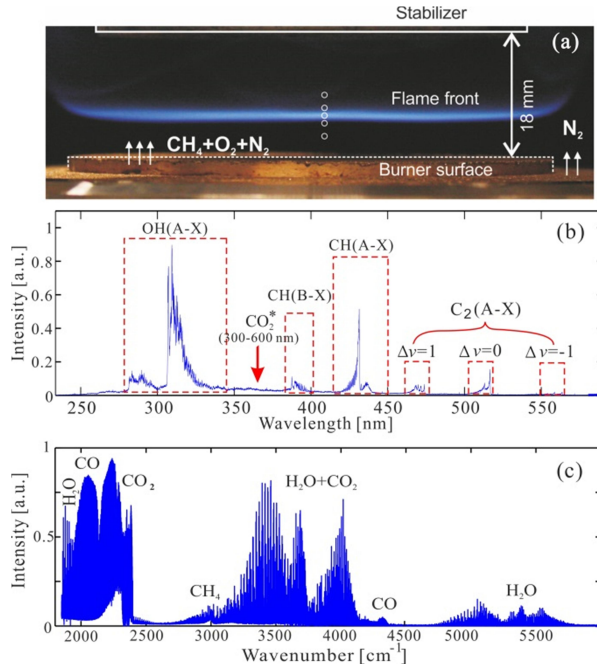


**Figure 4-1** Photograph of a flat lifted one-dimensional  $\text{CH}_4/\text{N}_2/\text{O}_2$  flame and (a) a spectrum of flame chemiluminescence in the UV/visible range recorded with a grating spectrometer (b) and of flame thermal emission in the IR range as recorded by an FTIR spectrometer.

## 4.2 Planar Laser-induced Fluorescence

Applications of the PLIF technique in combustion diagnostics were first demonstrated in the early 1980s [47]. Along with advancements of laser and

detection systems that have been made during last decades, the PLIF technique nowadays is widely employed as a valuable tool for studying turbulent combustion processes which in present work are those associated with use of hydrocarbon and nitrogen-containing fuels. Table 4-1 presents a summary of species measured using LIF presented either in the thesis or in the related work. Additional information is included concerning the corresponding excitation-detection wavelengths and achievable SNRs for an approximately 20-mm imaging size and under specific flame conditions.

**Table 4-1** A summary of the species measured using LIF in the present work.

Flames	Species	Excitation Wavelength	Lasers	Pulse Energy	Detection Wavelength	SNR
CH <sub>4</sub> /air flames	OH	~ 283 nm	Dye laser (Rh 590)	>10 mJ	~ 309 nm	>32
CH <sub>4</sub> /air flames	CH <sub>2</sub> O	355 nm	3 <sup>rd</sup> harmonic of Nd:YAG	120 mJ	360 -600 nm	>28
CH <sub>4</sub> /air flames	CH	~ 387 nm [48]	2 <sup>nd</sup> harmonic of Alexandrite	70 mJ	~431 nm	>17
CH <sub>4</sub> /air flames	HCO	259 nm [49]	3 <sup>rd</sup> harmonic of Alexandrite	15 mJ	280- 400 nm	>8
NH <sub>3</sub> doped CH <sub>4</sub> /air flames	CN	~ 359 nm	2 <sup>nd</sup> harmonic of Alexandrite	45 mJ	~ 387 nm	>20
CH <sub>4</sub> /O <sub>2</sub> flames	Hot O <sub>2</sub>	~ 257 nm [50]	3 <sup>rd</sup> harmonic of Alexandrite	14 mJ	280–420 nm	>20
NH <sub>3</sub> doped CH <sub>4</sub> /air flames	NH <sub>3</sub>	2×305 nm [51]	Dye laser (Rh 610/640)	35 mJ	~ 565 nm	-5
NH <sub>3</sub> /air flames	NH <sub>2</sub>	385.7 nm	2 <sup>nd</sup> harmonic of Alexandrite	70 mJ	400-450 nm	-5
NH <sub>3</sub> /air flames	NH	~ 303 nm	Dye laser (Rh 610/640)	30 mJ	~ 336 nm	>25
NH <sub>3</sub> /O <sub>2</sub> /N <sub>2</sub> flames	NO	225.5 nm	Dye laser (LDS 698)	4.5 mJ	230 – 400 nm	Point detection
CH <sub>4</sub> /air flames	In atom	410 nm 450 nm	CW diode lasers	10 mW	410/450 nm	Visible with naked eyes, see Section 4.2.6

In addition, a schematic plot of the major reaction paths of CH<sub>4</sub> and NH<sub>3</sub> together with their interplay from simulation at 2000 K, 1 atm condition using the

GRI3.0 mechanism [52] is presented in Figure 4-2. The species listed in Table 4-1 are marked in red, which are shown to play a vital role in CH<sub>4</sub> or NH<sub>3</sub> chemistry as well as in the fuel- and prompt-NO formation mechanisms. Based on the results from Papers I to IV and on some of the related work, the developments of the PLIF technique are presented in the following sections, aimed at providing single-shot based, interference-free and high SNR imaging of these species/radicals which later can be dedicated to studying the combustion of hydrocarbon and nitrogen-containing fuels.

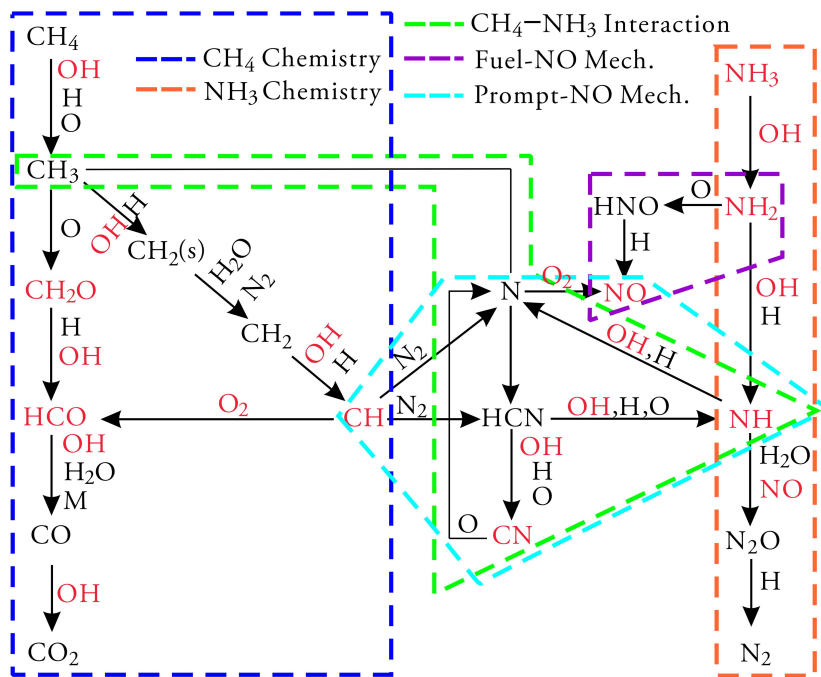


**Figure 4-2** Schematic plot of the major reaction paths of the  $\text{CH}_4$  and  $\text{NH}_3$  chemistries at 2000K, 1 atm obtained using the GRI 3.0 mechanism and a perfectly-stirred reactor in CHEMKIN. The interplay between the  $\text{CH}_4$  and  $\text{NH}_3$  chemistries together with the fuel- and prompt- $\text{NO}$  formation mechanisms are also shown.

#### 4.2.1 Formyl (HCO) radical

Heat release rate (HRR) is one of the most important parameters both for the practical design of a robust combustor and the numerical modeling of turbulent combustion. However, as a field variable, the HRR cannot be measured directly

through experiments. The analysis of laminar flame structure in section 3.1 suggests that the formyl radical, HCO could be a good indicator of HRR. Furthermore, Najm and his co-workers [16, 53, 54] have conducted numerical simulations and experiments in quasi-laminar flames. They found HCO correlate closely with local HRR over a wide operational range of hydrocarbon flames in which it was showed that ~ 60 % to 90 % of carbons flow through HCO directly or indirectly [54]. Recently, DNS results also indicated that HCO remains as a good local HRR indicator under turbulent conditions [55]. It would thus be desirable if the instantaneous HRR field can be mapped out preferably through visualizing HCO radicals. The excitation of HCO at the B-X (0,0,0)-(0,0,0) band near 259 nm offers such an opportunity. However, single-shot based HCO PLIF imaging is barely reported in the literatures because of the low fluorescence quantum yield of HCO and the comparatively weak energy output provided by conventional Nd:YAG-pumped-dye laser systems at this wavelength. The possibility of instead utilizing a multi-mode alexandrite laser for HCO excitation based on the results of Paper I is demonstrated in the following.

In the vicinity of 259 nm, the B-X (0,0,0)-(0,0,0) band of HCO exhibits a congested line structure which comprises a blend of the  $^R\text{P}_0$ ,  $^Q\text{P}_0$ ,  $^R\text{Q}_0$ ,  $^R\text{R}_0$ ,  $^R\text{R}_1$  and  $^R\text{R}_2$  branches with transitions assigned in Refs. [56, 57]. Figure 4-3 shows a set of spatially resolved emission spectra from a laminar methane/air flame stabilized on the LUPJ burner for different excitation wavelengths close to 259 nm. The ordinate of the two-dimensional spectra indicated the radial distance from the center of burner axis, whereas the abscissa corresponded to the wavelength domain. It is noteworthy that the spatial resolution across the flame front renders an additional discrimination on LIF signal, allowing for distinguishing species with fluorescence signals spectrally resided in the same wavelength range but spatially separated. Three zones along the spatial axis, i.e. an unburnt zone, a reaction zone and a product zone, can be identified as delimited by the dashed lines. The spectrum in each zone has been extracted and is presented subsequently in the subplots. One can note that at some excitation wavelengths strong interferences appear from either hot O<sub>2</sub> molecules (cf. Figure 4-3 (A) and (C)) or OH radicals (cf. Figure 4-3 (D)) in the hot coflow. The O<sub>2</sub> interference originates from excitation of the vibrational (0-7) band of the Schumann-Runge B-X system. A detailed discussion of the O<sub>2</sub> spectra will be found in section 4.2.2. To avoid O<sub>2</sub> interference within this wavelength range, the interval between two adjacent O<sub>2</sub> excitation wavelengths gives a narrow spectral window of ~ 2 Ångstroms for HCO excitation. The OH interference can also be significantly suppressed by tuning the laser wavelength off the OH transitions carefully. Figure 4-3 (B) represents a

typical HCO emission spectrum in which the interference created from OH radicals is negligible. According to simulated OH spectra using LIFBASE [58], the slight OH interference comes from the very weak transitions of the OH (4-1) and (3-0) bands, which, however, can be hardly tuned away. Fortunately, the spectrally-integrated intensity of OH interference is less than 15% that of the HCO signal intensity. In PLIF imaging, this interference is even negligible significant due to the limit resolution of the spectrograph, which shows higher signals for such species as OH, with broader spatial distribution than that if the thin HCO layer. Comparing different excitation wavelengths which give negligible interference, excitation at 259.004 nm gives the maximal signals and therefore is chosen as the optimal excitation wavelength for the experimental system being employed.

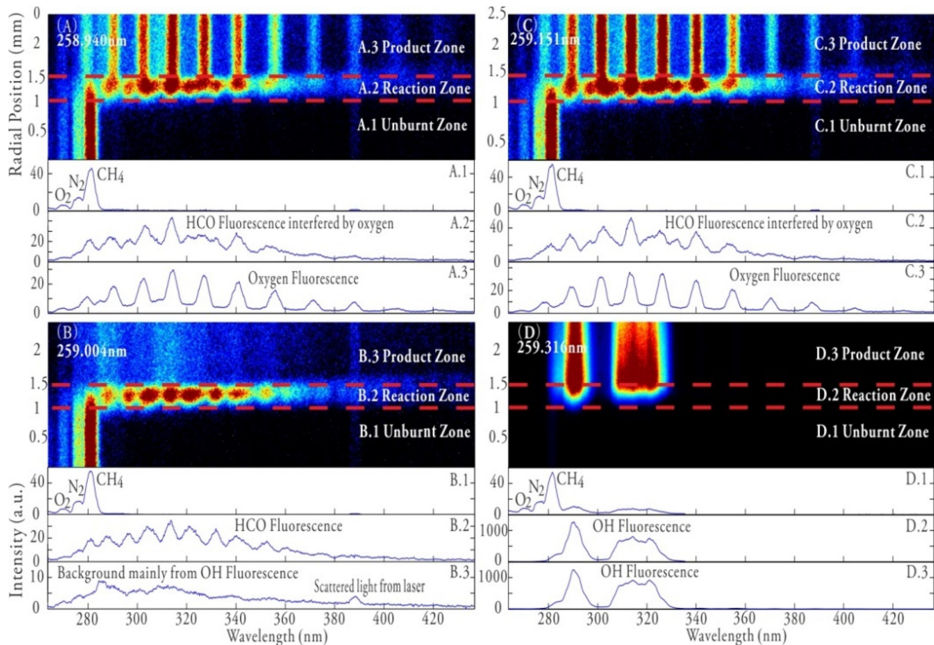


**Figure 4-3** Spatially resolved spectra of laser-induced fluorescence in a methane/air flame with different excitation wavelengths, (A) 258.940 nm, (B) 259.004 nm, (C) 259.151 nm and (D) 259.316 nm. The unburnt zone, the reaction zone and the production zone are delimited by dashed lines, and the spectra extracted from these regions for each excitation wavelength are presented subsequently in the subplots.

Figure 4-4 provides three examples of HCO PLIF in a methane/air laminar flame without interference (Figure 4-4 (1)) and with interference from O<sub>2</sub> (Figure

4-4 (2)) and OH (Figure 4-4 (3)). As can be seen in Figure 4-4 (3), OH interference can completely and thus obliterate the HCO signals if the excitation wavelength is not carefully selected. A careful inspection of Figure 4-4 (1) appears to reveal a dual-layer structure of the thin HCO layer, which can be hardly expected for a laminar premixed flame. This has been shown to be attributable to the additional HCO production by CH<sub>2</sub>O photolysis through CH<sub>2</sub>O + *hv* → HCO + H [59] since CH<sub>2</sub>O has shown broad absorption bands in the UV region [60]. The photolytically generated HCO signal shows a virtually quadratic power-dependence. It has been shown that the CH<sub>2</sub>O interference can be kept at a level below 5% of the natural HCO signal when laser fluence is kept below 2.5 J/cm<sup>2</sup>.

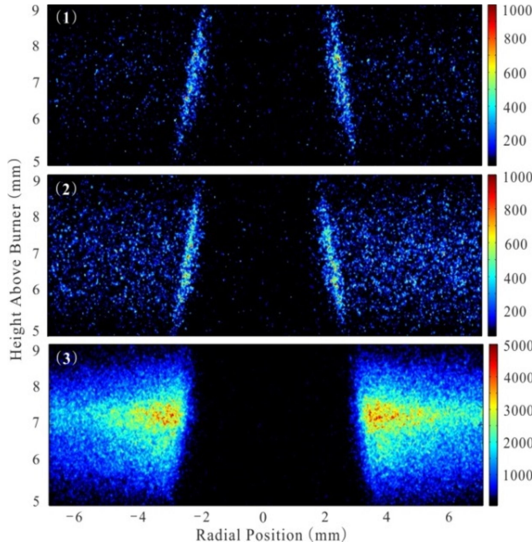


**Figure 4-4** An illustration of the potential interference in a single-shot HCO PLIF measurement: (1) the interference-free HCO LIF excited at 259.004 nm, (2) HCO LIF having O<sub>2</sub> interference when excited at 258.94 nm, and (3) OH interference dominant over HCO signals.

In addition to the interference sources of the HCO signal as discussed above, it is also found that a spectrally continuous background was contributed to the HCO LIF signal under fuel-rich flame conditions, which leads to a considerably higher LIF signal level and a broader “HCO” layer in rich flames. In contrast, a numerical simulation using the GRI 3.0 mechanism [52] predicts a decreasing trend of HCO concentration as flame condition are changed from being stoichiometric to being fuel-rich. This discrepancy is likely attributable to the generation of large hydrocarbons (such as polycyclic aromatic hydrocarbons, PAH) which generally have broad absorption and emission characteristic in the UV region.

In short, the potential interference sources for HCO PLIF measurements from O<sub>2</sub>, OH, the photolysis of CH<sub>2</sub>O and large hydrocarbons in rich flames have been identified. Optimized HCO detection using a multi-mode alexandrite laser can be achieved with excitation at 259.004 nm and subsequent detection from 290 nm to 400 nm with a proper band-pass filter. Restrictions apply to (1) the laser fluence below 2.5 J/cm<sup>2</sup> employed to suppress the falsified HCO signal generated by CH<sub>2</sub>O photolysis and (2) to HCO diagnostics in lean premixed flames to avoid spectral interference from large hydrocarbons. Despite the aforementioned restrictions on the HCO PLIF, the exceptional importance of the HCO radical in hydrocarbon flame chemistries makes it a unique tool for investigating of the fundamentals of turbulent lean premixed hydrocarbon flames. Such feasibility together with the single-shot HCO images obtained will be exemplified further in Chapter 5.

#### 4.2.2 Hot Oxygen Molecule (O<sub>2</sub>)

Hot oxygen, i.e. oxygen molecules in excited electronic or vibrational states, is of particular interest in many areas including plasmas physics [61], atmospheric chemistry [62] and combustion technology [63]. Most existing techniques for the detection of molecular oxygen are based on an indirect manner which detects a tracer LIF that can be affected by the presence of oxygen through the quenching effect. The present work based on Paper II demonstrated the detection of vibrationally excited hot O<sub>2</sub> molecules though the (0-7) band of the well-known B-X *Schumann-Runge* system. The absorption spectrum of the (0-7) band was simulated using LIFsim [64] as can be found in Paper II. An excitation wavelength of 256.972 nm was chosen as the best compromise between obtaining good SNR oxygen LIF signals and minimizing the interference from other species. A blend of rotation transitions, P<sub>1</sub>(35), P<sub>2</sub>(35), R<sub>1</sub>(9) and R<sub>2</sub>(9) was excited simultaneously at this wavelength.

As discussed in section 4.2.1, large hydrocarbons, formyl radical (HCO) and hydroxyl radical (OH) have the potential of interfering with the O<sub>2</sub> LIF signals detected in this wavelength region. To examine the potential interference, O<sub>2</sub> LIF emission spectra were recorded in a lean CH<sub>4</sub>/O<sub>2</sub> flame ( $\Phi=0.9$ ) and a rich CH<sub>4</sub>/O<sub>2</sub> flame ( $\Phi=1.47$ ) as shown in Figure 4-5 (a) and (b), respectively. It can be seen that the LIF emission spectrum from the lean flame shows little interference but possesses a distinctive O<sub>2</sub> spectral structure containing transitions from excited electronic state to successive vibrational levels in the ground electronic state as

assigned in Figure 4-5 (a). Since the oxygen molecules are not fully consumed in the lean flame, the hot O<sub>2</sub> widely spreads out in the production zone, where the temperature is still high. In the rich flame, two hot O<sub>2</sub> layers appear up in the spectrum. The inner layer corresponds to the primary reaction zone, in which the oxygen peaks can be seen at the top of a broad underlying fluorescence background originating predominantly from PAH interference. In the primary reaction zone of the rich premixed flame studied, the PAH contribution to the overall signal was about 50 %. Care should be taken under such condition in interpreting the signals obtained. Further downstream, little PAH interference was observed in the outer layer which corresponds to the secondary reaction zone where the unburnt fuel that remained in the rich flame was mixed and reacted with the ambient air.

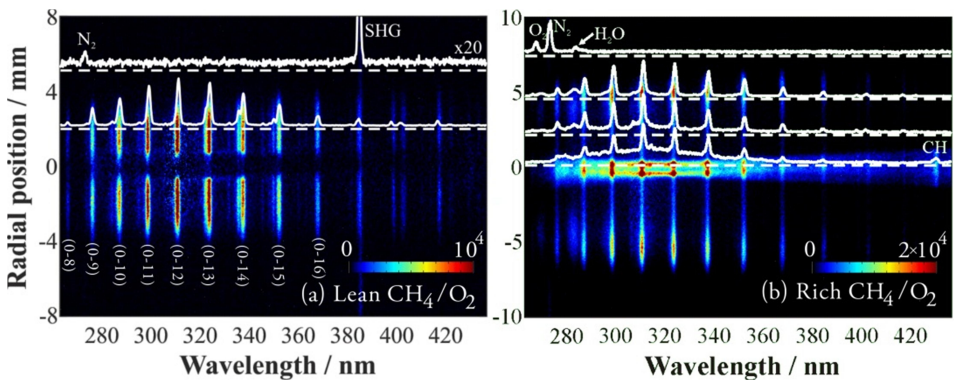


**Figure 4-5** Spectrally resolved emission spectra along a line across the flame front of a laminar (a) Lean  $\text{CH}_4/\text{O}_2$  flame ( $\Phi=0.9$ ) and (b) Rich  $\text{CH}_4/\text{O}_2$  flame ( $\Phi=1.47$ ). Spectra were extracted at selected radial positions indicated by dashed lines.

The instantaneous two-dimensional distributions of hot O<sub>2</sub> are illustrated for the lean flame in Figure 4-6 (a-b) and for the rich flame in Figure 4-6 (c-d). As expected, despite the high oxygen concentration, no LIF signals can be found in the unburnt regions for either flames since virtually no O<sub>2</sub> molecules are populated at the v = 7 vibrational state at room temperature. Also, the lean flame shows a wide distribution of the hot excess O<sub>2</sub> which was found in the product region. In the rich flame, a portion of the O<sub>2</sub> was heated in the thin primary reaction zone before it was consumed. It should be noted that the O<sub>2</sub> LIF signal in this region could be contaminated by PAH interference as Figure 4-5 (b) suggests. Downstream of the primary reaction zone, weak but traceable signals appear corresponding to the presence of a small amount of O<sub>2</sub> (~ 0.9 % in total) in chemical equilibrium in the

product region. Further downstream, the secondary reaction zone was formed and heat was released through oxidizing of the unburnt and other intermediates reactants such as CO and H<sub>2</sub>. It is worth mentioning under thermal equilibrium condition the LIF signals from the O<sub>2</sub> molecules for v =7 are considerable when the temperature is higher than 1500 K. The LIF signal also continues to increase by approximately two orders of magnitude until the temperature approaches 3000 K. This feature makes the hot O<sub>2</sub> LIF signal very sensitive to the flame temperature, preserving the potentials to be utilized for temperature mapping in the future.

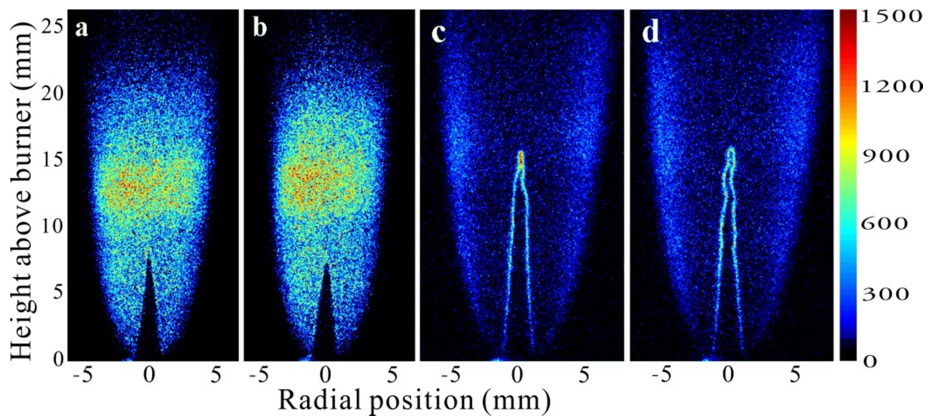


**Figure 4-6** Single-shot PLIF images of hot molecular O<sub>2</sub> recorded in (a-b) a lean premixed flame ( $\Phi=0.9$ ) and (c-d) a rich premixed flame ( $\Phi=1.47$ ).

#### 4.2.3 Cyano (CN) radical

An increasing interest in utilizing renewable biomass-derived fuels as alternatives to fossil fuels has emerged [65], motivating the demand to study the detailed chemical kinetics involved in the combustion of nitrogen-containing fuels. Cyano radical (CN) is one of the key species that participate in the conversion of fuel-nitrogen as well as the formation and re-burning of NO in the prompt NO mechanism [66]. Hints concerning the role of the CN radical in the interplay of CH<sub>4</sub> and NH<sub>3</sub> chemistry can be also found in Figure 4-2. Many of reported CN measurements using various laser techniques [67-70] are obtained mostly point-wise and average-based in low-pressure flames doped with NO<sub>2</sub> or NO. In contrast, instantaneous two-dimensional CN imaging is rarely reported in the literature, despite its clearly being more appropriate for the investigation of turbulent flames. The present work reported in Paper III demonstrated the feasibility of single-shot high-quality CN

PLIF images obtained using an alexandrite laser (linewidth  $2.5 \text{ cm}^{-1}$ , 30 ns pulse duration) with a novel excitation at the B-X (1-0) band close to 359 nm and subsequent off-resonance detection at around 387 nm. The comparison of such excitation scheme with others is referred to in ref. [71]. A conventional dye laser system (linewidth  $0.3 \text{ cm}^{-1}$ , 8 ns pulse duration) was additionally employed for CN excitation as a comparison.

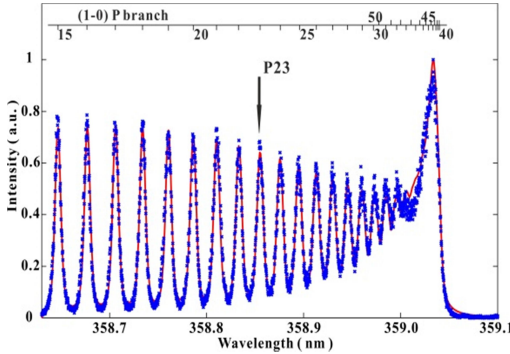


**Figure 4-7** An excitation scan over the P-branch bandhead of the CN B-X (1-0) band acquired with a dye laser (linewidth  $0.3 \text{ cm}^{-1}$ ). The red line represents a LIFBASE simulation (Fitting parameters:  $T=1605 \text{ K}$  with a thermalized system,  $0.005 \text{ nm}$  resolution and a 39% Lorentzian contribution to line broadening).

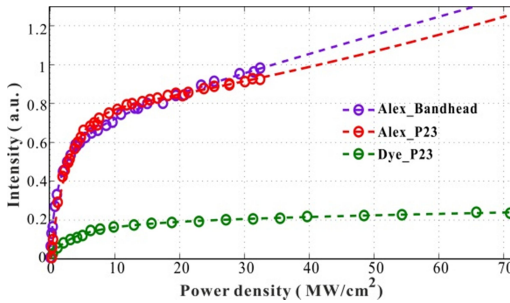


**Figure 4-8** Power dependence for narrowband dye laser excitation of the P(23) transition (green circles) and broadband alexandrite laser excitation of the bandhead (purple circles) and the P(23) transition (red circles) in the CN B-X (1-0) band.

Figure 4-7 shows an excitation scan (blue dots) over the P-branch bandhead of the CN B-X (1-0) band using a dye laser, and the corresponding spectral simulation (red curve) performed in LIFBASE agreed closely with one another. The P(23) line as indicated by the arrow was identified. In Figure 4-8 the power dependence of the CN LIF signals obtained through excitation at both the P(23) line and the bandhead using both lasers is compared. It can be clearly seen in Figure 4-8 that the CN LIF signals (green dots) excited by the dye laser at the P(23) line exhibit a strong saturation effect with laser irradiance higher than  $5 \text{ MW/cm}^2$ . In contrast, the CN excitations using the alexandrite laser at both the bandhead and the P(23) line deliver a significantly higher signal level by a factor of  $\sim 3$  to  $5$  than that of the dye laser with the same laser irradiance, and no complete

saturation was observed with the maximum irradiance  $\sim 33 \text{ MW/cm}^2$ . The weaker LIF signal achieved by the dye laser excitation can be explained by the fact that the laser-coupled rotational ground state can be depleted without being sufficiently repopulated within the short laser pulse duration ( $\sim 8 \text{ ns}$ ) due to the limited rotational energy transfer (RET) rate. The relatively long-pulse excitation produced by the alexandrite laser resulted in an increased repopulation through rotational energy transfer (RET) during the laser pulse. In addition, multi-line excitation using the broad-band alexandrite laser ( $\sim 2.5 \text{ cm}^{-1}$ ) becomes advantageous at high laser irradiances since the multi-line excitation further suppresses the saturation effect. For example, excitation of the P(23) line using the alexandrite laser also involved excitation of the P(22) and P(24) lines as well as weak excitation of the P(21) and P(25) lines, which resulted in a three times higher overlap integral between excited transitions and the laser spectral profile than that of the dye laser excitation. Therefore, at complete saturation of alexandrite laser excitation, an additional corresponding increase in the LIF signal would be expected. Similar advantages gained from the long-pulse and broadband features of the alexandrite laser have also been demonstrated previously for CH PLIF measurements [48]. The CN LIF emission spectra recorded in a  $\text{NH}_3$ -doped (4230 ppm)  $\text{CH}_4$ /air laminar flame using both lasers further support the conclusions drawn above. For details regarding this, one is referred to Paper III.

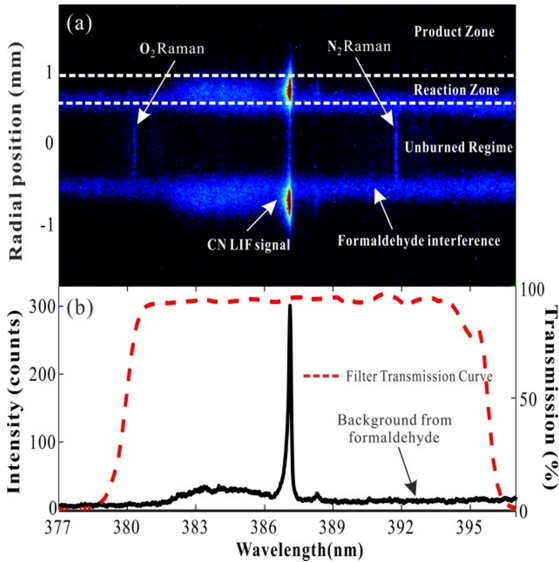


**Figure 4-9** (a) A spatially resolved LIF spectrum acquired using the alexandrite laser for bandhead excitation in a pure  $\text{CH}_4$ /air flame together with (b) a spectrum extracted from the reaction zone. The transmission curve of the interference filter employed (red dashed line) is displayed in (b).

To exclude any potential interference, an additional LIF emission spectrum (cf. Figure 4-9) was recorded in a pure methane/air flame in which the CN concentration was significantly lower than in the NH<sub>3</sub> doped flames. As shown in Figure 4-2, the formation of CN is promoted by NH<sub>3</sub> doping through the additional generation of N radicals which react with the CH<sub>3</sub> radical so as to generate CN via HCN. In an unseeded flame, N radicals are generated by the prompt-NO mechanism through CH which has a significantly reduced concentration resulting in less CN production. Figure 4-9 shows a 24 times weaker CN signal in an unseeded CH<sub>4</sub>/air flame than that in an NH<sub>3</sub>-seeded (4230 ppm) flame. Despite the Raman signals from N<sub>2</sub> and O<sub>2</sub> and the “leaked” CN signal in the unburned regime due to the limited spatial resolution (~ 0.5 mm) of the spectrometer system employed, a continuous background also appears at a spatial location slightly shifted towards the unburnt regime with regard to the CN signal, attributing to the CH<sub>2</sub>O interference. Given the transmission curve (the red dashed line) of the narrow band-pass filter employed, the contribution of CH<sub>2</sub>O interference to the CN signals was about 56 %. With the employment of an optimal band-pass filter which cuts off the transmission above 389 nm, the interference level could be reduced to 30 %. For this reason and the less detectable CN signal, the application of CN PLIF in unseeded methane/air flame is limited. Yet it is nevertheless valuable for investigating, flames burning nitrogen-containing fuels for example.

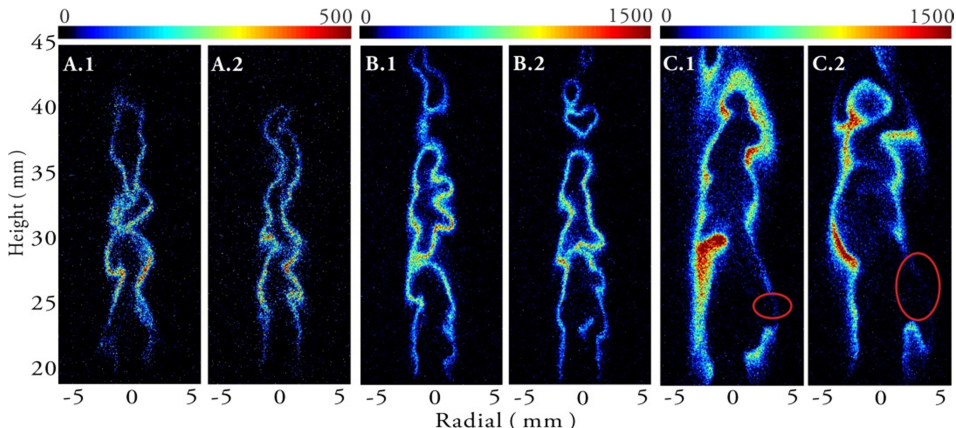


**Figure 4-10** Comparison of PLIF images acquired in turbulent flames (30 m/s jet speed) doped with 2800 ppm NH<sub>3</sub> using (A) dye laser excitation and (B) alexandrite laser excitation with  $\Phi=1.0$  and (C)  $\Phi=1.4$ .

Single-shot CN PLIF measurements were demonstrated using both lasers in turbulent CH<sub>4</sub>/air flames ( $\Phi=1.0$ ) at 30 m/s jet speed and doped with 2800 ppm of NH<sub>3</sub> as shown in Figure 4-10 (A) and (B). A highly wrinkled CN layer with a measured thickness of ~ 440  $\mu\text{m}$  which is twice as thicker than the CH layer thickness under similar flame conditions is clearly resolved [48]. The CN PLIF achieved by use of alexandrite laser excitation results in an improved SNR (~ 40) as compared with that obtained with use of the dye laser (~17). In addition, Figure 4-10 (C) shows CN PLIF images acquired in a  $\Phi=1.4$  turbulent flame with the same jet speed and the same amount of NH<sub>3</sub> seeding. The CN layer becomes appreciably thicker and disconnected at certain locations marked by the red circles, which implies a complex interplay between turbulence and the nitrogen-chemistry in NH<sub>3</sub>-dopes flames, a matter requires further investigations. Based on the estimated CN concentration (to be discussed in section 4.3) and the achieved SNRs in the studied flames, the present CN detection strategy renders a CN detection limit of a few hundred ppb for a 20-mm imaging size with a SNR of 5.

#### 4.2.4 Gaseous Ammonia (NH<sub>3</sub>)

The detection of NH<sub>3</sub>, a key species in the chemistry of fuel-bound nitrogen and a primary product of biomass pyrolysis [72], in combustion-relevant applications has been promoted due to in particular the extended use of biomass energy for power production [73]. The present work reported in Paper IV has demonstrated the detection of ammonia using two-photon LIF, and the characteristics of LIF signal have been quantified under conditions of elevated temperature and pressure which emulate the combustion environments in industrial applications.

As outlined in Figure 4-11, the X-C' electronic transitions of NH<sub>3</sub> in vacuum ultraviolet (VUV) were probed through absorbing two photons simultaneously at ~ 305 nm, and the fluorescence from the C'-A transitions was detected at around 565 nm. Figure 4-12(a) shows an excitation scan spectrum (solid line) close to ~ 305 nm at 387 K and atmospheric

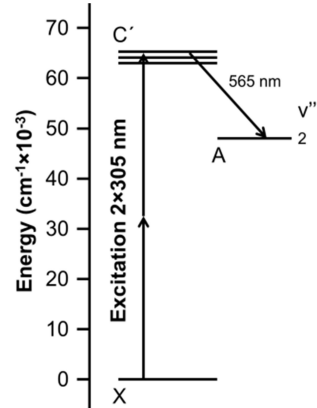


**Figure 4-11** Schematic energy-level diagram indicating the probed C'-X and detected C'-A transitions of NH<sub>3</sub>.

pressure together with PGOPHER simulation [74] (the dashed line). Qualitative agreement between the experiment and simulation can be observed, permitting reliable identification of the transitions corresponding to the spectral lines. Two peaks located at 304.8 nm (line 1) and 304.9 nm (line 2), from the qQ-branch were identified. The corresponding emission spectrum excited at 304.8 nm is displayed in Figure 4-12(b). To investigate the temperature dependence of the NH<sub>3</sub> LIF signal, an excitation scan at an elevated temperature of ~ 780 K was also performed as shown in Figure 4-12 (c). The PGOPHER simulation likewise shows close agreement with the experimental measurements, confirming the accuracy of PGOPHER simulation which can be used to predict the temperature dependence of the NH<sub>3</sub> LIF signal in a wider temperature range. Figure 4-12(d) shows the PGOPHER prediction of the NH<sub>3</sub> LIF temperature sensitivity calculated as the percentage of change in the LIF-signal with excitations at line 1 and line 2. It appears that line 2, although of lower signal strength, is more temperature insensitive over the temperature interval of 400–600 K. This temperature range is relevant to the one employed for catalytic NO<sub>x</sub> reduction by use of ammonia [75]. The consumption of NH<sub>3</sub> in flames typically starts at temperatures below 800 K. Thus, excitation at 305.9 nm seems to be preferable in order for temperature insensitive and correct qualitative and quantitative NH<sub>3</sub> LIF measurements to be obtained.

Since the NH<sub>3</sub> LIF signal is achieved through a two-photon process, stimulated emission (SE) can occur as a loss mechanism to the detected LIF signal. This was examined at atmospheric pressure with varying laser irradiance, and the pressure dependence of the LIF and SE signals was also investigated. Details of the results are referred to in Paper IV. The results indicated that the LIF signal shows an  $I^2$  dependence of laser irradiance, whereas the SE signal follows a highly nonlinear  $I^5$  power dependence which was only detectable at a high laser irradiance of ~10 GW/cm<sup>2</sup>. It can thus be concluded that SE does not compose a loss mechanism for two-photon NH<sub>3</sub> LIF imaging measurements which are typically performed at lower irradiance levels, but attention needs to be taken for performing point-wise measurements with a focused beam. Concerning the pressure dependence of the signals, a decrease in signal strength with an increase in pressure was found for both the LIF and the SE signals after normalization versus pressure. Although the C' state is known to be pre-dissociative, the pressure dependence of both the LIF and the SE signals indicates other dominating loss mechanism such as collisional quenching rather than dissociation which has a rather weak pressure dependence [76].

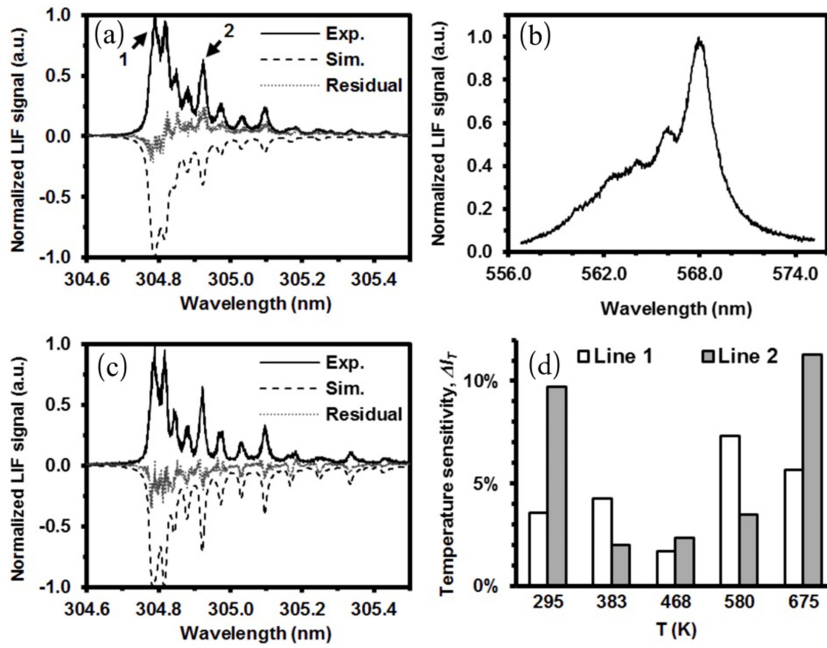


**Figure 4-12** Excitation scan spectra of  $\text{NH}_3$  C-X transition at (a) 383 K (c) 780 K. (b) and an emission spectrum for excitation at 304.8 nm (d) the  $\text{NH}_3$  LIF temperature sensitivity for lines 1 and 2 calculated as the percentage of change in LIF-signal is indicated in (a).

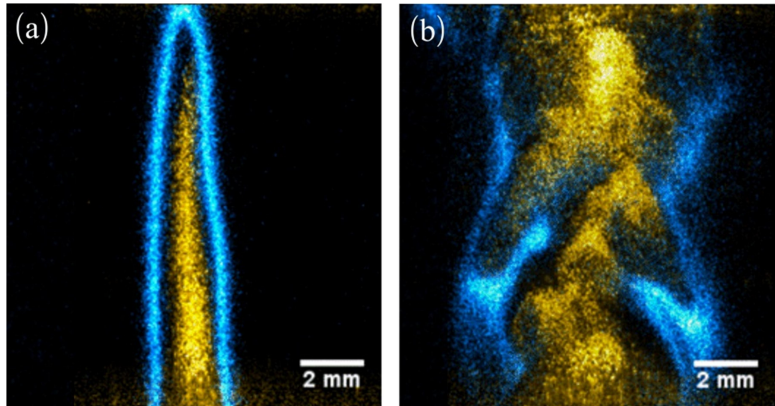


**Figure 4-13** Simultaneous  $\text{NH}_3$  (yellow) and  $\text{CH}$  (blue) images acquired in stoichiometric (a) laminar ( $Re=1400$ ) and (b) turbulent ( $Re=11000$ )  $\text{NH}_3$ -methane-air flames with 0.2 % of  $\text{NH}_3$  as a fuel in the total flow.

To illustrate the ability for ammonia visualization under combustion conditions, simultaneous NH<sub>3</sub> and CH images were recorded for both stoichiometric laminar and turbulent NH<sub>3</sub>-methane-air flames as shown in Figure 4-13. Good SNR of NH<sub>3</sub> imaging  $\sim 8$  was achieved along with a CH image which assists visualizing the flame front structures. The laminar flame shows a distinct gap between the central NH<sub>3</sub>-zone (yellow) in the fuel-air mixture and the thin CH-zone (blue) of the flame reaction zone, indicating NH<sub>3</sub> decomposition to occur in the flame preheat zone. In the turbulent flame, a complex highly wrinkled flame front can be observed along with non-uniform spacing between the CH- and NH<sub>3</sub>-zones, suggesting turbulence having a strong effect on NH<sub>3</sub> consumption, a matter deserves further investigation. Since the mixing of ammonia with flue gases has been identified as a key parameter for effective NO<sub>x</sub> reduction [77], the present NH<sub>3</sub> imaging technique can be a valuable tool for obtaining a better understanding and optimization of the ammonia deNO<sub>x</sub> process.

#### 4.2.5 Nitrogen Monohydrate (NH) Radical

Nitrogen monohydrate (NH) locates at the downstream of the NH<sub>3</sub> chemistry, corresponding to the reaction zone layer of NH<sub>3</sub> flames. NH also plays an important role in the oxidation routes of other nitrogen-containing fuels [66], which makes accurate measurements of this species highly valuable. Most of the NH measurements that have been reported in flames were based on point-wise detection for which either absorption or fluorescence techniques were employed. A summary of these techniques can be found in the introduction of ref. [78]. The capability of NH imaging has rarely been demonstrated in the literature. The present work (reported in Paper IX) which involved a detailed investigation of the NH spectroscopy suggested excitation-detection schemes for NH PLIF imaging with the possibility of quantification.

In the UV spectral range, NH has an accessible electronic transition, i.e. the A<sup>3</sup>Π-X<sup>3</sup>Σ<sup>-</sup> system. The (0-0) vibrational band of the A-X system can be approached at around 333 nm, while the (1-0) vibrational band is located at around 306 nm. These two wavelength ranges can be approached using a dye-laser system with dyes Rhodamine 610/640 and LDS 698 after frequency doubling. The corresponding fluorescence spectral range that was detected for both excitation wavelengths from either (0-0) or (1-1) resides around 333 nm. The excitation scan spectra of these two bands obtained in a premixed laminar NH<sub>3</sub>/air flame ( $\Phi=1.4$ ) are shown in Figure 4-14 (a) and (b), respectively. The corresponding PGOPHER

simulations oriented downwards in Figure 4-14 (a) and (b) were performed in order to assign the spectral lines using molecular data from Dixon [79] and Brazier [80]. Fine adjustments of the molecular constants and of the band origin are required to achieve close agreement with the experimental data obtained. Temperature-insensitive lines, i.e. R<sub>1</sub>(5) and R<sub>1</sub>(4) for the (0-0) and the (1-0) bands, respectively, have been identified as indicated by the arrows in Figure 4-14 (a) and (b).

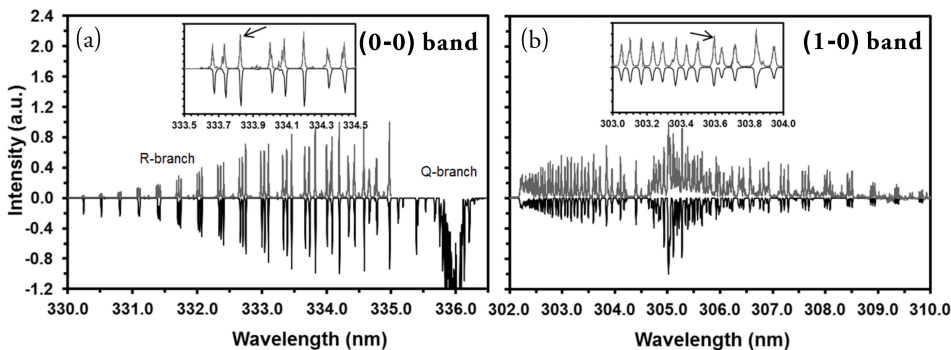


**Figure 4-14** Excitation scan spectra of NH vibrational bands (oriented upwards) together with corresponding simulated spectra (oriented downwards), (a) the (0-0) band and (b) the (1-0) band. Inserts show the magnified view of the spectra in the vicinity of the probed rotational transitions of (a) R<sub>1</sub>(5) and (b) R<sub>1</sub>(4).

The power dependences of both transitions in the corresponding bands are shown in Figure 4-15. The transition in the (0-0) band shows a gradual increase at irradiances below  $10^{-2}$  GW/cm<sup>2</sup> and the line fitted to the data points in the log-log diagram has a slope of 0.76, indicating a sub-linear dependence of the signal on laser irradiance and that the fluorescence is partially saturated. At irradiances above  $10^{-2}$  GW/cm<sup>2</sup> the signal gradually goes towards an essentially constant level, confirming close to complete saturation. For excitation of the (1-0) band, data acquired at irradiances up to  $10^{-2}$  GW/cm<sup>2</sup> can be fitted to a line of slope 0.98, indicating distinctly linear signal dependence. At high irradiance levels, the fluorescence signal shows still a sub-linear increase with laser irradiance, signifying a partially saturation. Quantification of the LIF signals by evaluating the power dependence curves will be discussed in section 4.3. Despite the similar maximum intensity achieved at the highest irradiance, it is worthy of noting that the off-resonance fluorescence detection obtained via the excitation at the (1-0) band is more beneficial under conditions of challenging background and interference issues which is frequently encountered in biomass applications.

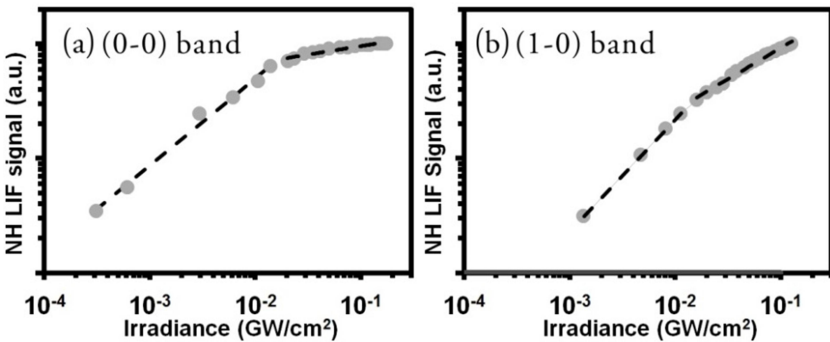


**Figure 4-15** The NH LIF signal versus laser irradiance: (a) Excitation of  $R_1(5)$  in the (0-0) band; (b) Excitation of  $R_1(4)$  in the (1-0) band.

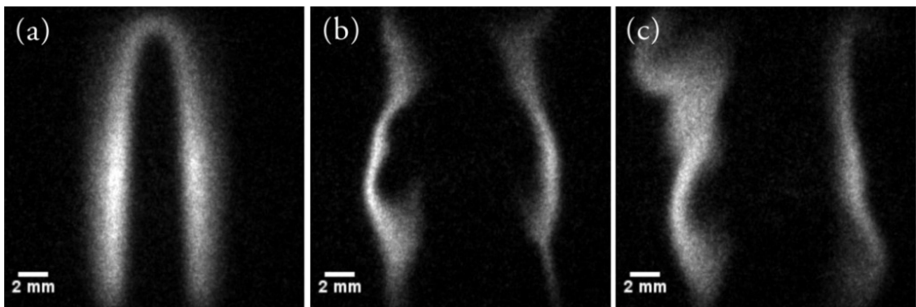


**Figure 4-16** Single-shot NH PLIF images acquired in premixed  $\Phi=1.4$  (a) laminar and (b-c) turbulent  $\text{NH}_3/\text{air}$  flames.

Utilizing the excitation at the (1-0) band, instantaneous NH PLIF images, as shown in Figure 4-16, were acquired in premixed fuel-rich  $\text{NH}_3/\text{air}$  flames of  $\Phi=1.4$ , under laminar ( $\text{NH}_3$  0.33 L/min and air 0.85 L/min) and turbulent ( $\text{Re}=11400$ , jet speed of 16 m/s) conditions. The NH layer, which can be regarded as the reaction zone layer of  $\text{NH}_3$  flames has a thickness of around 2 mm in the laminar flame as shown in Figure 4-16 (a). This thickness is greater than the reaction zone thickness measured in hydrocarbon flames [49, 71], as can be expected from the laminar flame speed of  $\text{NH}_3/\text{air}$  mixtures, of around 10 cm/s which is typically 3-4 times lower than that of hydrocarbon flames. Interestingly, images acquired in the turbulent flame, shown in Figure 4-16 (b-c), exhibit both significant thinning and broadening of the NH layer in comparison with the laminar one, something is rarely seen in the corresponding hydrocarbon flames. This indicates  $\text{NH}_3/\text{air}$  flames having a stronger interplay between turbulence and flame chemistry, which can also be reflected on the  $K_a$ . Since  $K_a$  is inversely

proportional to the laminar flame speed to a power of 1.5, turbulent  $\text{NH}_3$ /air flames compose significantly higher  $Ka$  values than in the corresponding  $\text{CH}_4$ /air flames, given the same degree of turbulent intensity of flow in both cases. In addition, as indicated in Figure 4-2, the  $\text{NH}_3$  chemistry involves fewer species and may be simpler than the  $\text{CH}_4$  chemistry, for example. Therefore,  $\text{NH}_3$ /air flames might be good candidates for investigating turbulence/flame interaction at high  $Ka$  conditions, since this enables experiments to be conducted under conditions of simpler configuration, such as lower flow speed, which may be also more advantageous for the numerical simulations. Together with the development of detection strategies for other species as presented in previous sections, employing the high-quality NH imaging demonstrated in the present work provides a unique tool for studying the fundamentals of the turbulence/flame interaction.

#### 4.2.6 Two-line Atomic LIF (TLIF) of Indium

In addition to the compositional fields in turbulent flames, temperature field is one of the most important parameters in combustion conditions as chemical reaction rates are often controlled by temperature. Two-line atomic LIF (TLIF) of the indium atom has been demonstrated to be a valuable technique to provide information of instantaneous temperature field [81]. The principle of the TLIF is outlined in Figure 4-17. The Stokes transition follows the excitation from the 0 state to the 2 state with 410 ( $\lambda_{02}$ ) nm radiation, and the subsequent fluorescence at 450 nm is detected, while the Anti-Stokes transition is excited by 450 ( $\lambda_{12}$ ) nm from the 1 to the 2 state and the fluorescence at 410 nm is detected. Given the laser spectral irradiance ( $I_{02}$  and  $I_{12}$ ) at two excitation wavelengths, the temperature can be related to the ratio of the detected fluorescence ( $F_{02}$  and  $F_{21}$ ) by:

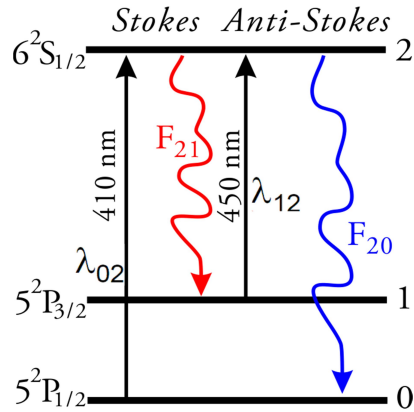


**Figure 4-17** Schematic of probed and detected transitions of TLIF of Indium.

$$T = \frac{(E_1 - E_0)/k}{\ln \frac{F_{21}}{F_{20}} + \ln \frac{I_{12}}{I_{02}} + 4 \ln \frac{\lambda_{21}}{\lambda_{20}} + \ln C} \quad (4.1),$$

where  $E$  is the energy of corresponding states,  $k$  the Boltzmann constants and  $C$  is a constant determined from experiment. The feasibility to achieve two-dimensional temperature mapping using this method relies partially on having a robust seeding system which can constantly deliver indium components into the combustion system without causing any perturbation to the flame. The conventional way of seeding is done by sending small droplets of indium chloride ( $\text{InCl}_3$ ) solution which dry to  $\text{InCl}_3$  crystals and then thermally decompose to form atomic indium when passing through the flame front. Therefore, indium signal can only be obtained from the post production zone of the flame [82]. Furthermore, despite the problems of clogging and condensation on instrument surfaces which might be caused by this seeding system, the solvent-based seeding system shows effects on the flames by changing the flame chemistry and temperature [83-85]. The present work demonstrates the utilization of a novel seeding system which takes the organometallic compound tri-methyl-indium (TMI) as an indium carrier and seeds into reacting flows. The TMI compound is featured by a comparatively high vapor pressure ( $p$ , in torr) as a function of temperature ( $T$ , in Kelvin) which can be expressed as [86]:

$$\log(p) = 10.98 - (3204/T) \quad (4.2).$$

Therefore, the seeded indium compounds are in gaseous phase. The seeding concentration can either be adjusted by the amount of inert carrier gas (typically  $\text{N}_2$  or Ar) that flows through the TMI bubbler or by the equilibrium temperature of the TMI bubbler that is seated in a temperature-controlled water bath. Figure 4-18 shows a photograph of a laminar premixed methane/air flame ( $\Phi=0.8$ ) seeded with 10 ppm TMI. A 10 mW diode laser was tuned to 410 nm for the excitation of indium. The strong indium LIF signal can be seen by naked eyes, indicating high efficiency of the present seeding

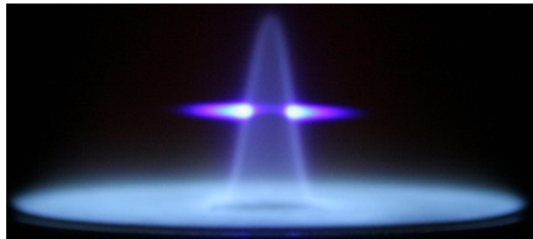


**Figure 4-18** Photograph of a laminar premixed methane/air flame ( $\Phi=0.8$ ) seeded with 10 ppm TMI. LIF of indium was excited by a 10 mW diode laser at 410 nm.

method which effectively converts the gaseous TMI into indium atoms. Considering the strong indium signal and its uniform distribution in the flame, an improved performance of the TLIF method for temperature mapping can be expected.

In addition to seeding TMI into a reacting jet flow, the jet flow was also operated with 234 ppm TMI carried by the inert gas with the flow rates similar to the one used for the piloted laminar flame. When the coflow is run under fuel-rich condition ( $\Phi=1.4$ ), an orange luminescence of the central jet appears. The emission photograph of such a condition is shown in Figure 4-19 (a) and the corresponding spectrum in Figure 4-19 (b). The emission of OH from the coflow along with atomic indium emission at 410 and 450 nm were observed. In addition, a congested cluster of bands appeared close to 360 nm, which is believed to originate from transitions of the InOH molecules [87]. Two narrow and isolated bands were also observed at around 600 nm. The high resolution spectra of these two bands are shown in Figure 4-20 (a) and (b). The PGOPHER simulations (the red curve in the figure) revealed the orange luminescence to arise from InH transitions. The InH emission spectrum was observed from a King furnace as reported firstly by Grundstrom [88], followed by extensive studies of the InH spectrum [89, 90]. To the best of the author's knowledge, the present work reports the first observation of InH emission spectrum in a combustion environment. This observation is relevant to combustion synthesis which is currently the most widely used means of nano-materials production [91].

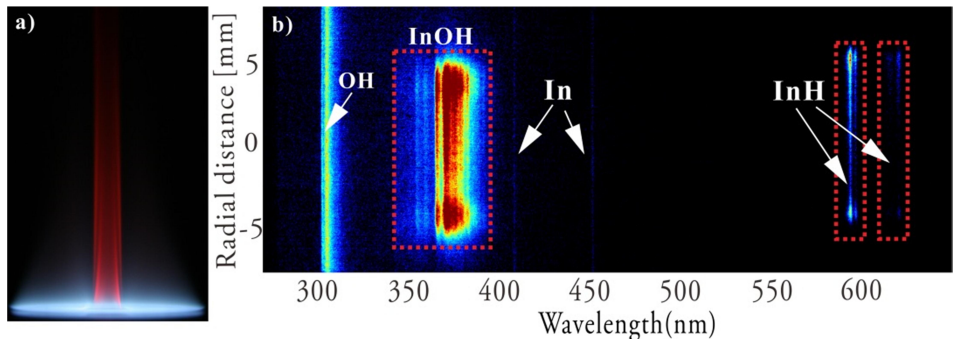


**Figure 4-19** (a) Emission from an inert central jet (Ar as carrier) with 234 ppm TMI seeding, the surrounding McKenna flame being operated at  $\Phi=1.4$ . (b) Low-resolution spectrum of the orange luminescence.

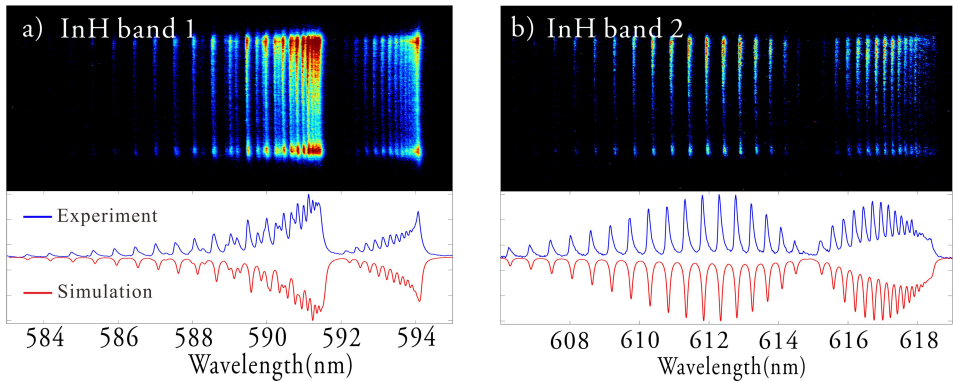


**Figure 4-20** High-resolution spectra of InH bands centered at (a) 590 nm and (b) 614 nm.

## 4.3 Concentration Quantification from a LIF signal

### 4.3.1 General discussion

In general, given constant incident laser irradiance, LIF signal is proportional to the concentration of the species probed. However, the detected LIF signal may not always be linearly dependent on the incident laser irradiance. Figure 4-21 shows a typical laser irradiance dependency of detected LIF signal. Three regimes, i.e. the linear regime, the partially-saturated regime and the saturated regime can be identified. In the linear regime, the LIF signal increases linearly with the laser irradiance. A further increase of the laser irradiance leads to a non-linear response of the LIF signal, and thus the partially-saturated regime is entered. At the highest laser irradiances, the LIF signal barely increases with increasing laser irradiance since the saturated regime is entered. Examples of such power dependence of the LIF signal can be seen in Figure 4-8 and Figure 4-15 in the previous sections. Assuming a simplified two-level energy diagram (labeled 1 and 2), different expressions for the detected LIF signal can be derived from the rate equation depending on the regime where laser irradiance resides. Quantification of the LIF signal usually requires a calibration process.

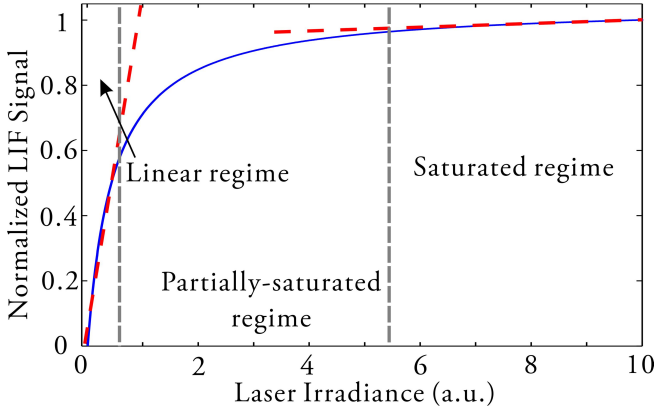


**Figure 4-21** Schematic plot of the laser irradiance dependence of the LIF signal.

### Linear regime:

In the linear regime, the detected LIF signal ( $S_{\text{linear}}$ ) can be related to the species concentration ( $N_t$ ) as expressed:

$$S_{\text{linear}} = \frac{h\nu D N_t f}{4\pi} \frac{A_{21}}{A_{21} + Q_{21}} I_{lv} \quad (4.3),$$

where  $h$  is the Planck's constant,  $\nu$  the transition frequency,  $I_{lv}$  the laser irradiance,  $D$  the coefficient of the detection system,  $N_t$  the total number density,  $Q$  the quenching rate,  $A_{21}$  the Einstein coefficient for spontaneous emission,  $f$  the Boltzmann factor which denotes the fraction of total population excited by the laser. To quantify the LIF signal, a calibration source with known parameters (e.g. species concentration and temperature) is commonly needed. The concentration can thus be estimated as:

$$N_t = N_{\text{ref}} \left[ \frac{S_{\text{linear}}}{S_{\text{ref}}} \cdot \frac{f_{\text{ref}}(T)}{f(T)} \cdot \frac{I_{lv,\text{ref}}}{I_{lv}} \cdot \frac{Q(T)}{Q_{\text{ref}}(T)} \right] \quad (4.4),$$

where the subscript “ref” denotes the quantities measured at a reference condition. The reference condition can be characterized either from other experimental measurements or from numerical simulations where the temperature and the compositional fields are known. The major uncertainty concerns the estimate of quenching rate, which is species-specific and depends not only on the local temperature but also on the quenching partners. Assuming a uniform flow field, expressions for  $Q$  can be derived for certain species. For example, the temperature-dependent  $Q$  for the OH radical can be calculated using the expression given by

Paul [92] and its quenching cross-section data from ref. [93]. In addition to the quenching rate, the Boltzmann factor  $f$  may be difficult to estimate for some species. For diatomic molecules such as OH,  $f$  can be estimated using the software LIFBASE. The temperature-insensitive transition  $Q_1(8)$  was typically selected for OH excitation in the present work. To estimate  $f$  for more complex molecule such as CH<sub>2</sub>O from spectroscopic simulations using PGOPHER will be discussed in Section 4.3.2.

### Partially-saturated regime

In the partially-saturated regime, the partially-saturated LIF signal,  $S_{PF}$  can be expressed as [94]:

$$S_{PF} = \frac{f \cdot N_t h v A_{21} D}{4\pi(f + g_1/g_2)} \left[ 1 - \frac{(Q_{21} + A_{21}) \cdot c}{(f + g_1/g_2) B_{12} I_v} \right] \quad (4.5),$$

Where  $c$  is the speed of light,  $g_1$  and  $g_2$  the statistical weights of the laser-coupled levels, and  $B_{12}$  the Einstein coefficients for absorption. It can be seen that if  $S_{PF}$  is plotted against  $(I_v)^{-1}$ , a linear line can be drawn where the offset (i.e. the term outside the bracket) is proportional to  $N_t$ . Since other quantities in this term are either known or can be canceled out through calibration,  $N_t$  can be estimated accordingly.

### Saturated regime

In the saturated regime, the saturated LIF signal ( $S_{FF}$ ) can be expressed as:

$$S_{FF} = \frac{f N_t h v A_{21} D}{4\pi(f + g_1/g_2)} \quad (4.6),$$

which is no longer dependent on the laser irradiance and the dependence on the quenching rate is also eliminated.  $S_{FF}$  is a constant that can be estimated from the curve of laser irradiance dependence (cf. Figure 4-21). Similarly, with some of the quantities known,  $N_t$  could be estimated through calibration. Note that the wing effects from both the temporal and line shape profiles of laser pulse deviates the detected LIF from complete saturation even at high laser irradiance. This could introduce uncertainties in the quantification of the LIF signal.

### 4.3.2 CH<sub>2</sub>O Quantification

CH<sub>2</sub>O is one of the most important species in the fuel chemistry of hydrocarbons, indicating the initiation of chemical reactions. Quantification of the CH<sub>2</sub>O LIF signal can thus be useful for model validation. The linearity of the CH<sub>2</sub>O LIF signal excited at 355 nm even with high incident laser irradiance has been shown by Brackmann et al. [95]. Thus, Equation (4.5) is applicable to CH<sub>2</sub>O quantification. Calibration can be carried out in a known laminar flame, for which the concentration of CH<sub>2</sub>O might be estimated from CHEMKIN simulation under similar flame configuration conditions. The major difficulties in quantifying the CH<sub>2</sub>O LIF signal arises from the uncertainty concerning the quenching rate ( $Q$ ) and the Boltzmann factor ( $f$ ).

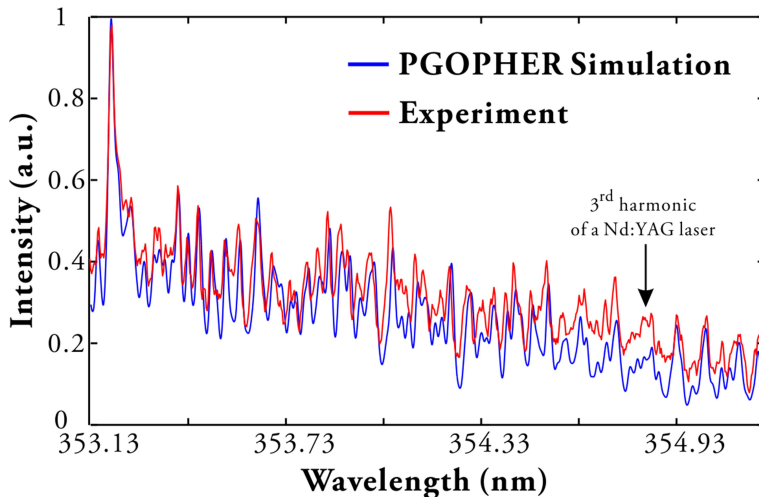


**Figure 4-22** The CH<sub>2</sub>O absorption spectrum as measured at 423 K, 1 atm (red curve) compared with PGOPHER simulation (blue curve).

Literature on models and experimental data concerning the quenching rate of CH<sub>2</sub>O LIF signal are limited. The limited experimental data available includes the one reported by Metz et al. [96] which showed that the CH<sub>2</sub>O fluorescence lifetime is inversely linearly proportional to the temperature up to 800K, suggesting a relation of  $Q \propto T$ . This relationship is qualitatively consistent with several experimental observations in flames [97-99]. Thus, to quantify the CH<sub>2</sub>O signal, the relation of  $Q \propto T$  is adopted to  $T < 800\text{K}$  and a constant quenching rate  $Q = Q(T=800\text{ K})$  is assumed for  $T > 800\text{ K}$  due to the lack of experimental data.

In order to estimate the Boltzmann factor ( $f$ ), PGOPHER simulation was performed to fit the CH<sub>2</sub>O absorption spectra as measured at elevated temperatures by Metz et al. [96] as shown exemplarily in Figure 4-22. Close agreement has been found between simulation and experiment. The effective Boltzmann factor for CH<sub>2</sub>O representing the sum of the Boltzmann factors over the laser-probed transitions can be estimated using PGOPGER. In the present work, CH<sub>2</sub>O was excited at 354.85 nm (i.e. 355 nm radiation from a 3<sup>rd</sup> harmonic of the Nd:YAG laser) with a line width of  $\sim 1 \text{ cm}^{-1}$ . The estimated corresponding temperature dependence of the Boltzmann factor for CH<sub>2</sub>O is shown in Figure 4-23. The Boltzmann factors of CH<sub>2</sub>O excited at other wavelengths can also be estimated by the present PGOPHER simulation, which reduces the uncertainty introduced by the Boltzmann factor when quantifying the CH<sub>2</sub>O LIF signal.

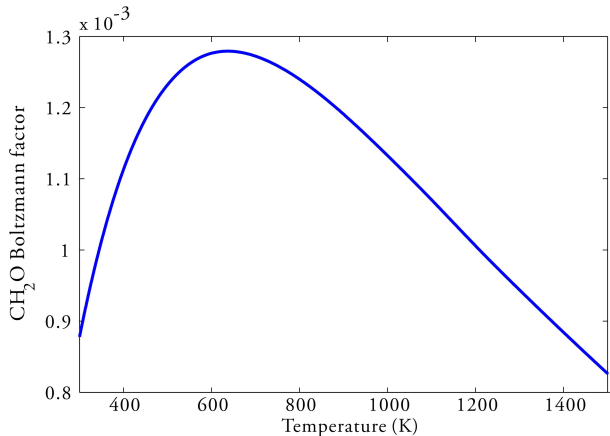


**Figure 4-23** The temperature dependence of the Boltzmann factor of CH<sub>2</sub>O excited by laser radiation at 355 nm with 1 cm<sup>-1</sup> linewidth being evaluated using PGOPHER.

## 4.4 Laser Rayleigh Scattering Thermometry

Laser Rayleigh scattering is commonly employed for temperature mapping in combustion environments. The principle is based on the idea gas law which states that the temperature is inversely proportional to the gas number density. The Rayleigh signals ( $I_f$ ) from measurements are calibrated by the Rayleigh signal ( $I_{ref}$ ) measured under known conditions, for example, pure nitrogen gas at 298 K. If the effective Rayleigh scattering cross sections ( $\sigma$ ) of the gas mixture are known, the temperature can be calculated by:

$$T_f = T_{ref} \frac{I_{ref}}{I_f} \frac{\sigma_f}{\sigma_{ref}} \quad (4.7),$$

where the subscript  $f$  denotes the measurement conditions and  $ref$  means the reference condition for calibration. The effective Rayleigh scattering cross section is the sum of the Rayleigh scattering cross sections of all species in the mixture in question weighted by their mole fractions ( $\chi$ ). Mathematically,

$$\sigma_{effective} = \sum \chi_i \sigma_i \quad (4.8),$$

where  $i$  means the  $i$ th species. A list of the Rayleigh scattering cross section for major combustion species can be found, for example in Ref. [100]. In turbulent reacting flows in which the instantaneous local composition of species can be difficult to estimate, only such major species as CO<sub>2</sub>, H<sub>2</sub>O, CO and N<sub>2</sub> etc. are considered when calculating the effective Rayleigh scattering cross section. This approximation holds true for lean methane/air premixed flames [101].

## 4.5 Laser Doppler Anemometry

Laser Doppler Anemometry (LDA) has been developed to measure flow velocities. This can be achieved by crossing two coherent laser beams with a certain intersection angle. A fringe which shows a periodic dark-and-bright pattern is constructed within the crossed volume. The fringe spacing  $d$  can be calculated if the laser wavelength and the intersection angle are known. As a seeded particle in the flow having the velocity of  $v_d$  passes through the fringe, a burst of signal with an output frequency of  $f_d$  can be detected allowing the velocity to be calculated from:

$$v_d = f_d \cdot d \quad (4.9).$$

The LDA technique was employed for measuring the flow velocities of a series of the LUPJ flames as will be taken up in section 5.1.

# Chapter 5

## Understanding of Turbulent Premixed Combustion in Different Regimes

Combustion in most practical applications takes place under highly turbulent conditions. The interaction between turbulence and flame chemistry has been one of the most important research subjects in the combustion community over the last a few decades. The combustion regime diagram discussed in section 3.2 has been used to qualitatively describe the turbulence/chemistry interaction on the basis of the scaling analysis. For most regimes, including the TRZ regime in the diagram, the flamelet concept has proved to be applicable. However, this may not hold true for the DRZ regime where the Kolmogorov scale is smaller than the reaction zone thickness. It appears that, up to now, there has been no consistent physical understanding of the turbulence/chemistry interaction in the DRZ regime, a fact often leading to the arbitrary assumption that the flamelet concept is always applicable.

A major controversy in connection with the DRZ regime is the question of whether the small eddies can penetrate into the thin reaction zone and thus broaden it. As quote from Driscoll [102], “*a documented distributed reaction zone is defined as a set of measured images of the heat release region or images of radicals such as CH that are spread out over distances that are many times larger than the thickness of a laminar flame*”. However, to the best of the author’s knowledge, no persuasive proof that distributed reactions can be generated through turbulence has been reported.

The aim of this chapter is to explore the characteristics of the flames in the DRZ regime. The LUPJ flames have been investigated using LDA and multi-scalar visualization as presented in Section 5.1, and multi-scalar visualization was also applied to investigate the LSB flames as presented in Section 5.2. A summary of

the present experimental observations of distributed reactions as well as those reported in literatures is provided in Section 5.3. The similarities of the distributed reactions with other combustion concepts are discussed in Section 5.4.

## 5.1 Turbulent Premixed Jet Flames (LUPJ Flames)

A series of LUPJ flames with varying degree of jet speeds (from 11 m/s to 418 m/s) and varying equivalence ratios (from stoichiometric to  $\Phi=0.4$ ) has been investigated in the present work (as reported in Papers V, VI and VII). Flame emission photographs of the investigated LUPJ flames are displayed in Figure 5-1. The flames are referred to as LUPJ $\alpha$ - $\beta$ , where  $\alpha$  represents the code for the  $\Phi$  of the jet flows and  $\beta$  represents the jet flow speeds  $U_0$  in m/s. The pilot coflow flame is run with a fixed  $\Phi=0.9$  and a flow speed of 0.3 m/s.

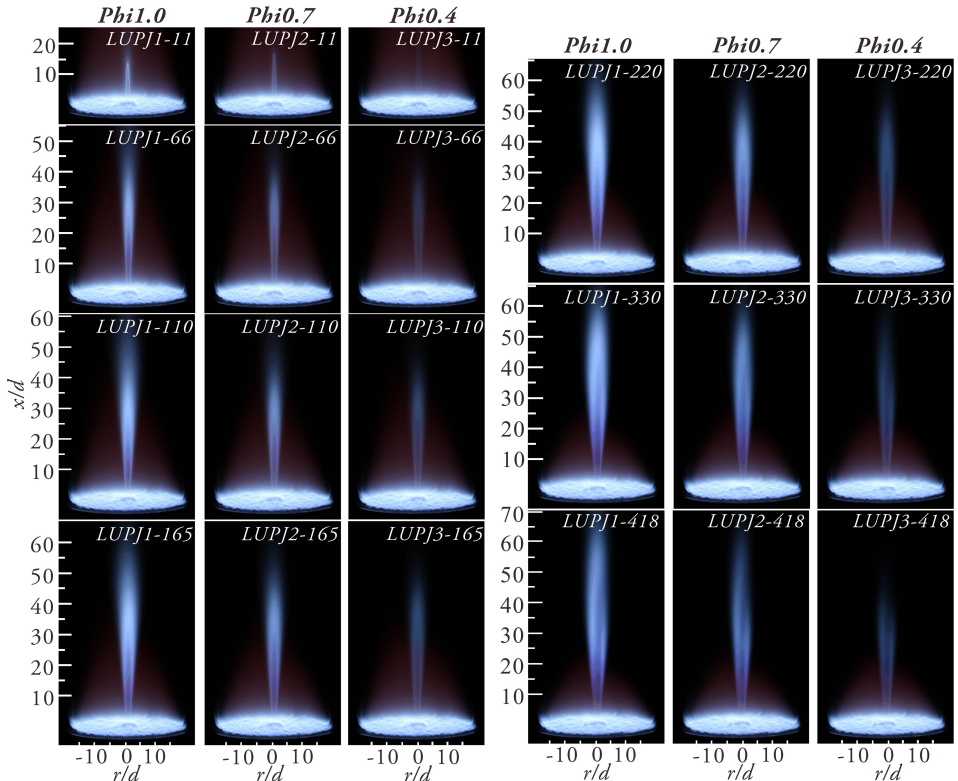


**Figure 5-1** Direct photographs (100 ms exposure time) of the chemiluminescence of the investigated LUPJ flames.

The flow fields of the flames were characterized by use of LDA. Reactive scalars (i.e. OH, CH<sub>2</sub>O, CH and HCO) and temperature (T) were captured instantaneously by three sets of simultaneous imaging measurements which include PLIF of OH/CH<sub>2</sub>O in combination with either CH PLIF, HCO PLIF or the Rayleigh scattering temperature measurements. For the T/CH<sub>2</sub>O/OH set of measurements, quantification of the CH<sub>2</sub>O and OH LIF signals, as discussed in Section 4.3, was achieved by use of the temperature field that was simultaneously measured and the data from the corresponding laminar flames as a calibration source. A set of LUPJ flames was investigated, covering from the laminar flamelet regime to the TRZ regime and to the DRZ regime. One matter of concern was to investigate the characteristics of flames in the DRZ regime which is relatively unexplored. The full dataset obtained for LUPJ flames will be served as a database for model validation and development.

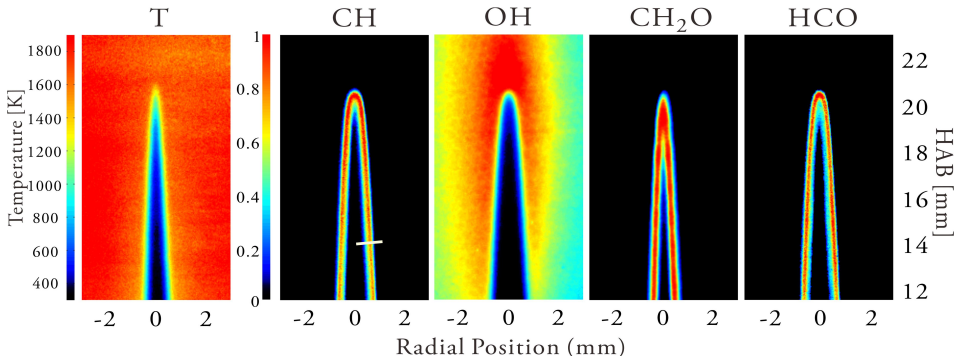


**Figure 5-2** Examples of the quasi-simultaneous imaging of temperature (through the Rayleigh scattering) and of species (from PLIF) for LUPJ-11 shown as an average of 100 frames.

Prior to any measurements in turbulent flames, species LIF and the Rayleigh scattering measurements were carried out in laminar flames. Since the piloted laminar jet flames show excellent stability, the reactive scalars and temperatures measured in different series can be correlated spatially. An example of the laminar LUPJ-11 flame is shown in Figure 5-2 as an average of 100 frames, where a typical laminar flame structure is shown; the CH and HCO layers are nearly identical located upstream of OH and downstream of CH<sub>2</sub>O; a thin thermal layer with a high temperature gradient appears in the vicinity of the CH/HCO layer. This provides good confidence concerning the fidelity of the signals as measured for the turbulent flames to be discussed in the following sections. The laminar flame speed,  $S_L$  and the laminar thermal thickness,  $\delta_L$ , which are important

quantities to calculate the turbulent non-dimensional parameters, have been evaluated from both experimental measurements and CHEMKIN simulation. CHEMKIN simulation of the laminar flames for  $\Phi = 0.4$  is not feasible since the mixture is below the flammability limit for the planar freely propagating flame condition. In addition,  $S_L$  was also determined experimentally using the relation  $S_L = U_0 \times \sin\theta$ , where  $\theta$  is the half angle of the flame cone, and  $\delta_L$  was obtained experimentally from the temperature fields as measured using Rayleigh scattering thermometry, the results being presented in Table 5-1. It is apparent that the pilot coflow flame has a direct heating effect on the laminar jet flames, which, as expected, significantly increases the laminar flame speeds, especially for the leaner cases. To account for the impact of the hot pilot coflow, the experimentally measured laminar speeds and flame thicknesses were adopted in the calculations of  $Ka$  and other non-dimensional parameters as will be described in the next section.

**Table 5-1** Quantities obtained for the investigated laminar flames from both CHEMKIN simulation and experimental measurements

Flame Code	$\Phi$	$U_0$ (m/s)	$S_{L, exp}$ (cm/s)	$S_{L, CHEM}$ (cm/s)	$\delta_{L, exp}$ (mm)	$\delta_{L, CHEM}$ (mm)
LUPJ1-11	1.0	11	42.5	37.5	0.48	0.44
LUPJ2-11	0.7		33.2	19.2	0.60	0.66
LUPJ3-11	0.4		21.4		0.85	

### 5.1.1 Flow Field Characteristics

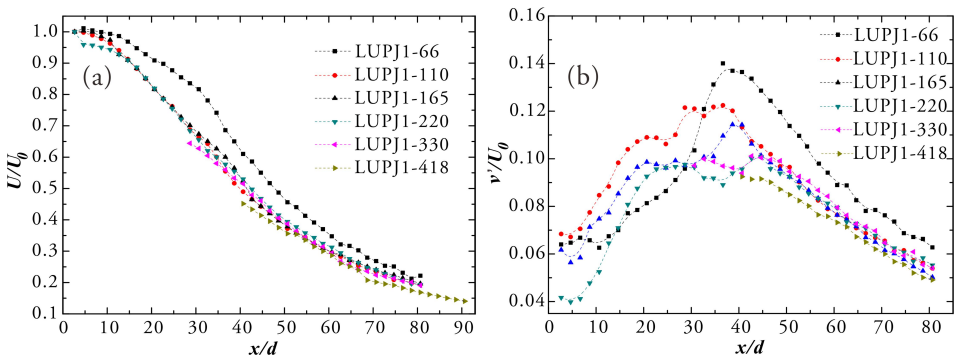


**Figure 5-3** (a) Axial variation of the mean of axial velocity ( $U$ ) and (b) axial variation of the axial rms velocity ( $v$ ) normalized by  $U_0$  for the selected LUPJ flames

The LDA flow field measurements were performed mainly on the stoichiometric LUPJ flames and the analysis of the flow fields is focused on the axial velocity component. The mean axial velocity and its root-mean-square (*rms*) normalized by the jet exit bulk velocity ( $U_0$ ) for the selected LUPJ flames are presented in Figure 5-3 (a) and (b) as a function of axial location ( $x$ ) normalized by jet diameter ( $d$ , 1.5 mm). As the maximum detectable velocity for the employed LDA system is 300 m/s, only part of velocity profiles for the flames LUPJ1-300 and LUPJ1-418 were obtained achieved.

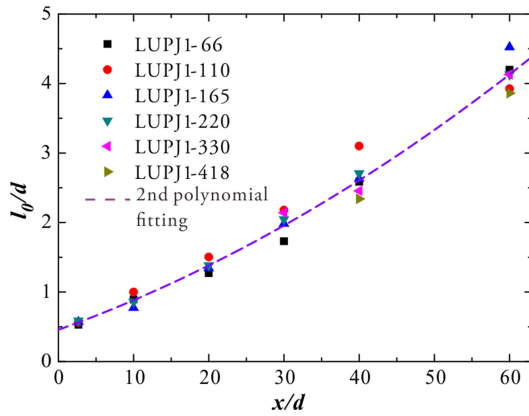


**Figure 5-4** Axial variation of the integral length scale  $l_0$ .

It can be noted in Figure 5-3 (a) that all the normalized axial velocity profiles of the reacting flows coincide and can be fitted into one single profile, independent of the inlet jet speed. Similar self-similarity behavior is known for a fully developed turbulent jet flow under non-reacting conditions [103]. An exception is found for flame LUPJ1-66 whose Reynolds number is considered to be moderate, the turbulent flow is not being fully developed. The profiles of normalized turbulence velocity ( $v'/U_0$ , also referred to as turbulence intensity here) shown in Figure 5-3 (b) can be delimited approximately into three stages. At the first stage ( $0 < x/d < 20$ ), the turbulence intensity increases with  $x/d$ , which latter approaches the second stage, i.e. a relatively plateau region ( $20 < x/d < 40$ ) in which the turbulence intensity reaches its peak value and become somewhat constant. The peak turbulence intensities for the selected flames are in the range of 8% to 12% with the lower jet velocity having higher turbulence intensities in general. The third stage resides approximately in the region  $x/d > 40$  where the turbulence intensity begins to decrease. The flame LUPJ1-66 is again exceptional due to its non-fully developed turbulence.

**Table 5-2** Quantities for the investigated turbulent LUPJ flames

Flame Code	$\Phi$	$U_0$ (m/s)	$Re_{jet}$	$Re_t$	$l_\eta$ ( $\mu m$ )	$\nu'/S_L$	$Ka_{20}$	$Ka_{30}$	$Ka_{50}$	$Da$	LDA
LUPJ1-66	1.0	66	6306	95	96	16	37	25	14	0.39	✓
LUPJ2-66	0.7			97	95	20	59	40	22	0.25	✗
LUPJ3-66	0.4			138	73	40	136	135	72	0.09	✓
LUPJ1-110	1.0	110	10510	190	57	31	71	70	46	0.20	✓
LUPJ2-110	0.7			195	56	40	115	113	74	0.12	✗
LUPJ3-110	0.4			214	53	62	264	261	171	0.06	✗
LUPJ1-165	1.0	165	15764	238	49	39	112	98	73	0.16	✓
LUPJ2-165	0.7			244	48	50	181	158	118	0.10	✗
LUPJ3-165	0.4			267	45	77	417	365	271	0.04	✗
LUPJ1-220	1.0	220	21019	317	39	52	152	151	100	0.12	✓
LUPJ2-220	0.7			325	38	66	246	244	162	0.07	✗
LUPJ3-220	0.4			356	32	103	567	561	373	0.03	✗
LUPJ1-330	1.0	330	31529	476	26	78	327	277	212	0.08	✓
LUPJ2-330	0.7			487	26	99	530	448	344	0.05	✗
LUPJ3-330	0.4			534	24	154	1220	1031	791	0.02	✓
LUPJ1-418	1.0	418	39936	603	22	98	467	394	302	0.06	✓
LUPJ2-418	0.7			617	21	126	756	639	490	0.04	✗
LUPJ3-418	0.4			676	20	196	1739	1470	1127	0.02	✓

In order to quantify  $Ka$ ,  $Da$  and the turbulent Reynolds numbers, the integral scale ( $l_0$ ) is required. In the present study, the radial profiles of the axial velocities were acquired at several axial locations. At a given axial location ( $x/d$ ),  $l_0$  was approximated by the half-width at half-maximum (HWHM) of the radial profile. Figure 5-4 shows the axial variation of  $l_0$  which increases almost linearly with  $x/d$  and is shown to be independent of the jet speed. At the jet exit,  $l_0$  is essentially equal to half of the jet diameter. A second-order polynomial fitting of  $l_0$  was applied, yielding the expression of  $l_0/d = 3.74 \times 10^{-4}(x/d)^2 + 0.039(x/d) + 0.46$ . Without the loss of generality, turbulence velocities and the integral scale at  $x/d=30$  which is approximately the middle of the region of peak turbulence intensity were used in calculating the turbulent characteristic quantities as listed in Table 5-2 for the

investigated LUPJ flames. The availability of the LDA data is also indicated in Table 5-2. For the lean flames where LDA measurements were not performed, the same quantities as in the corresponding stoichiometric flames were adopted. For the flame LUPJ1-418, velocity data at  $x/d=30$  is not available and a turbulence intensity of 10% has been assumed. Note that the  $Ka$  is not a unique value for each individual flame due to the spatial variance of  $l_0$  and the turbulence intensity. To exhibit the spatial variance of  $Ka$ , the  $Ka$  values at  $x/d=20$  and 50 were also estimated and listed in Table 5-2. In general, the  $Ka$  peaks at around  $20 < x/d < 30$ , and then decreases with increasing  $x/d$  due to the increased  $l_0$  and the decreased turbulence intensity downstream. If not specified, the  $Ka$  number appearing in the following text refers to the one at  $x/d=30$ .

### 5.1.2 Multi-scalar Visualizations: Laser diagnostics

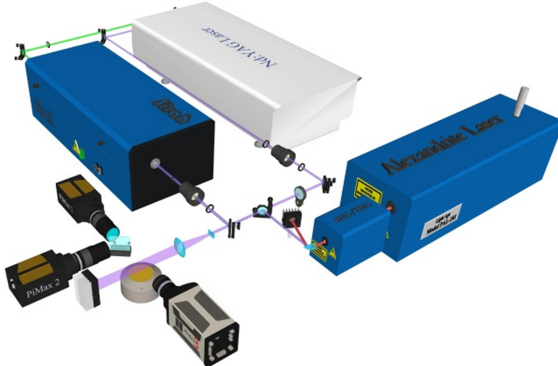


**Figure 5-5** Experimental configuration for high-resolution simultaneous multi-scalar measurements of the LUPJ flames

The multi-scalar visualization system, as shown in Figure 5-5, involves an Nd:YAG laser for  $\text{CH}_2\text{O}$  excitation and Rayleigh scattering thermometry at 355 nm, a dye laser for OH excitation at 283.55 nm, and an alexandrite laser for CH/HCO excitations at 387.3 nm and 259 nm, respectively. Details on LIF excitation-detection schemes involved are elaborated in Section 4.2. All of the laser beams were spatially combined and shaped by sheet-forming optics into a laser sheet of  $\sim 20$  mm height. By slightly adjusting the laser beam divergences using telescope systems, tightly focused laser sheets were obtained at the top of the jet center for all beams. The thickness of the combined laser sheet was measured as being less than 100  $\mu\text{m}$ . Two orthogonally-oriented ICCD cameras were arranged for the detection of OH and  $\text{CH}_2\text{O}$  signals, which were separated using a beam splitter.

The CH (or Rayleigh) signal was detected by the third camera. Optical filters were used for background suppression. The spatial resolution of each scalar was estimated by imaging the finest resolvable patterns on a resolution target (USAF-1951) as summarized in Table 5-3 together with other experimental parameters.

**Table 5-3** Experimental parameters of the multi-scalar visualization system

Species	CH	HCO	T	OH	$\text{CH}_2\text{O}$
<b>Objectives</b>	$f_\# = 1.2$ , $f = 50\text{mm}$	$f_\# = 2$ , $f = 100\text{mm}$	$f_\# = 2$ , $f = 100\text{mm}$	$f_\# = 2.5$ , $f = 150\text{mm}$	$f_\# = 1.4$ , $f = 85\text{mm}$
<b>Spatial resolution</b>	$56^2 \times 100 \mu\text{m}^3$	$56^2 \times 100 \mu\text{m}^3$	$56^2 \times 100 \mu\text{m}^3$	$70^2 \times 100 \mu\text{m}^3$	$70^2 \times 100 \mu\text{m}^3$
<b>Optical Filter</b>	GG400	Longpass 266 nm	Bandpass $355 \pm 5 \text{ nm}$	Bandpass $325 \pm 25 \text{ nm}$	GG400

### 5.1.3 Multi-scalar Visualizations: Jet speed dependence

#### CH/ $\text{CH}_2\text{O}/\text{OH}$ & HCO/ $\text{CH}_2\text{O}/\text{OH}$ series

The CH and HCO radicals, both known as short-lived combustion intermediates, are considered to be good markers of the reaction zone. As discussed in the Sections 3.1 and 3.2, the CH and HCO layers remain thin in both the laminar flamelet regimes and the TRZ regime. A significant broadening of the instantaneous CH or HCO layers would indicate distributed reactions [102]. Figure 5-6 and Figure 5-7 present groups of single-shot images taken from the CH/ $\text{CH}_2\text{O}/\text{OH}$  and HCO/ $\text{CH}_2\text{O}/\text{OH}$  series, respectively, of the stoichiometric flames with various jet speeds. In the flame LUPJ1-66 (cf. Figure 5-6(A) and Figure 5-7(A)), the  $\text{CH}_2\text{O}$  layer is broadened while the CH/HCO layer remains thin, indicating that turbulence starts to disturb the preheat zone of the flame. Therefore, one may refer the flames with thin CH/HCO layers but broadened  $\text{CH}_2\text{O}$  layer to the TRZ regime. Strikingly, as the jet speed increases to 165 m/s, it can be seen in Figure 5-6(B) and Figure 5-7(B) that the broadened CH/HCO layers start at the top of the flame LUPJ1-165. Further increasing the jet speed, i.e. LUPJ1-220/418, the CH/HCO layers become more broadened and evenly distributed at some locations. It has been reported [102] that the measured flamelet could be 3~4 times thicker than that of an unperturbed laminar flame due to the limited spatial resolution, three-dimensional effects and strain rate. However, the achieved spatial resolution better than 100  $\mu\text{m}$  in the present work is sufficient to resolve the thin flame front, and the significant broadening up to a few millimeters that was observed cannot be attributed to three-dimensional effects and strain rate.

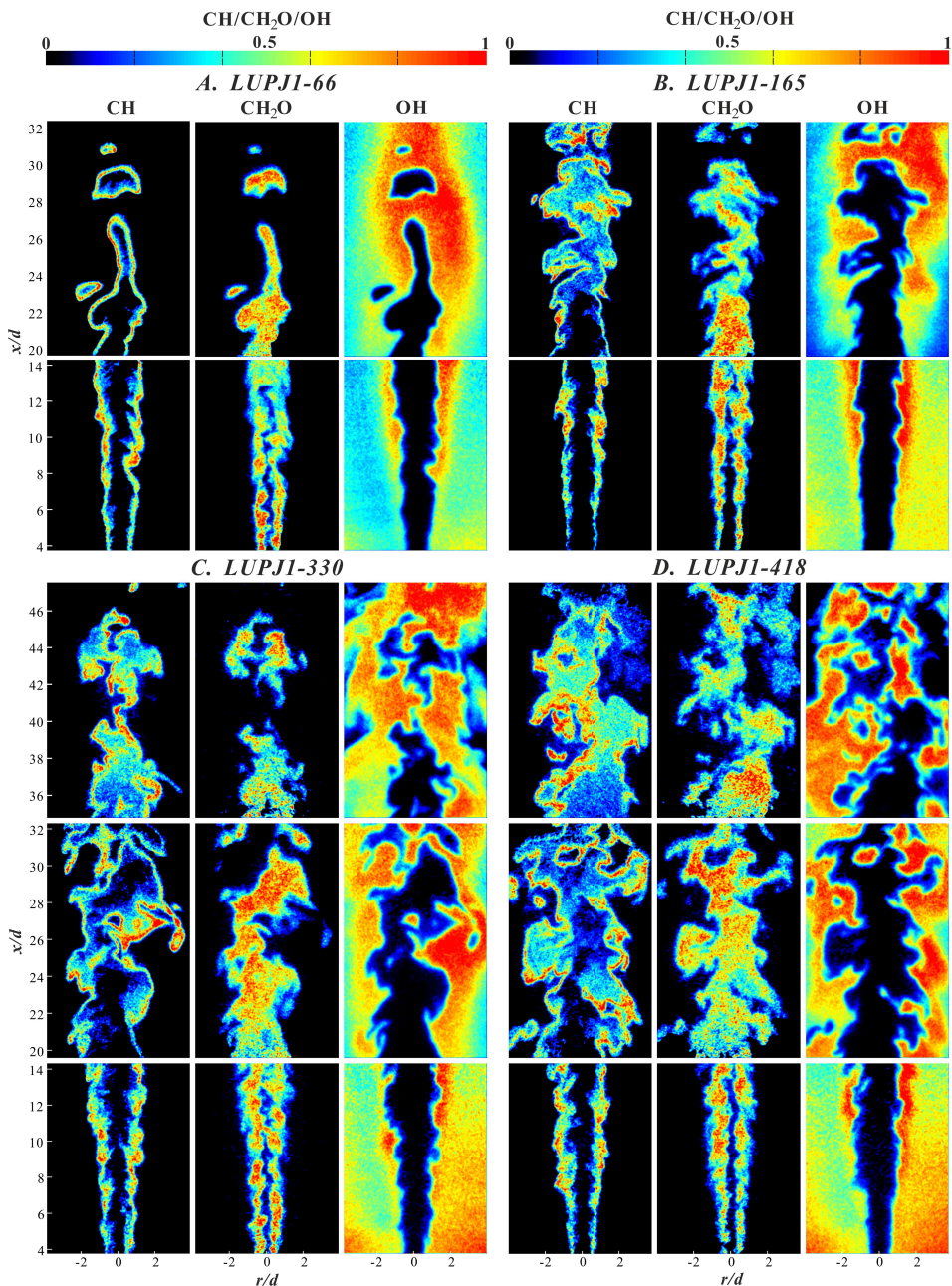


**Figure 5-6** Examples of jet speed dependence from  $\text{CH}/\text{CH}_2\text{O}/\text{OH}$  images for the LUPJ flames (A) LUPJ1-66; (B) LUPJ1-165; (C) LUPJ1-220; (D) LUPJ1-418

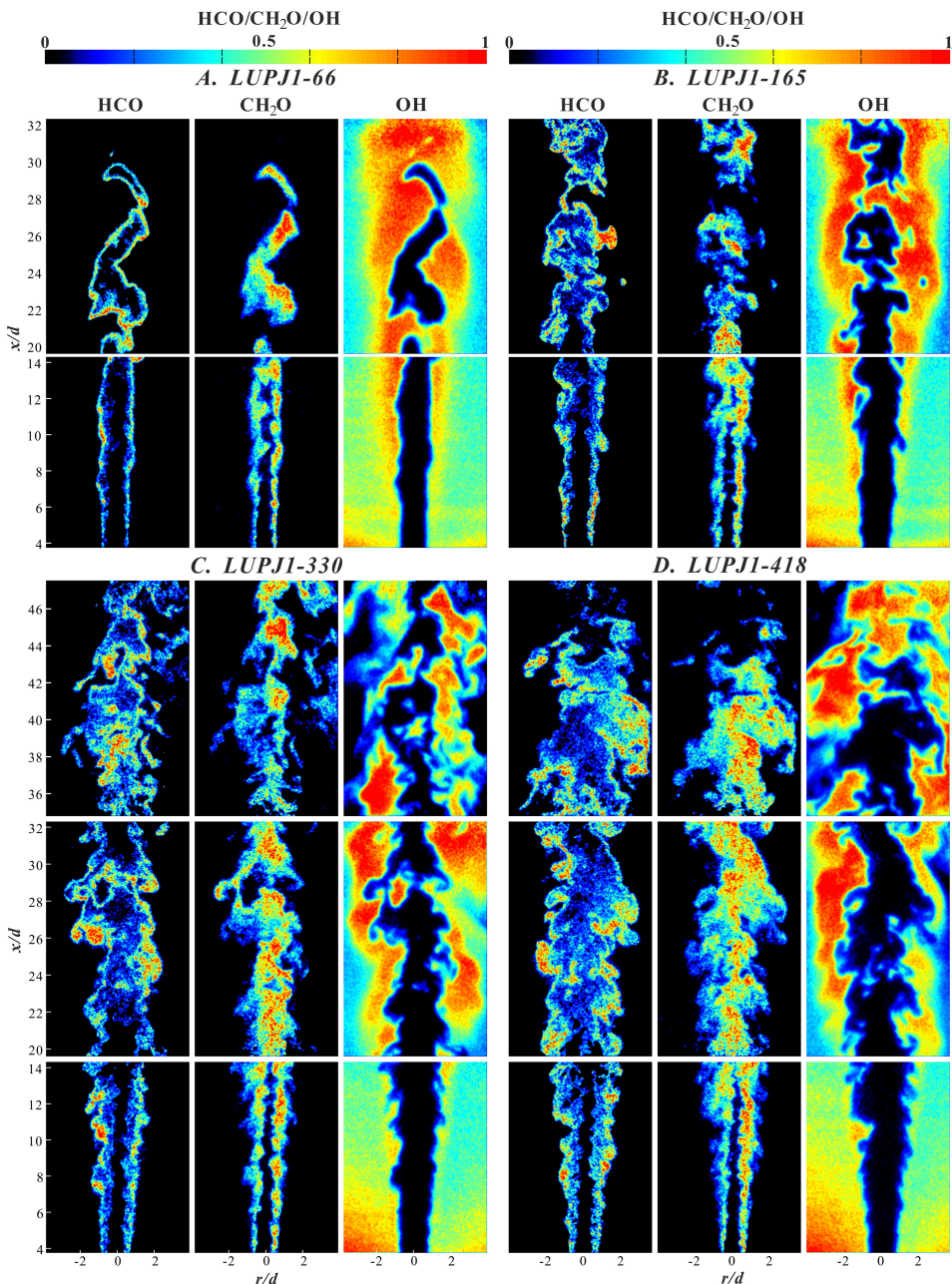


**Figure 5-7** Examples of jet speed dependence from  $\text{HCO}/\text{CH}_2\text{O}/\text{OH}$  images for the LUPJ flames (A) LUPJ1-66; (B) LUPJ1-165; (C) LUPJ1-220; (D) LUPJ1-418

Reflecting on Driscoll's definition of an experimentally documented distributed reaction zone as introduced at the beginning of this chapter, to the best of the authors' knowledge, the present observations, through direct visualizations of the reaction zone markers, i.e. CH and HCO, provide the first experimental verification of a distributed reaction zone generated by rapid turbulence mixing. In contrast to this, because of the high level of stretch and heat loss exerted by intense turbulence, high  $Ka$  flames have also been shown to be shredded [104] or quenched [105-107] before being broadened. From the present experimental results, it can be concluded that distributed reactions can be achieved and flames like the investigated LUPJ ones do not necessarily extinguish at high  $Ka$  if protected properly by a hot coflow.

As shown in Figure 5-6 and Figure 5-7, the flames (i.e. LUPJ1-165/220/418) with observed distributed reactions exhibit a progressive broadening of the CH/HCO layers along the axial direction, which is partially associated with the progressive increase of the integral scale as shown in Figure 5-4. The thickness of the distorted inner layer may be confined within the integral length scale  $l_0$ . Accordingly, even though the inner layer is strongly distorted by the turbulence eddies, it can be virtually thin if  $l_0$  is small and on the same order of magnitude of the inner layer thickness. This may be the case for the flames LUPJ1-220/418 near the jet exit  $\sim x/d=10$  where the  $Ka$  is expected to be high while the CH/HCO layer is still thin. The features concerning the correlations between the measured scalars were also found to be interesting. First, the primary OH and  $\text{CH}_2\text{O}$  signals were located in mutually exclusive regions, and CH/HCO was found to be able to penetrate slightly deeper into the OH regions than  $\text{CH}_2\text{O}$  did. Secondly, CH/HCO can markedly overlap with  $\text{CH}_2\text{O}$ . The stronger CH/HCO signals generally correspond to the regions where  $\text{CH}_2\text{O}$  signal was weak, and vice versa. This is consistent with the nature of fuel oxidation chemistry, which, as also shown in Figure 4-2, proceeds sequentially from  $\text{CH}_4$  through methyl radicals ( $\text{CH}_3$ ), formaldehyde ( $\text{CH}_2\text{O}$ ) and then formyl radical (HCO) in regardless of the reaction mode [23]. Even in the case of high  $Ka$  flames, owing to the rapid reaction rates in reactions associated with the OH radicals, OH radicals tend to not coexist at an appreciable level together with the species, such as  $\text{CH}_2\text{O}$  which stem from fuel stream. For the same reason, the OH radicals of high concentration (signifying the post-flame region) are only visually manifested themselves in patchy regions of no  $\text{CH}_2\text{O}$ , as also observed by Dunn et al. [108] and Temme et al. [109], whereas OH radicals of low concentration (which could be even lower than the present OH PLIF detection limit of  $\sim 100$  ppm) may still overlap with  $\text{CH}_2\text{O}$ . The GRI 3.0 kinetic mechanism [52] indicates CH to be formed primarily via the reaction:



whereas HCO through the reactions:



Thus, the appearance of appreciable CH/HCO signals suggests the previous presence of OH and/or H radicals which give rise to lesser amount of CH<sub>2</sub>O (and likely of CH<sub>2</sub>).

### T/CH<sub>2</sub>O/OH series

Figure 5-8 shows examples of quantitative T/CH<sub>2</sub>O/OH measurements of the stoichiometric flames at various jet speeds. To facilitate comparison, iso-intensity contours of CH<sub>2</sub>O (10% of maximum signal) were superimposed on the temperature fields. At the lower axial position (i.e.  $7 < x/d < 16$ ), the thermal layer was found to be relatively thin for all the studied flames, and it becomes thicker with increasing jet speed. The CH<sub>2</sub>O contours show a similarity to the thermal layer, and a high level of CH<sub>2</sub>O correspond to the region where temperature is relatively low. Along the axial direction, the thermal thickness is continuously increasing as indicated by the vitiated temperature gradient. More hot regimes ( $T > 1200$  K) resides within the CH<sub>2</sub>O contours as the jet speed increases, indicating the increasingly rapid transport of heat by turbulence eddies as expected for flames in the TRZ and DRZ regimes (see the discussion in Section 3.2 as well as Table 5-2). A slightly reduced temperature of the coflow flame at  $20 < x/d < 33$  is also noticeable for the flames LUPJ1-330/418, implying an increased influence of the cold ambient air entrainment at high jet speeds. Further downstream ( $37 < x/d < 49$ ), the turbulent mixing with the ambient air further reduces the maximum flame temperature to  $\sim 1500$  K along with reduced temperature gradients. It has been demonstrated that turbulence eddies can be greatly weakened after passing through the flame front due to the dilation effect [40, 41]. Along the axial direction, the dilation effect is expected to be continuously reduced as the temperature field is found to be more and more homogeneous. The occurrence of distributed reactions together with the observed relatively homogeneous temperature field supports the hypothesis regarding the DRZ regime as described in Section 3.2. In this regime, flame propagation is greatly suppressed by rapid turbulence mixing so that no distinct localized temperature gradient and flame front can be observed. Note that such a feature has also been used to characterize the concepts of flameless oxidation [110] and Mild combustion [111].

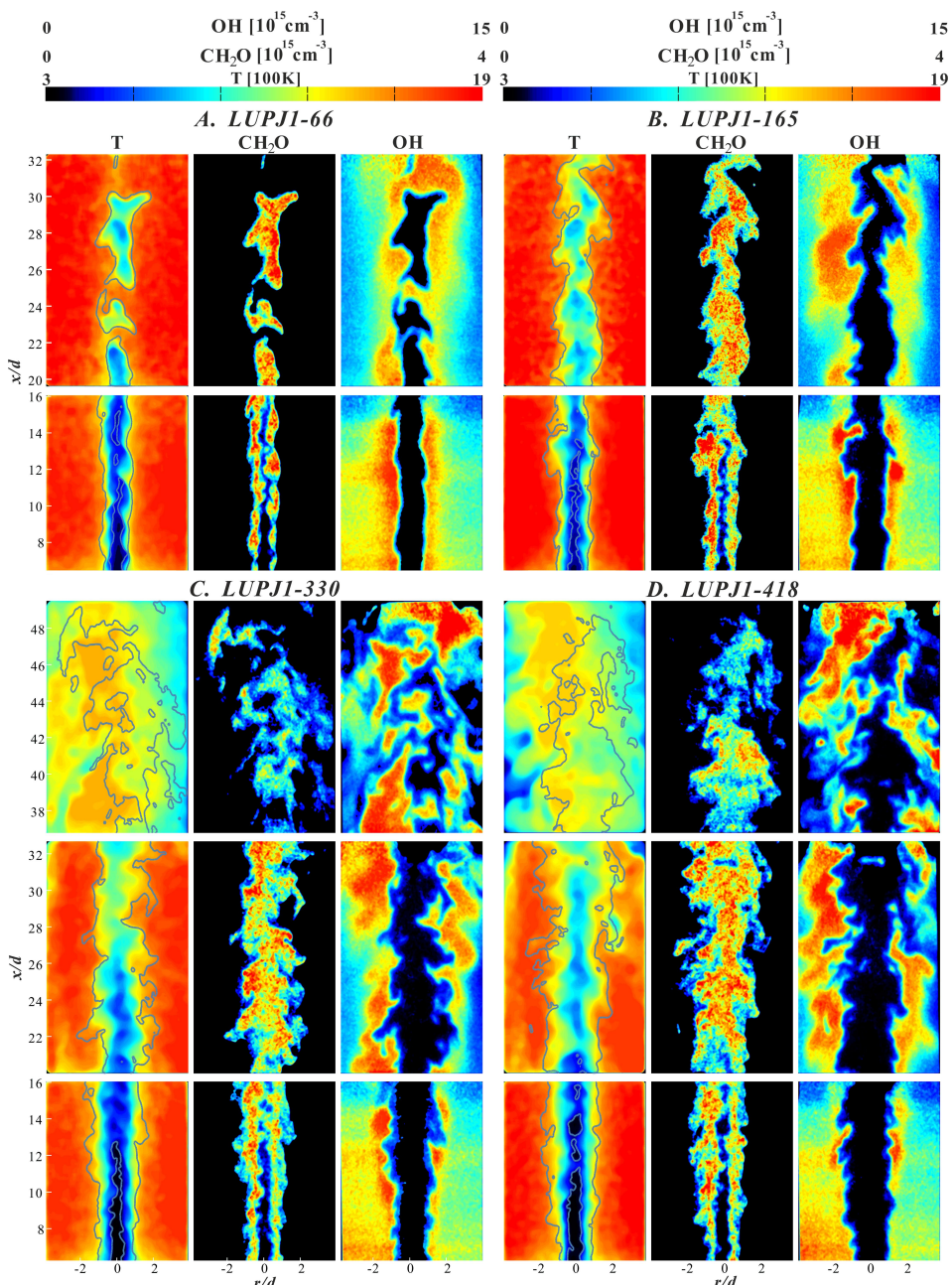


**Figure 5-8** Illustration of jet speed dependence from  $T/\text{CH}_2\text{O}/\text{OH}$  images for the selected flames (A) LUPJ1-66; (B) LUPJ1-165; (C) LUPJ1-220; (D) LUPJ1-418; iso-intensity contours of  $\text{CH}_2\text{O}$  were superimposed on temperature fields for comparison.

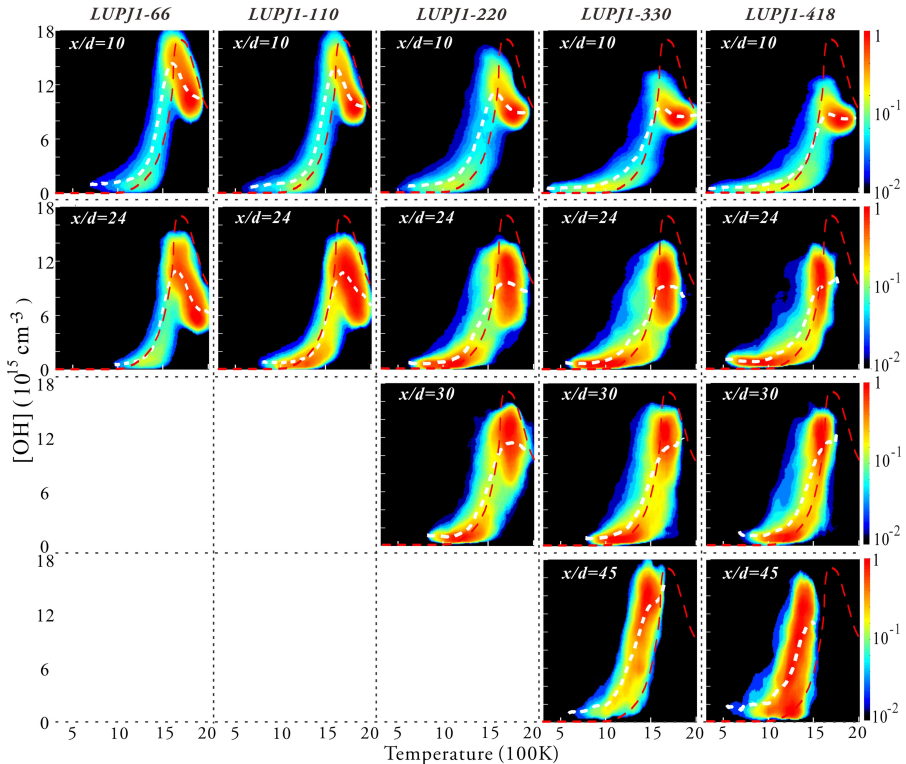


**Figure 5-9** OH/T JPDF for five selected flames (LUPJ1-66, LUPJ1-110, LUPJ1-220, LUPJ1-330 and LUPJ1-418) at four axial locations ( $x/d=10, 24, 30$  and  $45$ ).

To quantify the effects of turbulence on the flames, joint probability density functions (JPDF) of OH concentration/temperature for the selected flames at several axial locations are presented in Figure 5-9. The logarithm-scale colormap in the JPDF plots denotes the probabilities with red being the maximum and black being the minimum. The white dashed curves are the mean OH concentration weighted by its probabilities as a function of temperature, while the red curves show the OH/T correlation from the experimental measurement of the corresponding laminar flame, LUPJ1-11. In the laminar flame (red curve), the OH concentration peaks approximately in the reaction zone known as the super-equilibrium OH, followed by a decrease of the OH concentration to an equilibrium value in the product zone. Little OH radicals exist in the region with temperature below 1200K. In contrast to this, an appreciable amount of OH can be found in the lower temperature region as shown in Figure 5-9 for the selected flames. At  $x/d=10$ , with increasing jet speed, it can be seen that OH can be found in the regions of temperature below 600 K and the possibility of finding OH in the

temperature range of  $900 \text{ K} < T < 1400 \text{ K}$  is also enhanced. This observation is consistent with results of recent DNS studies of high  $Ka$   $\text{CH}_4/\text{air}$  flames [112, 113], in which it was shown that the turbulence eddies can effectively transport the reactive radicals (e.g. H and OH) from the high temperature reaction zone to the low temperature regions ( $\sim 500 \text{ K}$ ), which is responsible for an appreciable amount of heat release in the low temperature regions. Subsequently, with an increasing jet speed (hence increased turbulence level), the peak concentration of radicals (e.g. H and OH) is decreased due to the rapid transport of these radicals to the low temperature regions. At locations further downstream ( $x/d > 10$ ), even higher probability of having OH radicals at the low temperature regions can be seen as the turbulence intensity increases along the axial direction (until  $x/d$  about 40) and therefore the transport of radicals by turbulence eddies becomes even faster. At  $x/d=10$ , the distribution of OH JPDF shares certain similarity to that in laminar flames, a matter which is less clear, however, at locations downstream of the highly turbulent flames (LUPJ1-220/330/418) as a consequence of a strong turbulent perturbation in the product zone and at the flame front. Close to the flame tip ( $x/d= 45$ ) where the temperature field is rather homogeneous and reactions are distributed, OH appears to be spread over a wide range of concentrations confined mostly in the temperature range from 1000 K to 1500 K with nearly equal probabilities.

In Figure 5-10, JPDF plots for  $\text{CH}_2\text{O}$  concentration versus temperature are presented. Note that the colormap in Figure 5-10 is linear. The experimentally determined  $\text{CH}_2\text{O}/T$  profile (red curve) from the laminar LUPJ1-11 flame is plotted for comparison. At  $x/d=10$ , the  $\text{CH}_2\text{O}/T$  JPDF of turbulent flames qualitative agrees with the  $\text{CH}_2\text{O}/T$  profile of the laminar flame. The  $\text{CH}_2\text{O}$  concentration rises with temperature and peaks at around 1000K for the flames LUPJ1-66/110 and 800K for the flames LUPJ1-220/330/418. Subsequently, the  $\text{CH}_2\text{O}$  concentration decreases with increasing temperature. This is analogous to the process of fuel decomposition reactions that produce  $\text{CH}_2\text{O}$  (seen as the rising branch), which is then followed by the oxidization of  $\text{CH}_2\text{O}$  at high temperature (seen as the decreasing branch). The shift of the temperature of the peak  $\text{CH}_2\text{O}$  concentration towards lower temperature with increasing jet speed indicates that the fuel decomposition was accelerated by the enhanced transport of radicals under conditions of stronger turbulence. At locations downstream of the selected flames, the consumption branch of the  $\text{CH}_2\text{O}$  JPDF profiles at high temperatures remains a similar trend, although the distribution departs from the corresponding laminar profile. Contrarily, the rising branch at low temperatures in the  $\text{CH}_2\text{O}$  JPDF profiles due to the fuel decomposition is greatly reduced or has disappeared

completely. This is owing to that the dominant fuel decomposition process has been completed at the upstream locations where  $\text{CH}_2\text{O}$  is generated and transported by the flow to locations downstream. This is supported by the measurements of Sjöholm et al. [114] under similar flame conditions which show lesser amounts of fuel to exist downstream ( $x/d > 20$ ). This suggests that the disappearance of the rising branch in  $\text{CH}_2\text{O}$  JPDF profiles is attributed to the absence of fuel at locations downstream. Note that  $\text{CH}_2\text{O}$  is located mostly within the area delimited by the red curve as at  $T > 1600$  K, above which  $\text{CH}_2\text{O}$  is quickly consumed. At  $x/d = 45$ ,  $\text{CH}_2\text{O}$  exists mainly within the temperature range of 1100 K to 1500 K which, as shown in Figure 5-9 at the same axial location, coincides with the regions where most of the OH radials also exist.

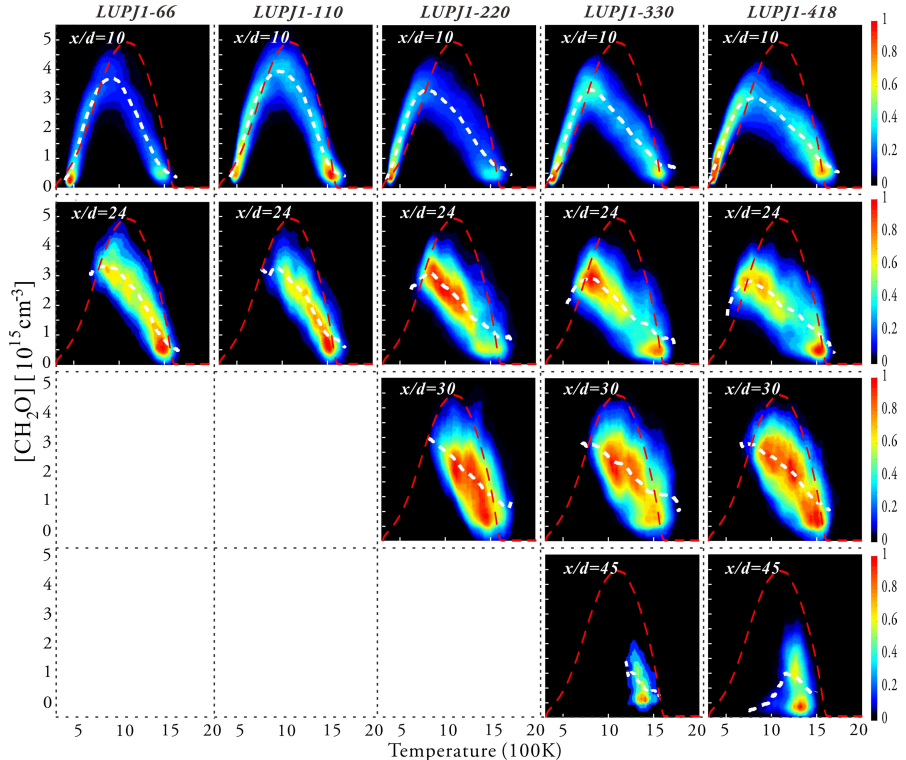


**Figure 5-10**  $\text{CH}_2\text{O}/T$  JPDF for five selected flames (LUPJ1-66, LUPJ1-110, LUPJ1-220, LUPJ1-330 and LUPJ1-418) at four axial locations ( $x/d = 10, 24, 30$  and  $45$ ).

It has been shown in Figure 5-6 and Figure 5-7 that distributed HCO/CH radicals can be substantially overlapped with  $\text{CH}_2\text{O}$  at  $x/d > 35$ . Accordingly, it can be expected that distributed HCO/CH radicals also exist in the same temperature

range (1100 K to 1500 K) as  $\text{CH}_2\text{O}$ . In a flame similar to LUPJ1-165 but with a smaller pilot flame (20 mm in diameter), Li et al. [31] has demonstrated that the top of the flame can be completely quenched due to significant heat loss by the ambient air entrainment, which is contrary to the observation of a broadened reaction zone at the top of the flame in LUPJ1-165 (cf. Figure 5-6(B) and Figure 5-7(B)). This difference indicates that temperature could be important for the occurrence of the distributed reactions. Within the temperature range from 1100 K to 1500 K, the temperature is above the cross-over temperature which sustains the flame and prevents extinction, whereas at the same time being sufficiently low so that the oxidation reactions do not proceed as quickly as they would in a laminar flame.

### 5.1.4 Multi-scalar Visualizations: $\Phi$ dependence

Given the same turbulent intensity, it is expected that the penetration of turbulence eddies into the thin reaction zone could be facilitated under fuel lean conditions in which the  $S_L$  decreases and  $\delta_L$  increases noticeably. Figure 5-11 shows examples of  $\Phi$  dependence of the scalar fields for two jet speed, 110 m/s (left) and 418 m/s (right) from the CH/ $\text{CH}_2\text{O}/\text{OH}$  series.

In the left column of Figure 5-11, a clear transition from a thin (i.e. LUPJ1-110) to a broadened/distributed (i.e. LUPJ2/3-110) CH layer is shown as  $\Phi$  changes from 1.0 to 0.4. The corresponding  $Ka$  values for LUPJ2-110 and LUPJ3-110 are 113 and 261, respectively. Figure 5-11 (C) indicates that the CH layer can be both thin and significantly broadened at the same axial location, suggesting a non-uniform distribution of turbulence length scales in space. The scalar profiles across the flame fronts along the red lines shown in Figure 5-11 (A) and (C) are plotted in Figure 5-12. In contrast to the typical flamelet structure shown in Figure 5-12 (a) for LUPJ1-110, LUPJ3-110 shows a rather broadened CH profile up to ~3mm. In addition, the penetration of OH at low concentration levels is also clearly in evidence. In the right column of Figure 5-11, distributed CH has been shown for all the flames (i.e. LUPJ1/2/3-418), the  $Ka$  values of which range from 394 to 1470 greatly exceeding the boundary of DRZ regime. The major difference among them is found that the CH layer of the flame LUPJ1-418, although distributed, appears more concentrated on the OH/ $\text{CH}_2\text{O}$  interface, whereas the flames LUPJ2/3-418 exhibit no distinct local CH peak at the OH/ $\text{CH}_2\text{O}$  interface. This can be attributed to the decreasing of  $Da$  (see Table 5-2) as a consequence of reduced flame reactivity under leaner conditions. The HCO layer as a function of

$\Phi$  shows behaviors similar to those of CH. Examples of this are provided in the Appendix I. In addition, the mean radial profiles of measured scalars from the T/CH<sub>2</sub>O/OH dataset at various  $x/d$  as a function of jet speed and equivalent ratio are presented in Appendices II and III by way of a reference.

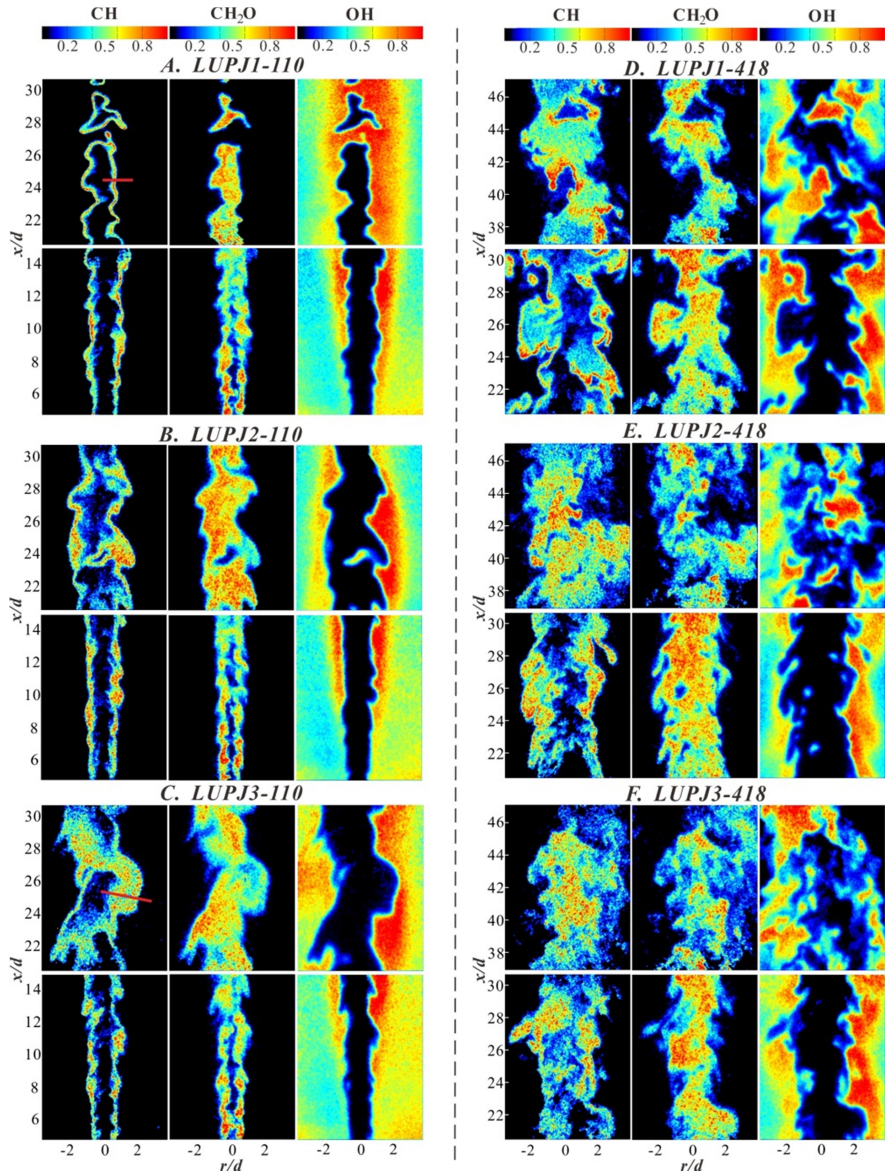


**Figure 5-11** Examples of equivalence ratio dependence of two given jet speeds, 100 m/s (left) and 418 m/s (right) from the CH/CH<sub>2</sub>O/OH series.

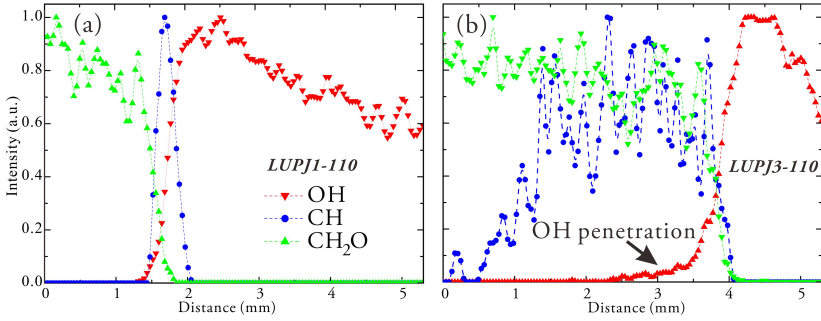


**Figure 5-12** Profiles of measured scalars across the flame front for the flames (a) LUPJ1-110 and (b) LUPJ3-110

It is of interest to examine the boundary of the DRZ regime. One can note that the different  $\Phi$  values for the flames (LUPJ1-165 and LUPJ2-110), which exhibit the transition from the thin to broadened CH/HCO layer have characteristic  $Ka$  numbers rather close to  $Ka=100$  which is consistent with the boundary predicted by Peters [21]. One should also note, however, that the CH/HCO layers downstream ( $x/d>30$ ) are in generally broader than those upstream (e.g.  $x/d=20$ ), whereas the  $Ka$  values at  $x/d>30$  are typically smaller than those at  $x/d=20$ . This indicates that the boundary of the DRZ regime in the present flames is not only a function of the local  $Ka$  number but also depends on other parameters, such as the local turbulence length scales and the streamwise history effect. Cautions have to be taken when interpreting the boundary of  $Ka=100$  in the present flames.

### 5.1.5 Flame tip structures

From the laminar flamelet perspective, a broken OH layer can be viewed as experimental evidence of local flame quenching. Global quenching could be recognized as the absence of OH radicals which indicates the complete termination of high-temperature reactions. This can be different, however, in case of the flames in the DRZ regime. In contrast to previous examples in Section 5.1.3 in which distributed CH/HCO and  $CH_2O$  are mostly enclosed by the OH layer, the top of the flame (cf. Figure 5-13) can also occasionally either be (A) partially enclosed by OH or (B) nearly absent of OH (termed as “quenched” in the figure) due to ambient air entrainment. The associated scalar fields of CH,  $CH_2O$ , HCO and T from the various measurement series are presented accordingly. Overall, the temperature is higher in the regions containing OH (~ 1300 K), and the

“quenched” case shows a lower maximum temperature due to stronger ambient air entrainment. Under both conditions,  $\text{CH}_2\text{O}$  is widely spread due to the lack of consumption mechanism at relatively low temperature [31].

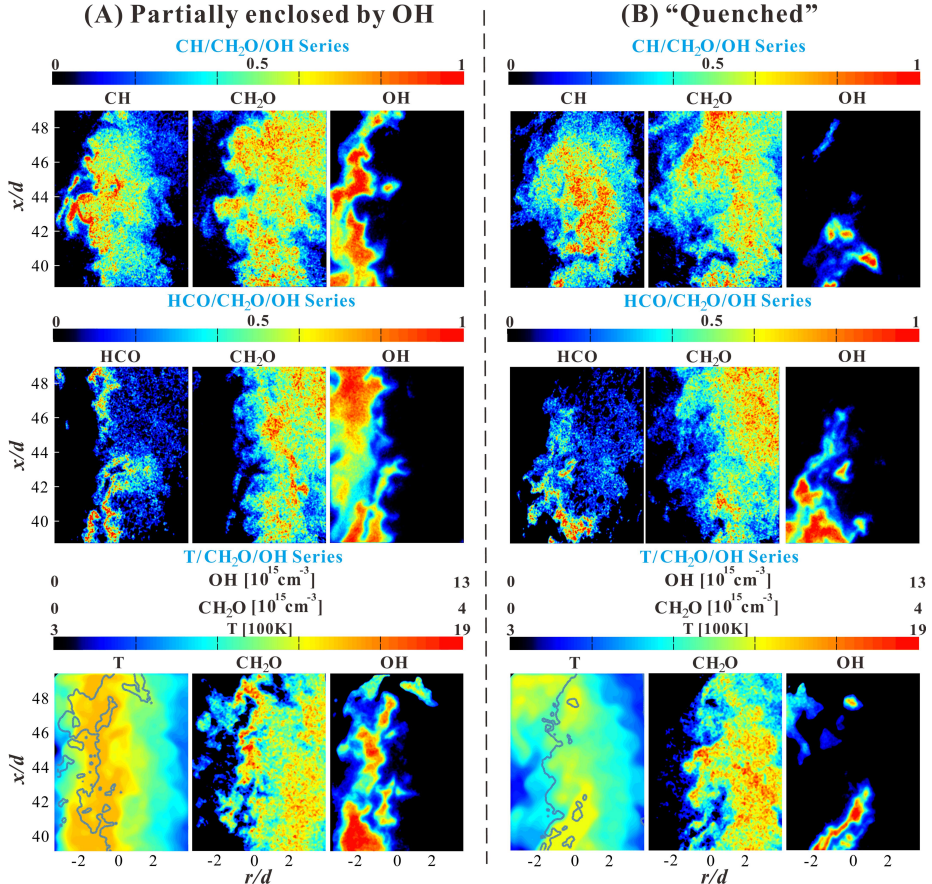


**Figure 5-13** Examples of simultaneous images from each series at the top of flame LUPJ1-418 with (A) flame partially enclosed by OH (B) “quenched”; iso-intensity contours of  $\text{CH}_2\text{O}$  were superimposed on the temperature fields for comparison.

Interestingly, however, the flame front markers, i.e. CH and HCO are not quenched and still appear distributed. This indicates that flame quenching in the context of distributed reactions is more reaction/species specific. Reactions which were restricted in the flamelet manifolds were activated as a consequence of the increased availability of radicals through turbulence mixing. CHEMKIN simulation using GRI3.0 mechanism shows that both CH and HCO can be

quickly oxidized through reactions with  $O_2$  within  $\sim$  ten nanoseconds which are too short to allow any significant transport by turbulence or diffusion to take place. Accordingly, CH and HCO radicals must be locally generated through reactions that take place. In the “quenched” case (cf. Figure 5-13 (B)), one can note that HCO appears to be more concentrated on the  $CH_2O/OH$  interface, whereas CH shows a wider and uniform distribution. As discussed in Section 5.1.3, CH is formed through reaction R(5.1) which involves the H radical, whereas both H and OH radicals contribute to the formation of HCO through reactions R(5.2) and R(5.3). This implies that H radicals could spread wider than OH, and might still exist when OH radicals are low in occurrence or absent. Without the presence of OH radicals, H radicals can still contribute to the generation of HCO and CH. When OH is available, the reaction R(5.3) will play an important role in giving rise to higher HCO signal at the  $CH_2O/OH$  interface. This issue remains to be clarified through future experiments and numerical simulation.

### 5.1.6 Flame front Markers

As discussed in Section 4.2.1, both experiments and numerical simulations support the HCO radical being one of the best HRR/flame front markers for both laminar and turbulent methane/air flames. However, prior to the development of a satisfactory single-shot HCO PLIF technique, instantaneous visualization of the HCO radical is barely feasible. Instead, because high-quality simultaneous imaging of OH and  $CH_2O$  is experimentally feasible through PLIF, the product of OH and  $CH_2O$  which has been shown to be responsible for the generation of HCO through the reaction R(5.3) in laminar flames has been proposed for marking the HRR indirectly [16, 115]. Although this method has only been verified in quasi-laminar flames, it has been employed extensively in studying various turbulent flames [116-122]. The HCO/ $CH_2O/OH$  dataset of the present work provides a unique possibility to re-examine the correlation between HCO and the quantity of  $OH \times CH_2O$  under turbulent flame conditions.

As shown in Figure 5-14, the measured scalars (i.e. HCO,  $CH_2O$  and OH) and the quantities that were derived (i.e.  $CH_2O \times OH$ ,  $HCO \times OH$  and the normalized gradient of OH,  $Grad[OH]$ ) from the flames LUPJ1-110 and LUPJ1-418 are presented. Since all the measured scalars are qualitative, it is their spatial structures rather than their intensity strengths which are compared. In laminar flames as demonstrated in Section 3.1 (cf. Figure 3-2), the quantities, HCO,  $CH_2O \times OH$  and  $Grad[OH]$  essentially coincide with each other. They are

confined to a thin layer in which the major reactions take place. The quantity  $\text{HCO} \times \text{OH}$  is also presented to show an even thinner layer, which might be regarded as a smaller chemical length scale than the reaction zone thickness (marked by HCO). Nevertheless, the meaning of this quantity in chemical term is in need of further investigations. For now, it is simply interpreted as the overlapping layer of OH and HCO which is presented here to illustrate the effect that turbulence has on its thickness.

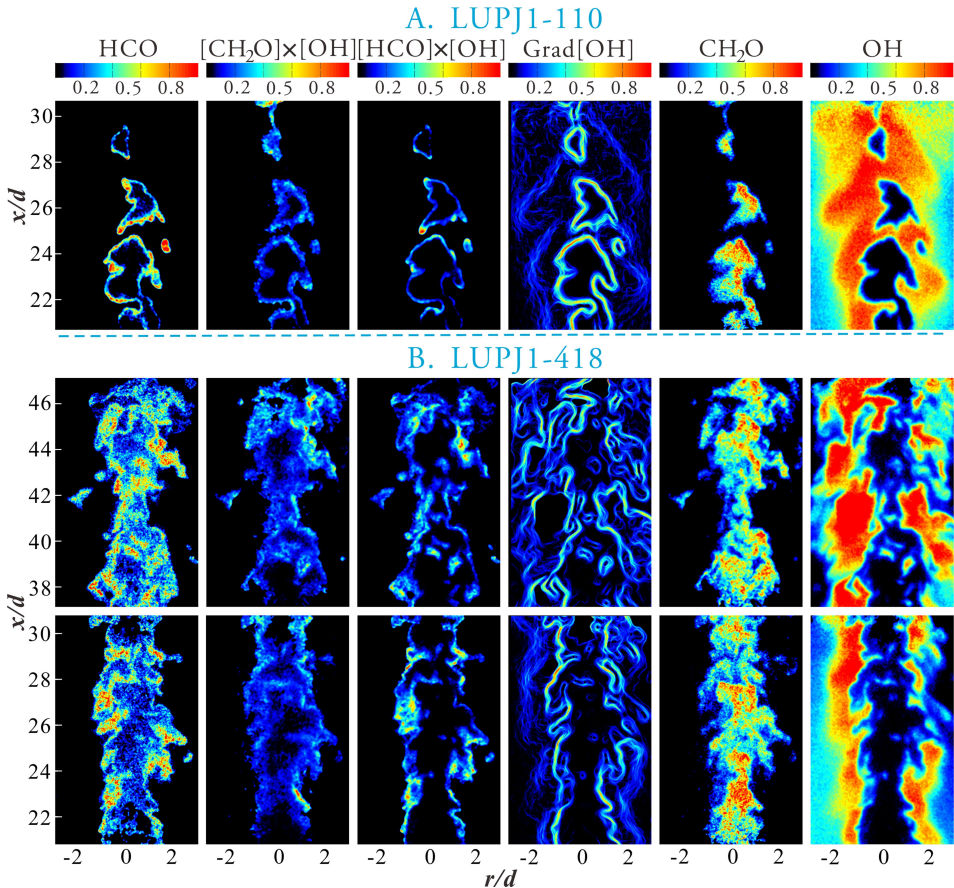


**Figure 5-14** Examples of snapshots of measured scalars and their derivatives (i.e.  $\text{CH}_2\text{O} \times \text{OH}$ ,  $\text{HCO} \times \text{OH}$  and normalized  $\text{Grad}[\text{OH}]$ ) from the flames LUPJ1-110 and LUPJ1-418 from the  $\text{HCO}/\text{CH}_2\text{O}/\text{OH}$  measurement series

It is seen from Figure 5-14 (A) that for flame LUPJ1-110 the first four quantities are generally thin and show close agreement in regard to their spatial

distributions. Careful inspection also shows that, although  $\text{CH}_2\text{O} \times \text{OH}$  is believed to reflect the HCO distribution, the  $\text{CH}_2\text{O} \times \text{OH}$  layer appears more blurred than the HCO layer and the other quantities. This can be attributed to the fact that  $\text{CH}_2\text{O}$  and OH overlap in regions in which the intensity strengths of both are weak. It thus appears that the  $\text{CH}_2\text{O} \times \text{OH}$  layer can be strongly affected by the limited SNRs and the non-ideal background subtractions. Figure 5-14 (B) shows scalars measured in the flame LUPJ1-418 in the DRZ regime. As can be seen, the  $\text{CH}_2\text{O} \times \text{OH}$  layer is broadened which is consistent with the observation reported by Temme et al. [109], and the outer edges of the  $\text{CH}_2\text{O} \times \text{OH}$  layer are similar in qualitative terms with the HCO layer. However, comparing with the HCO layer and with other quantities, the detail structures cannot be easily discerned from those of the  $\text{CH}_2\text{O} \times \text{OH}$  layer. It is of interest to note that the  $\text{HCO} \times \text{OH}$  layer is likewise broadened but to a lesser extent than the first two quantities at the left shown in Figure 5-14 (B). Yet despite the OH gradients stemming from the flame product regions, the primary part of  $\text{Grad}[\text{OH}]$  still seemingly remains thin, but many finer filament-like structures on the  $\text{Grad}[\text{OH}]$  field can be observed especially in the regions where the  $\text{CH}_2\text{O}$  signals prevail. This can be seen as associated with the fact that an appreciable amount of OH has been transported away by turbulence to the  $\text{CH}_2\text{O}$  region as was discussed earlier. Comparisons with scalars measured and derived from the  $\text{CH}/\text{CH}_2\text{O}/\text{OH}$  dataset, which are presented in the Appendix IV, also show similar results.

Figure 5-15 shows the measured scalars (i.e. T,  $\text{CH}_2\text{O}$  and OH) and their derivatives (i.e.  $\text{CH}_2\text{O} \times \text{OH}$ , the temperature gradient  $\text{Grad}[T]$  and the normalized OH gradient  $\text{Grad}[\text{OH}]$ ) from the flames LUPJ1-66 and LUPJ1-418. The absolute values of the colormap for the  $\text{Grad}[T]$  are indicated in the left-hand corner of the  $\text{Grad}[T]$  images with the unit of 100 K/mm. For the flame LUPJ1-66 in the TRZ regime (cf. Figure 5-15(A)), more complex structures in the  $\text{Grad}[T]$  field can be seen, these being less similar to the layers marked by  $\text{CH}_2\text{O} \times \text{OH}$  and  $\text{Grad}[\text{OH}]$  which indicates a significant distortion of the turbulence in the temperature fields. The complex  $\text{Grad}[T]$  field consists of a part having distinct high thermal gradient fronts similar to those that can be seen in the flamelet regimes [29] and of a part having fine filament-like structures in which the thermal gradients are less pronounced. Also, the thermal gradients are also gradually reduced along the axial direction. For the flame LUPJ1-418 in the DRZ regime (cf. Figure 5-15(B)), the filament-like structures are dominant on the  $\text{Grad}[T]$  field, and the maximum value of the thermal gradient is reduced from 1500 K/mm (for LUPJ1-66 case) to 1000 K/mm which is consistent with the one reported by Dunn et al. [123] for flames with a similar burner configuration.

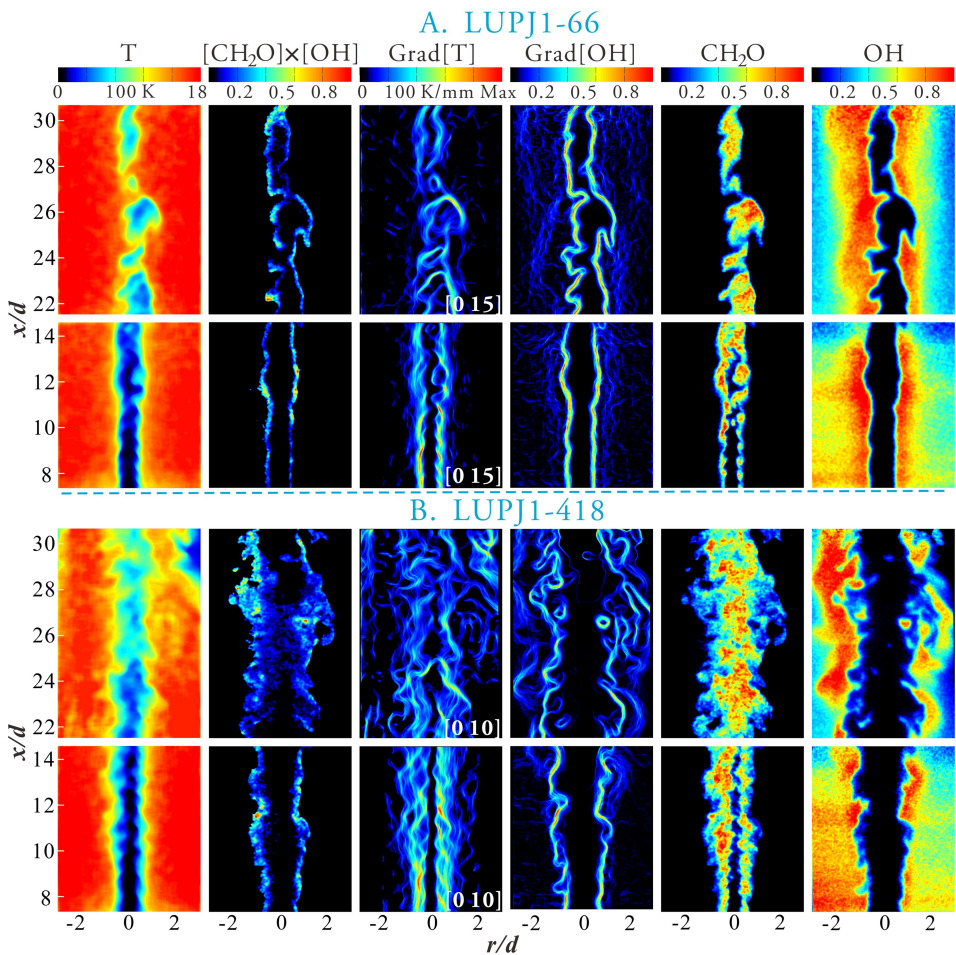


**Figure 5-15** Examples of snapshots of measured scalars and the quantities that were derived (i.e.  $CH_2O \times OH$ ,  $Grad[T]$  and normalized  $Grad[OH]$ ) from the flames LUPJ1-66 and LUPJ1-418 from the  $T/CH_2O/OH$  measurement series

### 5.1.7 Small-scale flame structures

As mentioned in Section 5.1.2, the present multi-scalar imaging system preserves a high spatial resolution of around  $100 \mu m$  for each measured scalar which is slightly coarser but comparable to the Kolmogorov scales for the flames that were investigated (see Table 5-2). In this section, detailed flame structures are illustrated (see Paper VII for further details).

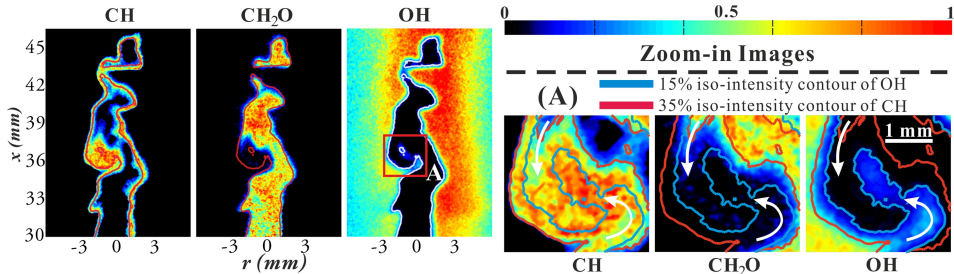


**Figure 5-16** Simultaneous CH/CH<sub>2</sub>O/OH images measured in the flame LUPJ1-110. An iso-intensity contour of OH was superimposed on the fields of other scalars for comparison. Detailed flame structures are further illustrated in the zoom-in image (A) together with the contour of the measured scalars.

Figure 5-16 provides an example of the flame LUPJ1-110 from the CH/CH<sub>2</sub>O/OH dataset. The flame LUPJ1-110 in the TRZ regime can be characterized as a flamelet-like flame from previous discussion. However, non-flamelet behavior was also observed occasionally. In the region marked by the square, the CH layer is seen to be locally broadened up to  $\sim 3$  mm, whereas the CH layer is typically  $\sim 200 \mu\text{m}$  in thickness and lies in the thin OH/CH<sub>2</sub>O interface under the flamelet conditions (see Figure 5-12 (a)). This locally broadened region is further magnified and displayed in Figure 5-16 (A). It can be seen that the iso-intensity contour of the broadened CH layer fits well with both edges of the strong OH and CH<sub>2</sub>O signal regions. As indicated by the arrows, the imaged structure resembles the motion of small eddies that roll in CH<sub>2</sub>O from the unburnt regions and bring in OH from the product side. Such turbulence mixing of reactants and radicals occur rapidly along with chemical reactions including those that generate CH. The mixing process is also reflected on the CH image: on the upper-left of the images in Figure 5-16 (A), following the direction of the arrow, the CH<sub>2</sub>O signal gradually decreases with a corresponding increase of CH signal as CH<sub>2</sub>O is rolling in; a similar observation can also be made for OH if one follows the arrow at the bottom-right of the images in Figure 5-16 (A). This observation might present as an example of a possible onset of local CH-layer thickening as a consequence of local rapid turbulence mixing between unburnt reactants (represented by CH<sub>2</sub>O) and radicals (represented by OH) from the product side. It appears that the eddy-like structures of OH and CH<sub>2</sub>O have a diameter of  $\sim 2$  mm, which is comparably larger than the thickness of the flame front but close to the integral scale in the present flame (see Figure 5-4). This is consistent with the theoretical speculation as depicted by Lipatnikov [25] that “*the thickening of the flamelets starts from small-eddy penetration and then larger and larger*

*eddies could penetrate into thicker and thicker reaction zones and thereby broadening them further and further. Due to such a penetration-broadening-penetration cascade, the reaction zone could finally reach a thickness of the order of the integral length scale.”*

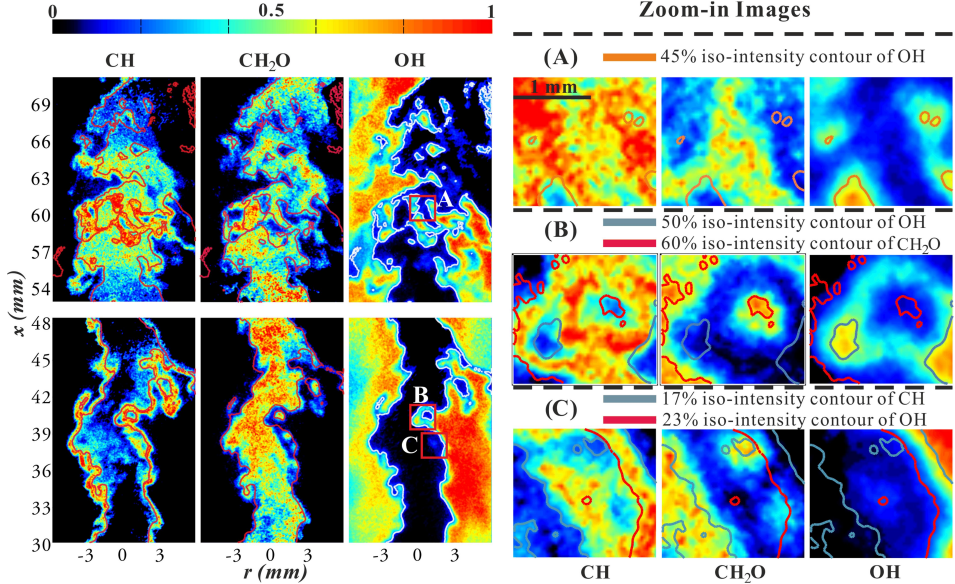


**Figure 5-17** Simultaneous CH/CH<sub>2</sub>O/OH images measured in the flame LUPJ1-418, featuring distributed reactions. The iso-intensity contour of OH was superimposed on the fields of other scalars for comparison. Detailed flame structures are further illustrated in the zoom-in images (A), (B) and (C) together with the contours of scalars that were measured.

The other example is given in Figure 5-17 for the flame LUPJ1-418 which features distributed reactions. Three regions containing local fine structures of the distributed reaction are marked by the squares in the OH images of Figure 5-17 and displayed in Figure 5-17 (A-C). Contours of measured scalars have been used for illustration of their correlations. Unlike flamelet structures, Figure 5-17 shows that CH, OH and CH<sub>2</sub>O can substantially overlap with each other widely in space. As can be seen in Figure 5-17 (A-C), local increases of OH (CH<sub>2</sub>O) signals even at scales as small as 100  $\mu\text{m}$  can be related to corresponding local low-signal regions of CH and CH<sub>2</sub>O (OH). This demonstrates how the multi-scalar imaging approach assists in the discrimination of small-scale structures from noise. It is noteworthy that in the middle of Figure 5-17 (A) and Figure 5-17 (C) where both OH and CH<sub>2</sub>O signal levels are low or medium, the resolved structures of the reactive scalars (e.g. CH and CH<sub>2</sub>O) are chaotic and remain uncorrelated. This

indicates that the chemical reactions involved rather than turbulent mixing become rate-limiting on a small scale when the concentrations of reactive radicals are low. More comprehensive investigations are needed in the future to reveal the role of small-scale turbulence and how it interacts with the flame front.

## 5.2 Lean Premixed Low-swirl Flames

Low-swirl stabilized lean premixed flames (LSFs) bear the advantages of low  $\text{NO}_x$  emission, stable flame operation and low noise, and therefore have the potential to be employed for gas turbine applications [124-127]. The present work (that reported in Paper VIII) concerned two methane/air LSFs, designated as LSF-1 and LSF-2 with Reynolds numbers of 20000 and 50000, respectively, using simultaneous PLIF measurements of  $\text{CH}$ ,  $\text{OH}$  and  $\text{CH}_2\text{O}$ .

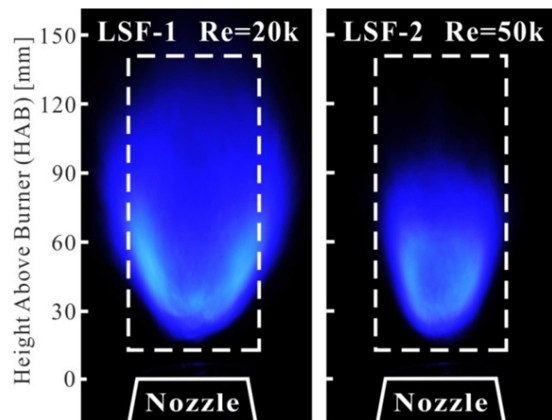


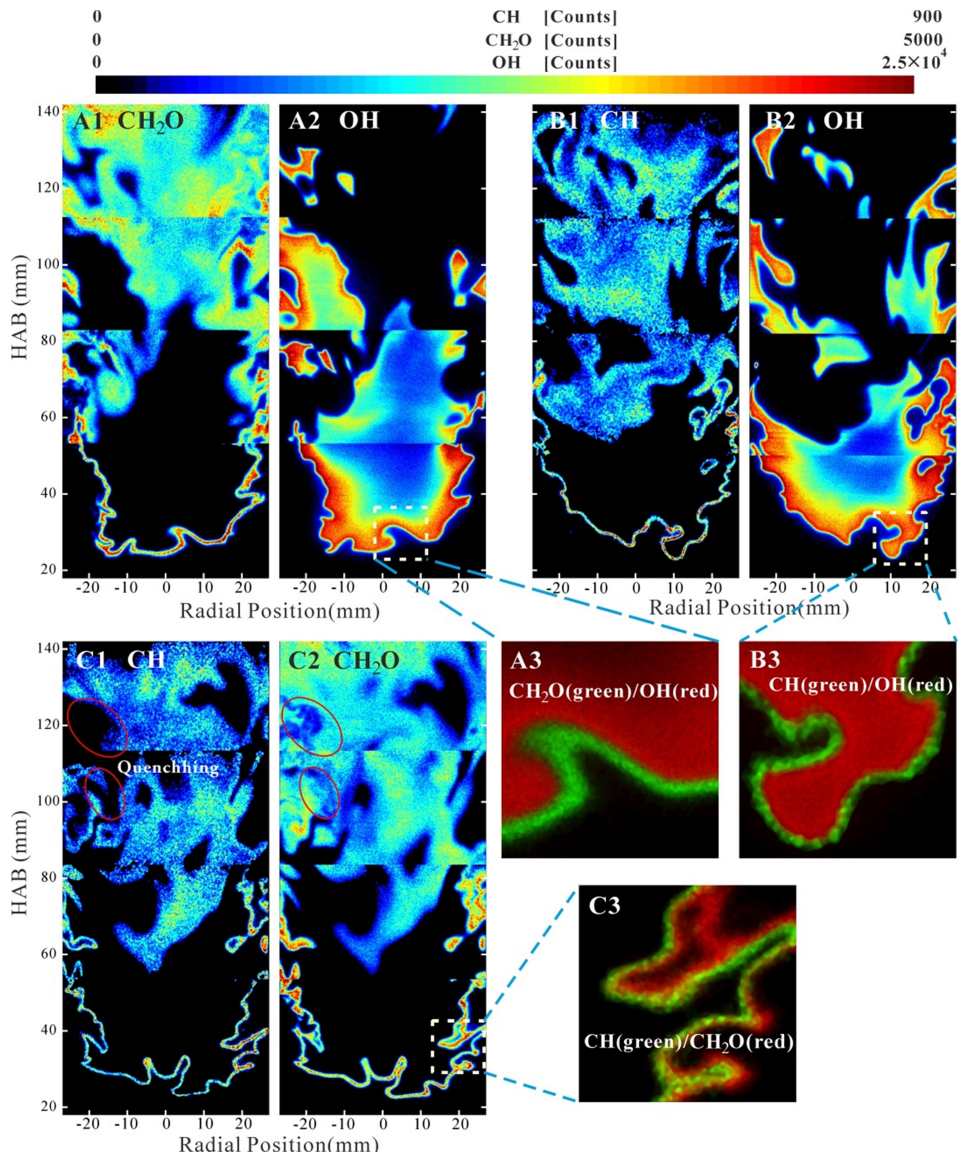
**Figure 5-18** Photographs of investigated flames, LSF-1 and LSF-2 with 200 ms exposure time. The dashed squares indicate the area that has been investigated by PLIF measurements.

Direct photographs of LSF-1 and LSF-2 are shown in Figure 5-18. The two flames exhibit a rather similar lift-off distance of  $\sim 30$  mm above the burner exit, whereas LSF-2 shows a significantly smaller flame chemiluminescence volume than that of LSF-1, a matter that can be explained by the increased ambient air entrainment downstream of the flame [128]. The region in which the PLIF measurements were performed is marked out by the dashed squares in Figure 5-18, which cover the leading flame front region (LFF, at height above burner, HAB of  $\sim 30$  mm), the flame trailing edge region (FTE,  $\sim 30$  mm  $<$  HAB  $<$  55 mm) and the central region of the flame further downstream (HAB  $>$  55 mm). Most of the

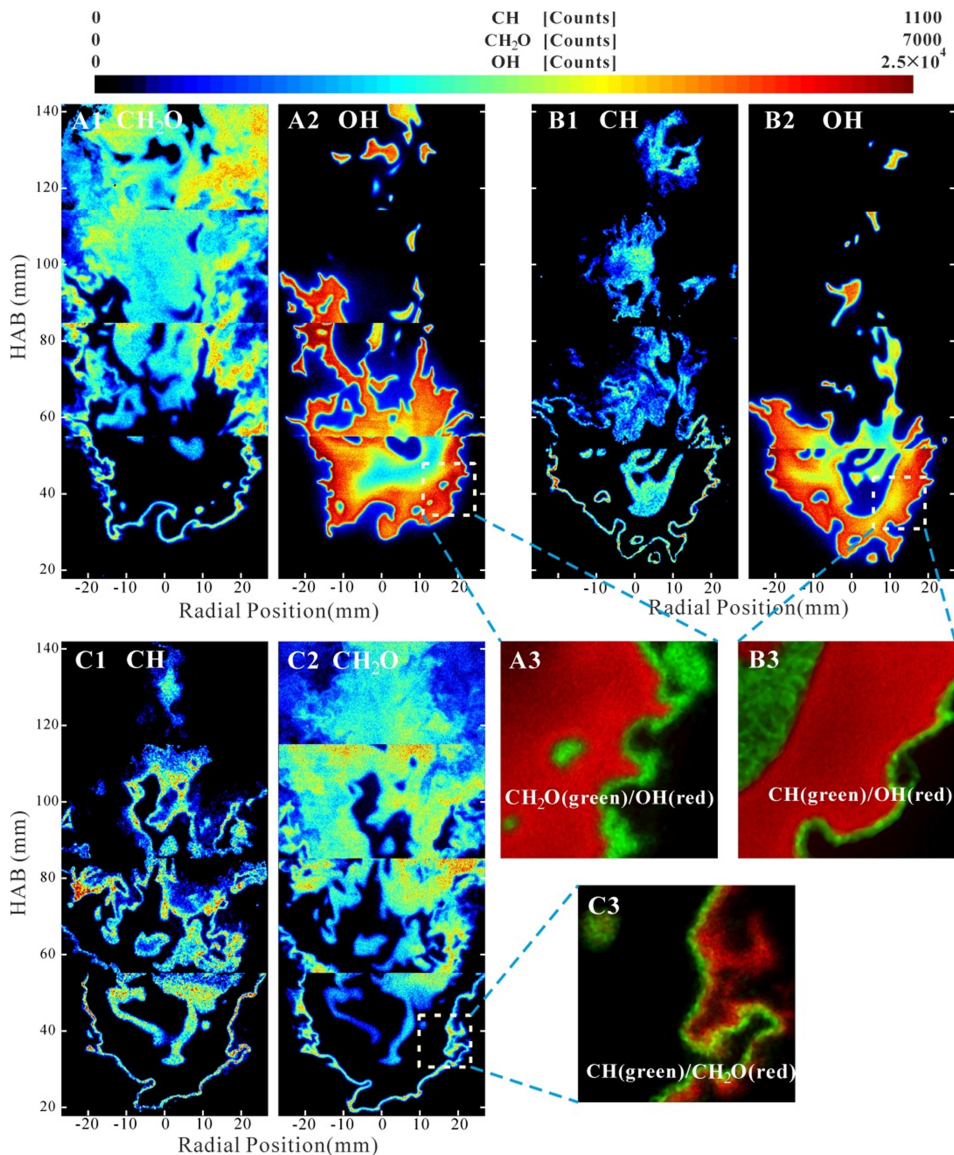
experimental and numerical investigations have been focused on the LFF region where the LFF has been shown to be thin and of typical laminar flamelet structure [10, 29, 129-133]. Slightly downstream, the existence of extinction holes in the FTE region due to the ambient air entrainment has been reported [12, 134, 135]. On the basis of the flow field measurements under similar flame conditions [9, 134], the Karlovitz number of the investigated flames is estimated to be about unity at the LFF region and about 30 in the FTE region, their thus being located in the corrugated/TRZ regimes in the Borghi diagram. The fuel/air mixture diluted by the entrained ambient air can leak through the holes into the downstream regions and mix with the hot combustion products. The characteristics of the leaked unburned fuel/air mixture downstream are not adequately studied by experiments. This is re-examined in the present work.

Figure 5-19 shows examples of three series of simultaneous PLIF images for LSF-1: (A)  $\text{CH}_2\text{O}/\text{OH}$ , (B)  $\text{CH}/\text{OH}$  and (C)  $\text{CH}/\text{CH}_2\text{O}$ . Each image consists of four independent instantaneous PLIF image pairs recorded at different HAB positions. As can be seen in Figure 5-19 (A1-A2), the LFF of LSF-1 contains a thin  $\text{CH}_2\text{O}$  layer that partially overlaps with the high-gradient OH front, exhibiting a typical laminar flamelet structure. OH radicals prevail over a large area downstream of the LFF, signifying a region with hot combustion products where the mean temperature up to 1700 K has been measured [136]. In the downstream regions ( $\text{HAB} > 55$  mm) where fuel was found to widely exist [135], intermediate reactant,  $\text{CH}_2\text{O}$  appeared distributed in space with reduced maximum signal level by a factor of 2 as compared with the LFF region. This indicates that the leaked fuel in the downstream regions can continue to react. The corresponding mean temperature (reported in Ref. [136]) along the central axial direction decreases gradually from 1600 K (at  $\text{HAB}=55$  mm) to 1000 K (at  $\text{HAB}=140$  mm) due to the entrainment of ambient air. More strikingly, Figure 5-19 (B-C) shows that the short-lived CH radicals can be distributed and coexists with  $\text{CH}_2\text{O}$  in wide regions downstream, similar to the observed distributed reactions in the LUPJ flames but with completely different burner configuration. Furthermore, at some downstream locations as marked by the circles in Figure 5-19 (C1-C2), the CH signal disappears whereas  $\text{CH}_2\text{O}$  still survives, which very likely signifies local quenching of the distributed reactions due to cooling of the entrained ambient air. In contrast to the distributed reactions downstream, the CH layer in the LFF/FTE regions is thin. As further shown in Figure 5-19 (A3-C3), the CH layer is shown to locate downstream of the  $\text{CH}_2\text{O}$  layer and upstream of the OH layer, coinciding with the layer in which OH and  $\text{CH}_2\text{O}$  partially overlap. It is noteworthy in Figure 5-19 (C3) that the CH layer in the FTE region remains thin and intact, whereas the

$\text{CH}_2\text{O}$  layer is distorted by small turbulence eddies, which can be considered as a typical flame front structure in the TRZ regime.



**Figure 5-19** Examples of simultaneous PLIF measurements of (A1-A2)  $\text{CH}_2\text{O}/\text{OH}$  (B1-B2)  $\text{CH}/\text{OH}$  and (C1-C2)  $\text{CH}/\text{CH}_2\text{O}$  for LSF-1 ( $\text{Re}=20000$ ). The local structures of two simultaneously measured species as marked by the dashed square are shown in (A3-C3)



**Figure 5-20** Examples of simultaneous PLIF measurements of (A1-A2)  $\text{CH}_2\text{O}/\text{OH}$  (B1-B2)  $\text{CH}/\text{OH}$  and (C1-C2)  $\text{CH}/\text{CH}_2\text{O}$  for LSF-2 ( $Re=50000$ ). The local structures of two simultaneously measured species as marked by the dashed square are shown in (A3-C3)

Simultaneous PLIF measurements of LSF-2 are shown in Figure 5-20. Similar to LSF-1, the flamelet-like structures of LSF-2 (cf. Figure 5-20 (A3-C3)) in the LFF/FTE regions and the distributed reactions in the downstream regions are also

found, whereas LSF-2 displays more wrinkled structures in the LFF/FTE regions owing to the smaller scales of the turbulent eddies in higher Reynolds number flame. It appears that the distributed reactions start earlier in space with increased the Reynolds number as indicated by the occurrence of a distributed CH layer with HAB  $\sim$ 50 mm shown in Figure 5-20 (B1-C1). Furthermore, quenching of the distributed reactions (indicated by the absence of the distributed CH regions) were not observed within the region with HAB  $<$  50 mm where the distributed reactions are well surrounded by hot combustion products and are less affected by the ambient air entrainment. In contrast, significant quenching of the distributed reactions can be found at locations downstream (HAB $>$ 60 mm), a matter which is less obvious for the LSF-1 case. This can likely be attributed to the excessive cooling of the ambient air entrainment at the current higher Reynolds number case. As shown in a recent numerical simulation [128], the temperature in the downstream regions of the flame LSF-2 can be significantly lower than 1000 K, whereas the mean temperature for the flame LSF-1 in the same regions is constantly higher than 1000K [136]. Consistent with the finding of distributed reactions in the LUPJ flames [137], the present study supports that the distributed reactions occur above certain temperature, which, in the present cases, is about 1000 K, whereas below this temperature CH is quenched.

In summary, the present study reveals an interesting feature of LSFs, namely the LSFs are shown to span spatially over many combustion regimes which covers the corrugated flamelet regime in LFF region, the TRZ regime in FTE region and the DRZ regime in the downstream region. This result provides a direct experimental evidence along with the one found in LUPJ flames that distributed reactions can be a common combustion mode.

### 5.3 Concluding Remarks of Distributed Reactions in Turbulent Premixed Flames

Along with the present work, a number of earlier studies have also reported some experimental flame observations which were claimed to concern the distributed reactions. These are summarized in Table 5-4. In addition, an experimental observation of a broadened reaction layer in the interface between two liquids is also included [138]. It can be noted that the present work provides unique and persuasive evidence for the existence of distributed reactions through the direct visualizing of short-lived radicals, namely, HCO and CH. As discussed earlier, the chemical lifetime of HCO and CH is on the order of ten nanoseconds. Therefore,

the presence of HCO/CH must indicate the occurrence of reactions so that the observation of broadened/distributed HCO/CH layers can be regarded as a rigorous criterion for the existence of DRZ in flames. In this section, it is intended to clarify other experimental observations which can be associated with the occurrence of DRZ in flames.

**Table 5-4** Experimental observations of distributed reactions

Case No.	Flames	Methods	Observations	Refs
1	Piloted CH <sub>4</sub> /air jet flames	➤ OH/CH <sub>2</sub> O PLIF ➤ RST <sup>1</sup>	<ul style="list-style-type: none"> <li>• Reduced <math>\nabla T</math> with increased jet speeds. Equivalently, homogeneous T field and broadened thermal thickness</li> <li>• <math>\nabla T</math> fields contain filament-like fine structures</li> <li>• Patchy OH regions</li> <li>• Appearance of quenching-and-ignition judging from flame chemiluminescence</li> </ul>	[108, 123, 139]
2	Fan stirred CH <sub>4</sub> /air flames	➤ MIE <sup>2</sup> ➤ High speed FC <sup>3</sup> ➤ Schlieren imaging	<ul style="list-style-type: none"> <li>• A bending point of MIE appears with increasing turbulent intensity</li> <li>• Flame fronts (judged from high speed FC) appear dispersive and fragmental with filament-like edges</li> </ul>	[140-142]
3	Piloted CH <sub>4</sub> /air jet flames	➤ OH/CH <sub>2</sub> O PLIF	<ul style="list-style-type: none"> <li>• The third point in case 1</li> <li>• OH<math>\times</math>CH<sub>2</sub>O area increases with increasing <math>Re_t</math></li> </ul>	[109]
4	LUPJ and LSB CH <sub>4</sub> /air flames	➤ OH/CH/HCO/CH <sub>2</sub> O PLIF ➤ RST <sup>1</sup>	<ul style="list-style-type: none"> <li>• The first three points in case 1</li> <li>• The point in case 3</li> <li>• Distributed CH and HCO layers</li> <li>• Distributed reactions appear to occur above 1000 K</li> <li>• OH radicals were found in low-T region with low concentration level</li> <li>• CH and HCO appear similar but might have subtle differences in intensity distribution</li> <li>• HCO (CH) radicals can widely coexist with CH<sub>2</sub>O in space even when OH is barely detectable</li> </ul>	Papers V to VIII
5	Reaction in interface of two liquids <sup>4</sup>	LIF of reactants	$S \sim \sqrt{Re_t}$ where S is the ratio of turbulent and laminar propagation rate of reaction front	[138]

<sup>1</sup> Rayleigh Scattering Thermometry; <sup>2</sup> Minimum ignition energy; <sup>3</sup> Flame Chemiluminescence;

<sup>4</sup> Not technically a flame but a reacting interface between two liquid solutions.

For one thing, the present results for both LUPJ flames and LSB flames indicate that temperatures above  $\sim 1000$  K appears to be important for sustaining distributed reactions. This sheds light on the fact that most of the flame conditions (Case 1 and Case 3 in Table 5-4) that were claimed to be in DRZ mode employed a pilot coflow flame. In addition, in the present work the build-up of radical pools in the regions with (intermediate) reactants was found to be responsible for the DRZ. The broadening of the  $\text{CH}_2\text{O} \times \text{OH}$  layer was shown in the present work to be in line with the broadening of HCO/OH (see Section 5.1.6), which could be considered as an additional criterion for DRZ. However, cautions have to be taken in regard to the issues of limited SNRs and the non-ideal background subtraction, which might lead to an artificially broadened or thinning of the  $\text{CH}_2\text{O} \times \text{OH}$  layer as discussed in Section 5.1.6. In addition, it is noteworthy that some of the observations listed in Table 5-4 may not necessarily be associated with the distributed reactions. For instance, the observation of the fine filament-like structures in the  $\text{Grad}[T]$  field is not a unique feature of distributed reactions since the distortion of the temperature field through turbulence starts already for flames in the TRZ regime which can be exemplified in Figure 5-15 for LUPJ1-66. Besides, the patchy OH regions that were observed in the flames might merely signify quenching and not be explicitly linked to DRZ. Finally, no direct evidence has been found that the observations in regard to Case 2 reported by Shy et al. [140-142] belong to the distributed reactions. This remains to be clarified through further investigations (such as CH/HCO PLIF) on the experimental conditions of Case 2.

In addition to the experimental evidence concerning DRZ, some DNS simulations in high  $Ka$  flames have also been reported, these being summarized in Table 5-5. Consistent with the experimental results, the major observation regarding DNS simulation is the transport of radicals to the low temperature regions, leading to an enhancement of local heat release in low-temperature regions and the decorrelation between the fuel consumption and the heat release regions. It is noteworthy that such radical transport might have occurred in the TRZ regime [112], but it is certainly more marked and dominant in the DRZ regime. On the other hand, all of the DNS were performed in turbulent tube flows, and only a broadened but not a distributed reaction zone was reported. This discrepancy may arise from the streamwise history effects in practical combustion which are not considered in DNS. In addition, it can be noted that the Lewis number effect on the high  $Ka$  flames is one that has been of particular interest in the DNS investigations that have been carried out, but that it has not been examined experimentally. Experimental investigations using the techniques involved in the

present work can be carried out to bridge such a mismatch to thus facilitate a better comparison between the experiments and numerical simulations.

**Table 5-5** Numerical observations of distributed reactions

Case No.	Flames	Methods	Observations	Refs
1	H <sub>2</sub> /air, CH <sub>4</sub> /air and C <sub>3</sub> H <sub>8</sub> /air flames embedded in turbulent tube flow	3D DNS	<ul style="list-style-type: none"> <li>● The reaction zone appears thickened but not distributed.</li> <li>● A pool of radicals such as H, O, OH and HO<sub>2</sub> can be found in low-T regions, which are responsible for enhancement of reactions at low-T regions.</li> <li>● Decorrelation between the fuel consumption and heat release regions.</li> <li>● Lewis number, beside Ka, might also influence the transition from flamelet to distributed reaction mode.</li> <li>● Methane and propane flames in the DRZ regime have similar burning rate to their corresponding laminar values, whereas the burning rate for the hydrogen flame was enhanced in the DRZ regime.</li> </ul>	[112, 143- 145]
2	Similar to case 1	2D and 3D DNS	<ul style="list-style-type: none"> <li>● The first two points in case 1.</li> <li>● Rapid convective transport in high Ka flames, which is an order of magnitude faster than the chemical reaction rate, is responsible for effective rapid exchanges among burnt, unburnt and reactive mixtures prior to being consumed.</li> <li>● Methane/air and hydrogen/air flames with the same Ka exhibit differently in the transition from flamelet to distributed reaction mode, which is partially attributed to the differential effects</li> </ul>	[46, 113, 146]

The schematic plot presented in Figure 5-21 attempts to depict the flame front/turbulence interaction in the DRZ regime on the basis of the experimental observations made in the present work. In the DRZ regime, if an established boundary that separates the (intermediate) reactants from the burned mixture is subjected to strong turbulence distortions, the temperature field might be first homogenized (see Figure 5-8 for the experimental examples). The radicals such as H and OH can be transported rapidly to the regions of reactants, giving rise to significant local heat release. Three major exothermic reactions identified as being responsible for such heat release for H<sub>2</sub>/air flames through DNS [112, 113] are listed in Figure 5-21. The concentration of transported OH and H radicals might have to stay low at the region with an appreciable amount of reactants (see Figure 5-17 for experimental evidence). The transport of intermediate reactants such as CH<sub>2</sub>O to the burnt regions was shown to be less effective in the present experiments, which can be probably attributed to the preferential diffusion, the lighter radicals/species being transported faster and further. Therefore, the heat release layer is extended only slightly beyond the original reactant/burnt mixture

interface to the burnt region. It is not clear thus far how the HRR in the distributed reaction mode compares with that in the laminar flamelet case. This issue remains to be investigated in the future. In addition, the concepts such as the flame surface density and the displacement speeds of the flame fronts may no longer be valid under the DRZ regime. Accordingly, revisions of the current flamelet combustion models may be needed in order to adapt the nature of DRZ in an appropriate manner.

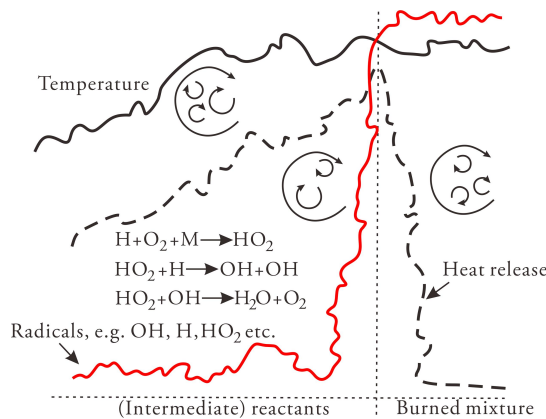


*Figure 5-21 Schematic of the flame front interacting with eddies in the DRZ regime.*

## 5.4 Similarities with Other Combustion Concepts

The concept of the distributed reactions does not apply solely to turbulent premixed combustion in which distributed reactions are achieved through the intensive turbulence/flame front interactions. Instead, a group of similar combustion concepts also utilizes a similar idea of the DRZ which is in contrast to the conventional view of the laminar flamelet-like flames. The moderate or intense low-oxygen dilution (Mild) combustion is probably the most quoted expression among these concepts. Other expressions such as FLOX (Flameless Oxidation), CDC (Colorless Distributed Combustion), HiCOT (High Temperature Combustion Technology) and HITAC (High Temperature Air Combustion) have also been employed and referred to the same or similar combustion processes as the Mild combustion. This type of combustion is typically featured by an elevated temperature of reactants and low temperature increase during the combustion process [111]. The elevated temperature of reactants is achieved either by preheating of air or by hot exhaust gases recirculation (EGR). The invisible flame

chemiluminescence (FC) to the naked eyes and the homogeneous distribution of time-averaged OH<sup>\*</sup> emission are typically regarded as being experimental evidence for the occurrence of distributed reactions [147-151] since the visible FC is associated with the thin flame front under laminar flame conditions [54]. Recent DNS simulations [152] under Mild conditions indicate, however, that the reactions may still occur in thin regions. To study experimentally the reaction zone structures of Mild combustion, flame emission spectra and instantaneous OH PLIF measurements were carried out in a laboratory flameless combustor. CH PLIF measurements in the flameless combustor were also attempted, but very little CH signal were detected under all flame conditions that were investigated.

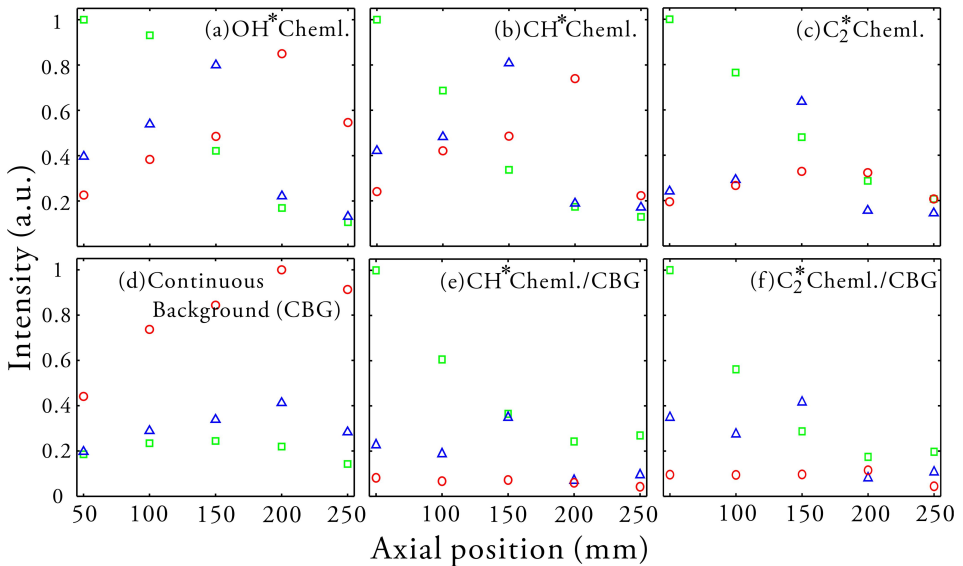


**Figure 5-22** Spectrally integrated intensities of (a) OH<sup>\*</sup>, (b) CH<sup>\*</sup> and (c) C<sub>2</sub><sup>\*</sup> after background subtraction recorded at different axial positions along the flameless combustion chamber for three combustion modes, i.e. the conventional mode (squares), the transient mode (triangles) and the flameless mode (circles). (d) the subtracted continuous background (CBG) was integrated over the visible range (400 nm – 700 nm) and (e-f) the intensities of the CH<sup>\*</sup> or C<sub>2</sub><sup>\*</sup> emission divided by the corresponding CBG. The data points in each subplot are normalized by their corresponding maximum value.

Except for the appearance of a continuous background (CBG), the emission spectra recorded from the flameless combustor were similar to the one showed in Figure 4-1, where the emissions from OH<sup>\*</sup>, CH<sup>\*</sup> and C<sub>2</sub><sup>\*</sup> can be identified. Figure

5-22 (a-c) presents the spectrally-integrated intensities of OH\*, CH\* and C<sub>2</sub>\* after background subtraction as a function of the axial location along the combustion chamber for each of the three combustion modes. As can be seen, the OH\* and CH\* show a similar trend in the axial direction for each combustion mode, their also being qualitatively in line with the OH\* emission images shown in Figure 2-5. The transient and flameless modes show slightly weaker OH\* and CH\* emissions than the conventional mode does. Instead, a significant suppression of the C<sub>2</sub>\* emissions can be observed for the flameless mode (Figure 5-22 (c)). Nevertheless, it is clear from the measured spectra that the visible CH\* and C<sub>2</sub>\* emissions still exist even under the flameless condition in which the flame appears to be invisible to the naked eyes as shown in Figure 2-4. The flame visibility is reduced further through the increased CBG emission likely contributed from the CO<sub>2</sub>\* emission [153]. The intensities of the CBG for each of the three combustion modes were integrated spectrally over the visible spectral range (400nm – 700 nm) and displayed in Figure 5-22 (d). The CH\* and C<sub>2</sub>\* emissions that are responsible for the flame visibility are normalized by their corresponding CBG values as shown in Figure 5-22 (e) and (f), respectively. It can be seen that the CH\*/CBG and C<sub>2</sub>\*/CBG emission intensities are constantly low, both of them being about an order of magnitude lower than the maximum value of the conventional condition. The increased CBG reduces the contrast of the visible flame emission against the background so that flames appear to be invisible to the naked eyes.

**Table 5-6** Formation mechanisms of major chemiluminescent species in flames.

OH* Mech.	Refs	CH* Mech.	Refs
R1 CH+O <sub>2</sub> ↔CO+OH*	[154, 155]	R3 C <sub>2</sub> +OH↔CO <sub>2</sub> +CH*	[156, 157]
R2 H+O+M↔M+OH*	[158]	R4 C <sub>2</sub> H+O <sub>2</sub> ↔CO <sub>2</sub> +CH*	[159]
		R5 C <sub>2</sub> H+O↔CO+CH*	[160]
C <sub>2</sub> * Mech.	Refs	CO <sub>2</sub> * Mech.	Refs
R6 CH <sub>2</sub> +C↔H <sub>2</sub> +C <sub>2</sub> *	[161]	R8 CO+O+M↔CO <sub>2</sub> *+M	[153]
R7 C <sub>3</sub> +O↔CO+C <sub>2</sub> *	[162]		

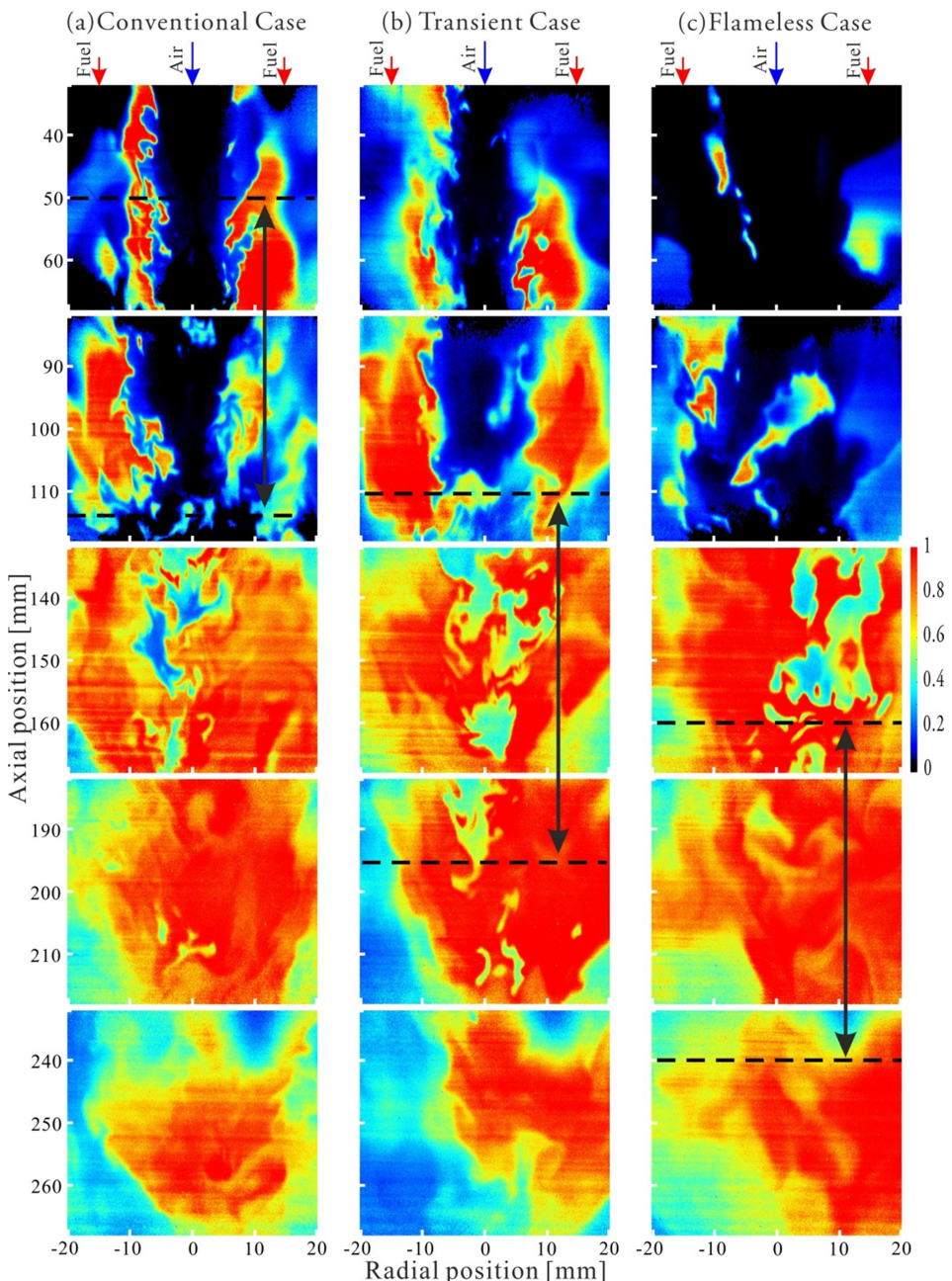


**Figure 5-23** Instantaneous OH PLIF images for (a) the conventional mode (b) the transient mode and (c) the flameless mode. The primary regions of  $\text{OH}^*$  emission shown in Figure 2-5 are delimited by the dashed lines.

The chemical kinetics provides insight into the changes in intensity of these chemiluminescent species. The major formation mechanisms of the chemiluminescent species in flames are listed in Table 5-6. Under the flameless condition, as shown by the reaction R8, the increase of  $\text{CO}_2^*$  emission that was observed suggests an increase in the concentration of CO, which promotes the forward reaction. Thus, peak CO concentrations might be expected along with the peak of  $\text{CO}_2^*$  emission which was shown in Figure 5-22 (a) and (d) to qualitatively coincide in space with the location of peak  $\text{OH}^*$  emission. The increased CO concentration would also result in a reduction in  $\text{C}_2^*$  formation through R7, in  $\text{CH}^*$  formation through R5 and in  $\text{OH}^*$  formation through R1. In laminar hydrocarbon flames, both CO and  $\text{H}_2$  are intermediate reactants and coexist in the oxidation layer. Thus, it might be expected that  $\text{H}_2$  concentration would also increase, which would lead to a further suppression of  $\text{C}_2^*$  formation through R6. On the other hand, the formation channels of R2 for  $\text{OH}^*$ , R3 and R4 for  $\text{CH}^*$  are less affected. This explains the spectral characteristics that were observed under the flameless condition.

Figure 5-23 shows instantaneous OH PLIF images for (a) the convention mode (b) the transient mode and (c) the flameless mode and the primary regions of  $\text{OH}^*$  emission shown in Figure 2-5 are delimited by the dashed lines. Overall, one can note that the edges of the OH layer for all the three flame modes are not as sharp as the one shown in typical flamelet-like flames [163]. Particularly, for the cases of the transient mode and the flameless mode, the minimal OH signal level is appreciably above zero in the region around the axial position of 150 mm, being about 40% of the maximum signal in the same region. This suggests a non-flamelet behavior. Recent numerical simulations under Mild conditions indicate that the non-flamelet behavior could be resulted from the intensive flame-flame interaction in addition to the turbulence/flame interaction [152, 164]. It should be noted that instantaneous OH field has been also shown to contain sharp OH gradients under MILD conditions [165], which is in contrast to the results shown in Figure 5-23. This fact indicates that the features of MILD combustion might vary from one to the other depending on practical experimental configuration. Further classification of different types of MILD combustion could be needed. Of interest too is the fact that under the flameless condition the  $\text{OH}^*$  emission regions correspond to the regions where the instantaneous OH field appeared to be rather homogeneous. In addition, as also shown by A.S. Verissimo et al. [13] for the same flameless combustor with similar flame conditions, the  $\text{OH}^*$  emission on the mean tends to largely overlap with the occurrence of CO in space. Accordingly, the  $\text{OH}^*$  might be used to mark out the CO oxidation regions. The CO oxidation by OH,

for example, takes place at relatively slower reaction rates, which can thus be expected to be more prone to turbulence distortions. In the flameless case, the homogeneous OH distribution in the regions of OH<sup>\*</sup> emissions suggests that CO oxidization might take place in a distributed way. As long as the resident time of CO in the combustion chamber is sufficiently long, CO will be eventually oxidized to CO<sub>2</sub>, resulting in a negligible amount of CO being found in the exhaust gases which is measured to be about 5 ppm under the current flameless condition [13].

In summary, the present spectral investigations show that the invisibility of Mild (or flameless) combustion can be attributed to the suppression of both the C<sub>2</sub><sup>\*</sup> emission and the CH<sup>\*</sup> emission, the latter to a lesser extent, along with an increase in the continuous background from CO<sub>2</sub><sup>\*</sup>. As analysis of chemical kinetics indicated, this suggests an increased amount of CO in the OH<sup>\*</sup> region. The results of the OH PLIF measurements also suggest the instantaneous OH field appears to be homogeneous in the OH<sup>\*</sup> regions, which points to a distributed CO (and likely H<sub>2</sub>) oxidation process taking place under Mild conditions. Further investigation is needed to determine how fuels are converted into CO under Mild conditions.

# Chapter 6

## Summary and Outlook

The thesis deals with the development and application of laser-based scalar visualization to the study of turbulent premixed combustion.

The first part of the thesis was concerned with the development of laser-based diagnostics intended to provide instantaneous visualization of the key species involved in combustion of hydrocarbons and nitrogen-containing fuels under turbulent conditions. The species in question include HCO and hot O<sub>2</sub> for hydrocarbon flames, together with NH<sub>3</sub>, NH<sub>2</sub> (taken up in related work), and NH for flames burning nitrogen-containing fuels, as well as CN to mark the interplay between the hydrocarbon and nitrogen chemistry. All these above species are demonstrated with good SNRs and the capability of instantaneous visualization using PLIF. In addition, quantification of the CH<sub>2</sub>O PLIF signal is presented, which accounts for the temperature dependence of the Boltzmann factor and of the quenching rate. Besides, the potential for instantaneous temperature mapping by means of two-line atomic LIF (TLIF) of indium using a novel seeding system are demonstrated. It was found to be possible to effectively convert the seeded gaseous Trimethylindium (TMI) into indium atoms without appreciably affecting the flame chemistry.

The second part of the thesis includes the experimental investigations of premixed CH<sub>4</sub>/air turbulent flames on two quite different types of burners, i.e. the LUPJ burner and the LSB burner. The LUPJ and LSB the flames were studied in a wide variety of combustion regimes. Simultaneous visualization of scalars among HCO, CH, CH<sub>2</sub>O, OH and temperature was employed to study the flame structures. The results obtained for both the LUPJ and the LSB flames provided the first experimental evidence that the reaction zone of premixed flames can be significantly broadened through rapid turbulence mixing, a fact being verified by the observation of the broadened and distributed short-lived radicals, HCO and/or CH. The LUPJ flames in which distributed reactions were involved are

characterized by high Karlovitz number. In contrast, the LSB flames typically featured a low Karlovitz number about unity at the leading flame front. The distributed reactions were observed at downstream locations where leaked fuel/air mixture diluted by the entrained ambient air was mixed with hot combustion products from upstream. The Karlovitz numbers downstream of the LSB flames are expected to be high due to the ambient air entrainment. The observations obtained for the two distinctly differing burner configurations suggested that the distributed reactions could be a common combustion mode. In addition, correlations between scalars and the detailed local structures in flames with and without the presence of distributed reactions were analyzed and compared. It was found that the temperature above  $\sim 1000$  K is important for sustaining the distributed reactions involved. The build-up of radical pools through rapid transport of turbulence within the regions of (intermediate) reactants was found also to be responsible for the occurrence of the distributed reactions. The transport of (intermediate) reactants to the burnt regions may be less effective likely due to the preferential diffusion. At last, optical investigations were performed on a flameless combustor which was operated under Mild combustion which has a similar concept of the distributed reactions. The results show that the invisibility of Mild combustion is attributable to the suppression of  $C_2^*$  emission and  $CH^*$  emission, the latter to a lesser extent, together with an increase in the continuous background from  $CO_2^*$ . Under Mild combustion the instantaneous OH fields was found to experience no appreciable gradient in the regions where  $OH^*$  was presented. Chemical kinetics analysis of the formation of these emitting radicals suggested an increased amount of CO presented in the  $OH^*$  regions under the Mild combustion. The  $OH^*$  regions were further shown to have a homogeneous distribution of the instantaneous OH field. This fact suggested the oxidization of CO may take place in a distributed manner. Further investigation is needed in order to obtain an adequate understanding of how the fuels are converted into CO (and likely into  $H_2$  as well) under the Mild combustion.

The DRZ combustion regime is a relatively unexplored area, and the flame behaviors are essentially different from those in the flamelet regimes. Researches to be carried out in the future will aim at obtaining a better understanding of the details of the conditions under which the distributed reactions can be initiated. This could involve studies of the impact of the non-unity Lewis number effect, the dilation effect and the streamwise history effect in practical combustors on the distributed reactions. Examination of the distributed reactions in turbulent flames under elevated pressures could also be of interest. The present work aimed at revealing the structures of the DRZ with multiple scalars being visualized

simultaneously. The temporal evolvement of DRZ structures appears, however, to not have been investigated. An ongoing study of this issue using a high-speed laser system in our laboratory would hopefully glean some additional insights into the turbulence/chemistry interactions in the DRZ regime. At the same time, the concepts of the flame surface density and the displacement speed of flame front etc. derived on the basis of the flamelet theory might need to be reexamined. New or revised conceptions may well need to be introduced in order to enable experimental quantifications of the distributed reactions. For example, an intuitive question that is related would be that of how rapidly combustion proceeds under the DRZ mode.

To study turbulence/chemistry interactions, NH<sub>3</sub>/air flames might be a better candidate than CH<sub>4</sub>/air flames are. As declared in Section 4.2.5, the significantly lower laminar flame speeds of NH<sub>3</sub>/air flames provide the possibility of achieving high  $K\alpha$  flames with much less turbulence levels, a possibility may place experiments to be conducted under a simpler and better-controlled configuration. Also, NH<sub>3</sub> chemistry generally involves fewer species than CH<sub>4</sub> chemistry does which could be a plus. Last but not least, the laser diagnostics developed in the present work allows for the detection of the nitrogen-bonded species which covers the major fuel-oxidization path from the fuel (NH<sub>3</sub>), to the intermediate reactants (NH<sub>2</sub>) and to the reaction zone (NH). This, however, might not be the case for CH<sub>4</sub>/air flames.

On the basis of the experimental data from the present work and those to be acquired in the future (e.g. the high-speed data concerning LUPJ flames), it has been planned to establish an experimental database for LUPJ flames and LSB flames, which would hopefully take account of the characteristics of flow fields, compositional fields and temperature fields. I hope that such a database could evoke collective efforts enabling DNS and experimental measurements from other research groups worldwide to contribute to it. Standardized definitions of turbulent quantities also need to be adopted in order to facilitate comparisons between experiments and numerical simulations.



# Acknowledgements

The work reported in the thesis was carried out at the Division of Combustion Physics, Lund University from the year 2011 to 2014. It has been a fantastic period full of exploring, stimulating experiences, all of which turn out to be a gain in happiness. Time flies as it does when you are enjoying it. I find it somewhat surprisingly that Lund has been the city I have stayed in the longest of any except for my hometown. I have been seeing so many friends of mine come and leave. Now it is about my time to say goodbye to everyone here and to the peaceful and lovely city, Lund. I deeply cherish the past and the time we have been spent together. Memories may fade with time after all, yet one gets to sense the most adorable parts of the past.

I would like to thank Prof. *Macus Aldén* for giving me the opportunity to work here and for your supervision. I could imagine how difficult it must be to build such a large research group and get it running. But your insightful and strategic mind keeps it thriving. I also truly appreciate all of your kind tips and of the help you have given me.

My special appreciations should be given to *Zhongshan Li*. We have spent countless hours discussing various topics. Thank you for being so open and supportive to my ideas and my disagreements at times, and for supporting me to do things that I am most interested in and self-motivated toward. I have also been given the chance of involving in other projects and cooperating with others, which do extend my research perspectives. Alongside work, we have a joint interest in badminton. I have been inspired by your spirit to stick out until the last point even though the odds did not seem to be in our favor.

I want also to express my particular gratitude to Prof. *Xue-song Bai* who has infinite patient and guided me through the field of turbulent combustion. Thanks for your generosity with your time in answering my, I am sure sometimes, dreary questions. I'm sure you may well have been spent more time with me than your own students. I hope your efforts have not been in vain.

*Jesper Borggren* has been my great officemate during the past three years. Thanks for always helping me out with Swedish language. It has been my great pleasure to share the office with you. I wish you all the best in the future.

*Christian Brackmann* is the one who I spent numerous hours with in the lab and deserves my special thanks. You have an organized way of keeping things continuously moving on. You are patient and careful. I cannot imagine how things would have gone in the lab without the precious help from you. My thanks also go to others who I have worked with and who have helped me out in the lab. These include Prof. *Johannes Kiefer* from Germany, Prof. *Mario Costa* from Portugal and many within the Division, including *Ronald Whiddon*, *Jesper Borggren*, *Johan Zetterberg*, *Per Petersson*, *Andreas Ehn* and *Vladimir Alekseev*. In addition, I cannot forget the tough but enjoyable days and nights I have spent working with *Qing Li* and *ZhenKan Wang* for the LDA measurements. Thanks to Prof. *Per-Erik Bengtsson* for his nice course on fundamental combustion. Thanks to Prof. *Alexander Konnov* too for sharing your knowledge of combustion chemistry.

A successful experiment cannot be done without equipment. I truly admire the spirit of sharing equipment in our division. Although it can take time to gather all equipment for a measurement, one's ideas should never be limited by the equipment available. Thus, I would like to thank all my coworkers who shared or borrowed equipment with/to me. I would like in particular to mention in this respect *Kajsa Larsson*, *Andreas Lantz*, *Emil Nordström*, *Fahed Abou Nada*, *Edouard Berrocal*, *Arman Ahamed Subash*, *Vladimir Alekseev*, *Jesper Borggren*, *Malin Jonsson*, *Jinlong Gao* and *Anna-Lena Sahlberg*.

I am also willing to express my gratitude to *Rutger Lorensson* and *Igor Buzuk* for their assistants in solving various mechanical and electronic problems in the lab. My gratitude should also be given to *Minna Ramkull* and *Cecilia Bille* who have helped me dealing with numerous paper works of all kinds during these years. I also want to thank *Eva Persson* who kindly took care of the paper works associated with my PhD registration.

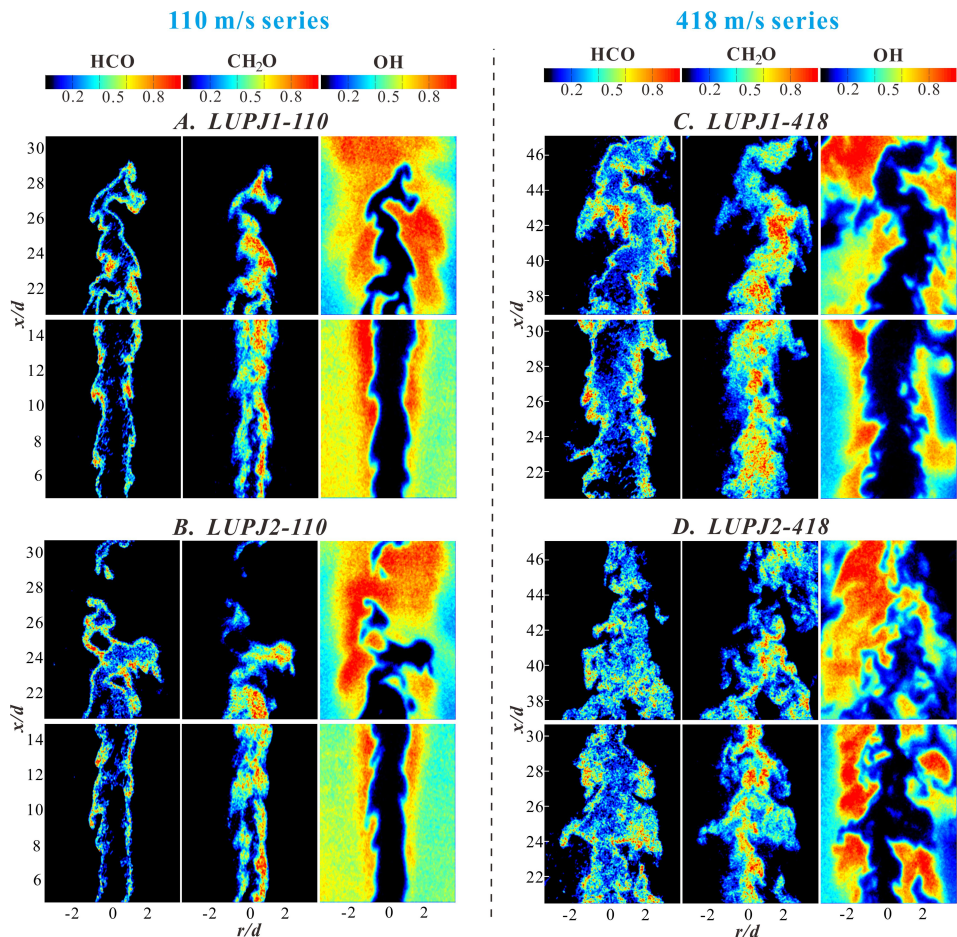
Going back to the beginning of my PhD life or even to the period of my Master diploma work, I would like to thank Prof. *Zhihua Wang* from Zhejiang University for his precious help and advice. I have also received help from *Bo Li* and *Zhiwei Sun*, and *Bo Li* has shared the valuable knowledge of lab experience with me. Thanks to *Yong He*, *Xu Shen* and *Chaoqi Xu* for sharing the great memories of the early years that we have had great fun together. It was one of my most wonderful trips with *Yong He* to the Eastern Europe. Later on, *Ye Zhang*, *Shufang Wei*, *Jiajian Zhu*, *Mengqin Shen* and *Zheming Li* have brought in a lot of

hours of happiness together on Friday nights playing games and showing “the lowest limit”. Thanks to other friends of mine, *Mingchao Wu*, your wife *Yuan Zhou*, *Fan Zhang*, *Jiangfei Yu*, *Xinming Wei*, your wife *Yajing Wu*, *Siyuan Hu*, *Wubin Wen* and *Rixin Yu* as well as those in the Badminton Club and those whose names are not indicated here for the every wonderful moment we have had together.

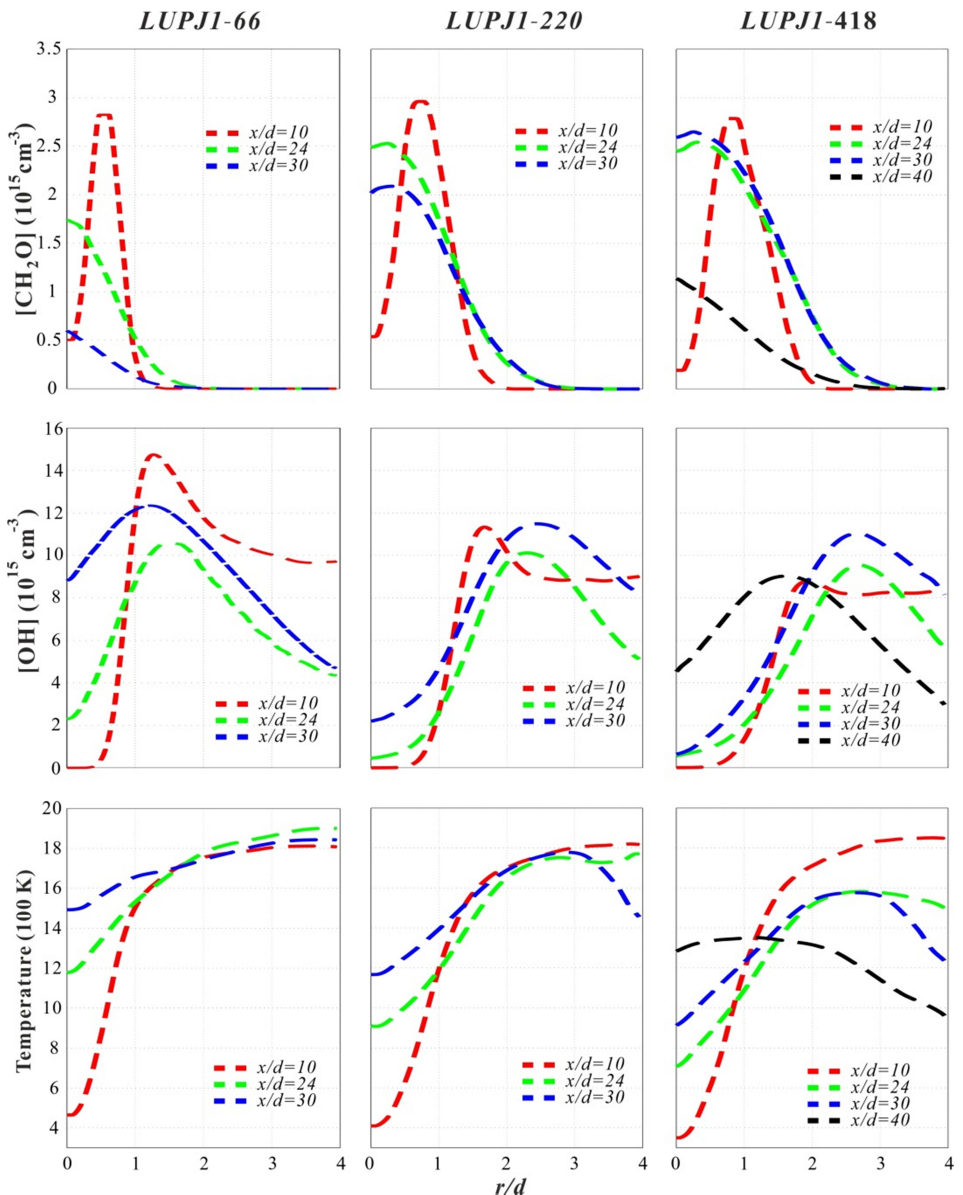
Last but not least I would like to give my deepest gratitude to my family, my parents and my grandparents. You have been my eternal force helping me to carry on. Without your supports and love, I would have never gone so far alone. I dedicate this thesis to my parents and grandparents in particular. I wish a peaceful and healthy life for all of you, and wish I could have more time to stay by your side.



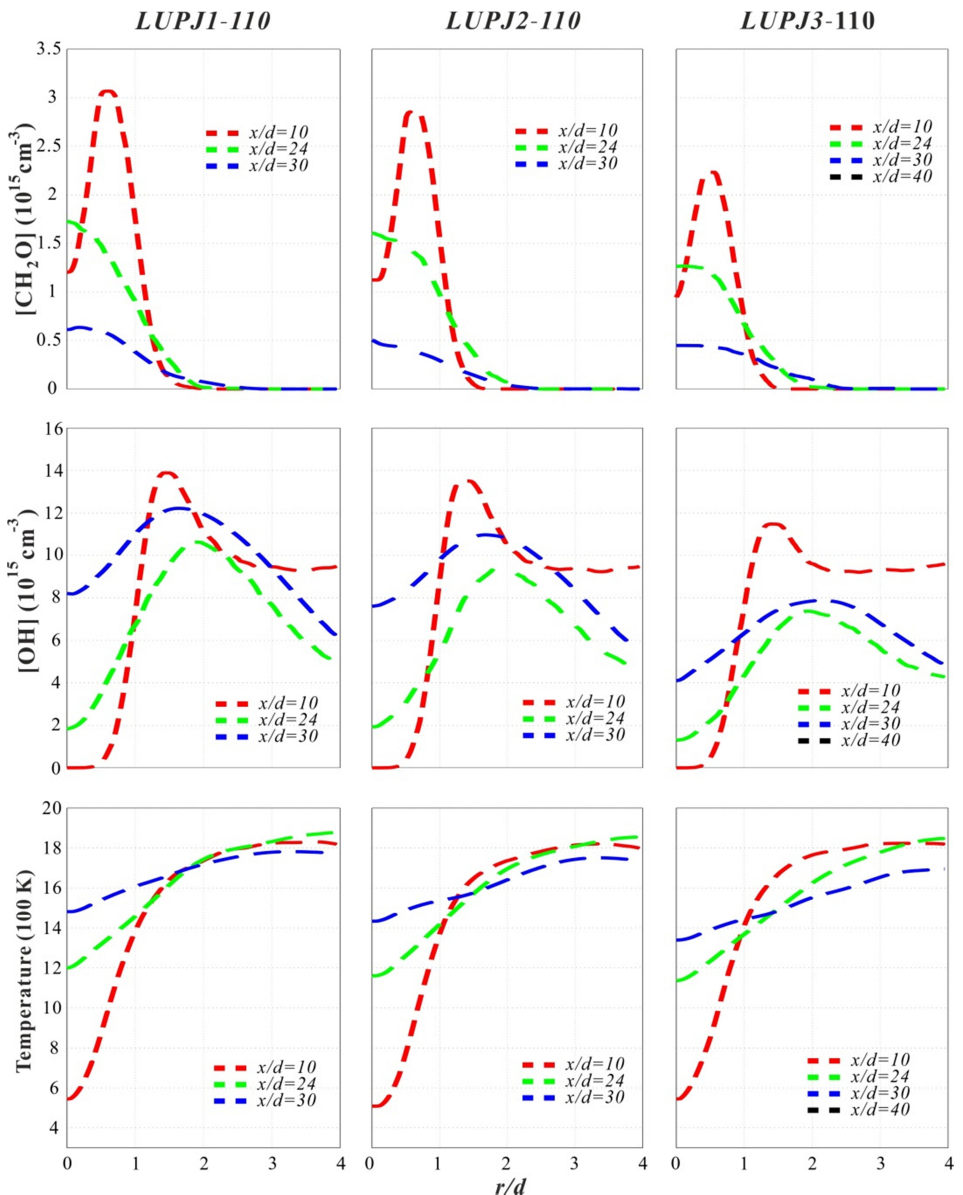
# Appendix



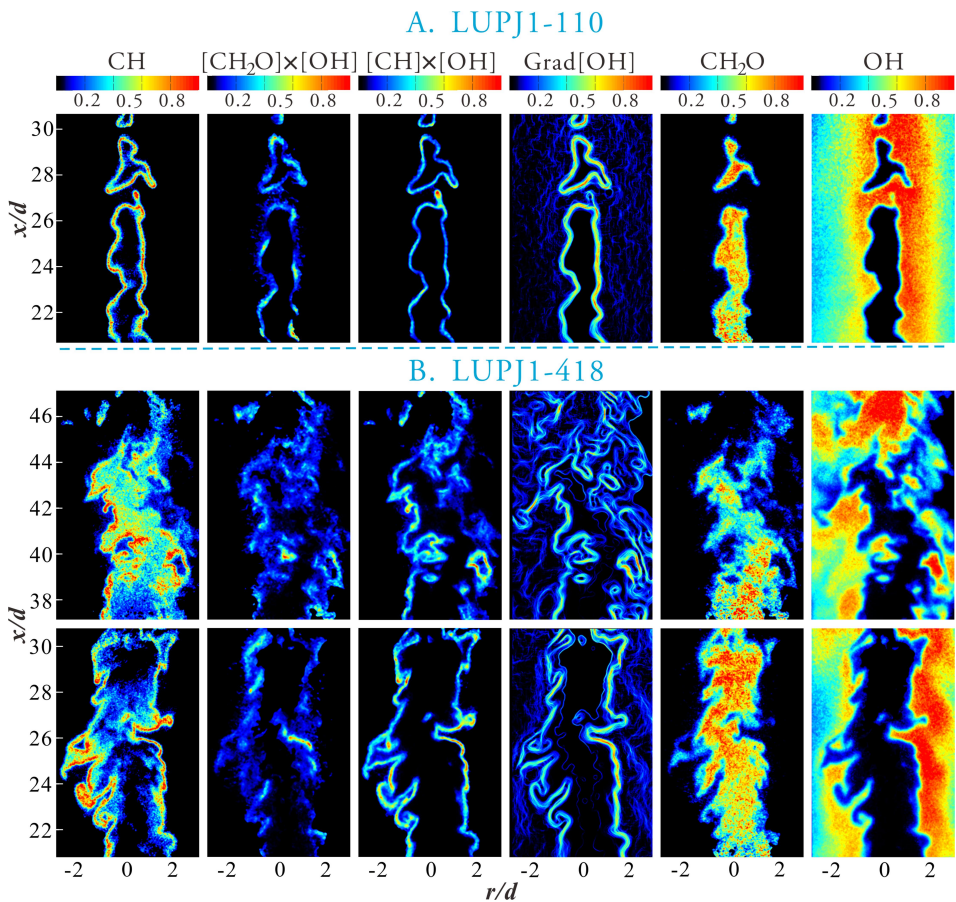
**Appendix I** Examples of equivalence ratio dependence for two given jet speeds, 100 m/s (left) and 418 m/s (right) from the HCO/ $\text{CH}_2\text{O}/\text{OH}$  series.



**Appendix II** Jet speed dependence of mean radial profiles of  $\text{CH}_2\text{O}$  (Row 1),  $\text{OH}$  (Row 2) and temperature (Row 3) at different axial locations for the flames of LUPJ1-66 (Column 1), LUPJ1-220 (Column 2) and LUPJ1-418 (Column 3).



**Appendix III** Equivalence ratio dependence of mean radial profiles of  $\text{CH}_2\text{O}$  (Row 1),  $\text{OH}$  (Row 2) and temperature (Row 3) at different axial locations for the flames of  $LUPJ1-110$  (Column 1),  $LUPJ2-110$  (Column 2) and  $LUPJ3-110$  (Column 3).



*Appendix IV Examples of snap-shots of measured scalars and the quantities that were derived (i.e.  $\text{CH}_2\text{O} \times \text{OH}$ ,  $\text{CH} \times \text{OH}$  and normalized  $\text{Grad}[\text{OH}]$ ) from the flames LUPJ1-110 and LUPJ1-418 from  $\text{CH}/\text{CH}_2\text{O}/\text{OH}$  measurement series*

# References

- [1] T. Megarry, *Society in Prehistory: The Origins of Human Culture*, Mac millan Press, 1995.
- [2] Key World Energy Statistics, IEA, 2014.
- [3] N. Peters, *Multiscale combustion and turbulence*, Proc. Combust. Inst., 32 (2009) 1-25.
- [4] S. Guch, C.E. Jones, *Alexandrite-Laser Performance at High-Temperature*, Optics Letters, 7 (1982) 608-610.
- [5] J.C. Walling, D.F. Heller, H. Samelson, D.J. Harter, J.A. Pete, R.C. Morris, *Tunable Alexandrite Lasers: Development and Performance*, Ieee Journal of Quantum Electronics, QE-21 (1985).
- [6] J. Zetterberg, Z.S. Li, M. Afzelius, M. Alden, *Two-dimensional temperature measurements in flames using filtered Rayleigh scattering at 254 nm*, Applied Spectroscopy, 62 (2008) 778-783.
- [7] V. Wulfmeyer, J. Bosenberg, *Single-mode operation of an injection-seeded alexandrite ring laser for application in water-vapor and temperature differential absorption lidar*, Optics Letters, 21 (1996) 1150-1152.
- [8] PI-MAX Datasheets and Application Notes, Princeton Instruments, 2014.
- [9] M. Day, S. Tachibana, J. Bell, M. Lijewski, V. Beckner, R.K. Cheng, *A combined computational and experimental characterization of lean premixed turbulent low swirl laboratory flames I. Methane flames*, Combust. Flame, 159 (2012) 275-290.
- [10] B. Bedat, R.K. Cheng, *Experimental-Study of Premixed Flames in Intense Isotropic Turbulence*, Combust. Flame, 100 (1995) 485-494.
- [11] R.K. Cheng, *Velocity and Scalar Characteristics of Premixed Turbulent Flames Stabilized by Weak Swirl*, Combust. Flame, 101 (1995) 1-14.
- [12] P. Petersson, J. Olofsson, C. Brackman, H. Seyfried, J. Zetterberg, M. Richter, M. Alden, M.A. Linne, R.K. Cheng, A. Nauert, D. Geyer, A. Dreizler, *Simultaneous PIV/PH-PLIF, Rayleigh thermometry/OH-PLIF and stereo PIV measurements in a low-swirl-flame*, Applied Optics, 46 (2007) 3928-3936.
- [13] A.S. Verissimo, A.M.A. Rocha, M. Costa, *Operational, Combustion, and Emission Characteristics of a Small-Scale Combustor*, Energy & Fuels, 25 (2011) 2469-2480.

- [14] J.O. Hinze, *Turbulence*, McGraw-Hill, New York, 1959.
- [15] K. Seshadri, N. Peters, *The inner structure of Methane-air flames*, Combust. Flame, 81 (1990) 96-118.
- [16] P.H. Paul, H.N. Najm, *Planar laser-induced fluorescence imaging of flame heat release rate*, Proc. Combust. Inst., 27 (1998) 43-50.
- [17] L.P.H. Degoey, A. Vanmaaren, R.M. Quax, *Stabilization of Adiabatic Premixed Laminar Flames on a Flat Flame Burner*, Combust. Sci. Technol., 92 (1993) 201-207.
- [18] C.J. Rallis, A.M. Garforth, *The Determination of Laminar Burning Velocity*, Prog. Energy Combust. Sci., 6 (1980) 303-329.
- [19] N. Chakraborty, M. Katragadda, R.S. Cant, *Effects of Lewis number on turbulent kinetic energy transport in premixed flames*, Physics of Fluids, 23 (2011).
- [20] R. Borghi, *Turbulent Combustion Modeling*, Prog. Energy Combust. Sci., 14 (1988) 245-292.
- [21] N. Peters, *Turbulent Combustion*, Cambridge University Press, Cambridge, 2000.
- [22] C.K. Law, C.J. Sung, *Structure, aerodynamics, and geometry of premixed flamelets*, Prog. Energy Combust. Sci., 26 (2000) 459-505.
- [23] F.A. Williams, *Progress in knowledge of flamelet structure and extinction*, Prog. Energy Combust. Sci., 26 (2000) 657-682.
- [24] D. Veynante, L. Vervisch, *Turbulent combustion modeling*, Prog. Energy Combust. Sci., 28 (2002) 193-266.
- [25] A. Lipatnikov, *Fundamentals of Premixed Turbulent Combustion*, CRC Press, 2012.
- [26] C. Kortschik, T. Plessing, N. Peters, *Laser optical investigation of turbulent transport of temperature ahead of the preheat zone in a premixed flame*, Combust. Flame, 136 (2004) 43-50.
- [27] B. Bohm, J.H. Frank, A. Dreizler, *Temperature and mixing field measurements in stratified lean premixed turbulent flames*, Proc. Combust. Inst., 33 (2011) 1583-1590.
- [28] I.B. Ozdemir, N. Peters, *Characteristics of the reaction zone in a combustor operating at mild combustion*, Experiments in Fluids, 30 (2001) 683-695.
- [29] I.G. Shepherd, R.K. Cheng, T. Plessing, C. Kortschik, N. Peters, *Premixed flame front structure in intense turbulence*, Proc. Combust. Inst., 29 (2002) 1833-1840.
- [30] L.P.H. de Goey, T. Plessing, R.T.E. Hermanns, N. Peters, *Analysis of the flame thickness of turbulent flamelets in the thin reaction zones regime*, Proc. Combust. Inst., 30 (2005) 859-866.

- [31] Z.S. Li, B. Li, Z.W. Sun, X.S. Bai, M. Alden, *Turbulence and combustion interaction: High resolution local flame front structure visualization using simultaneous single-shot PLIF imaging of CH, OH, and CH<sub>2</sub>O in a piloted premixed jet flame*, Combust. Flame, 157 (2010) 1087-1096.
- [32] K. Yamamoto, S. Isii, M. Ohnishi, *Local flame structure and turbulent burning velocity by joint PLIF imaging*, Proc. Combust. Inst., 33 (2011) 1285-1292.
- [33] D. Veynante, J.M. Duclos, J. Piana, *Experimental analysis of flamelet models for premixed turbulent combustion*, Proc. Combust. Inst., 25 (1994).
- [34] C. Meneveau, T. Poinsot, *Stretching and Quenching of Flamelets in Premixed Turbulent Combustion*, Combust. Flame, 86 (1991) 311-332.
- [35] J.A. van Oijen, G.R.A. Groot, R.J.M. Bastiaans, L.P.H. de Goey, *A flamelet analysis of the burning velocity of premixed turbulent expanding flames*, Proc. Combust. Inst., 30 (2005) 657-664.
- [36] R. Sankaran, E.R. Hawkes, J.H. Chen, T.F. Lu, C.K. Law, *Structure of a spatially developing turbulent lean methane-air Bunsen flame*, Proc. Combust. Inst., 31 (2007) 1291-1298.
- [37] S.B. Pope;; M.S. Anand, *Flamelet and distributed combustion in premixed turbulent flames*, Proc. Combust. Inst., 20 (1985) 403-410.
- [38] F.A. Williams, *Combustion Theory*, Addison-Wesley, 1985.
- [39] K.N.C. Bray, *Turbulent Transport in Flames*, Proceedings of the Royal Society-Mathematical and Physical Sciences, 451 (1995) 231-256.
- [40] C.J. Mueller, J.F. Driscoll, D.L. Reuss, M.C. Drake, M.E. Rosalik, *Vorticity generation and attenuation as vortices convect through a premixed flame*, Combust. Flame, 112 (1998) 342-358.
- [41] A.M. Steinberg, J.F. Driscoll, *Straining and wrinkling processes during turbulence-premixed flame interaction measured using temporally-resolved diagnostics*, Combust. Flame, 156 (2009) 2285-2306.
- [42] N. Chakraborty, R.S. Cant, *Effects of Lewis number on turbulent scalar transport and its modelling in turbulent premixed flames*, Combust. Flame, 156 (2009) 1427-1444.
- [43] J.B. Bell, R.K. Cheng, M.S. Day, I.G. Shepherd, *Numerical simulation of Lewis number effects on lean premixed turbulent flames*, Proc. Combust. Inst., 31 (2007) 1309-1317.
- [44] A.N. Lipatnikov, J. Chomiak, *Lewis number effects in premixed turbulent combustion and highly perturbed laminar flames*, Combust. Sci. Technol., 137 (1998) 277-298.
- [45] A.J. Aspden, M.S. Day, J.B. Bell, *Characterization of low Lewis number flames*, Proc. Combust. Inst., 33 (2011) 1463-1471.

- [46] H. Carlsson, R.Yu, X.S. Bai, *Flame structure analysis for categorization of lean premixed CH<sub>4</sub>/air and H<sub>2</sub>/air flames at high Karlovitz numbers: Direct numerical simulation studies*, Proc. Combust. Inst., (2014) DOI: 10.1016/j.proci.2014.1009.1002.
- [47] G. Kychakoff, R.D. Howe, R.K. Hanson, M.C. Drake, R.W. Pitz, M. Lapp, C.M. Penney, *Visualization of Turbulent Flame Fronts with Planar Laser-Induced Fluorescence*, Science, 224 (1984) 382-384.
- [48] Z.S. Li, J. Kiefer, J. Zetterberg, M. Linvin, A. Leipertz, X.S. Bai, M. Alden, *Development of improved PLIF CH detection using an Alexandrite laser for single-shot investigation of turbulent and lean flames*, Proc. Combust. Inst., 31 (2007) 727-735.
- [49] B. Zhou, J. Kiefer, J. Zetterberg, Z.S. Li, M. Alden, *Strategy for PLIF single-shot HCO imaging in turbulent methane/air flames*, Combust. Flame, 161 (2014) 1566-1574.
- [50] J. Kiefer, B. Zhou, J. Zetterberg, Z.S. Li, M. Alden, *Laser-induced fluorescence detection of hot molecular oxygen in flames using an alexandrite laser*, Applied Spectroscopy, 68 (2014) 1266-1272.
- [51] C. Brackmann, O. Hole, B. Zhou, Z. Li, M. Alden, *Characterization of ammonia two-photo laser-induced fluorescence for gas-phase diagnostics*, Applied Physics B-Lasers and Optics, 115 (2014) 23-33.
- [52] Gregory P. Smith, David M. Golden, Michael Frenklach, Nigel W. Moriarty, Boris Eiteneer, Mikhail Goldenberg, C. Thomas Bowman, Ronald K. Hanson, Soonho Song, William C. Gardiner, V.V.L. Jr., Z. Qin, [http://www.me.berkeley.edu/gri\\_mech/](http://www.me.berkeley.edu/gri_mech/).
- [53] H.N. Najm, O.M. Knio, P.H. Paul, P.S. Wyckoff, *A study of flame observables in premixed methane - Air flames*, Combust. Sci. Technol., 140 (1998) 369.
- [54] H.N. Najm, P.H. Paul, C.J. Mueller, P.S. Wyckoff, *On the adequacy of certain experimental observables as measurements of flame burning rate*, Combust. Flame, 113 (1998) 312-332.
- [55] Z.M. Nikolaou, N. Swaminathan, *Heat release rate makers for premixed combustion*, Combust. Flame, 161 (2014) 3073-3084.
- [56] G.W. Adamson, X.S. Zhao, R.W. Field, *The HCO B<sup>2</sup>A'-X<sup>2</sup>A' System - Fluorescence Excitation and Stimulated-Emission Pumping Spectra*, Journal of Molecular Spectroscopy, 160 (1993) 11-38.
- [57] H.M. Yin, S.H. Kable, *Rotational analysis of the HCO B<sup>2</sup>A'-X<sup>2</sup>A' (1) 3<sub>1</sub><sup>1</sup> and 3<sub>2</sub><sup>1</sup> bands*, Journal of Molecular Spectroscopy, 237 (2006) 163-173.
- [58] J. Luque, D.R. Crosley, SRI International Report MP 99-009, 1999.

- [59] J.G. Calvert, Demerjia.Kl, R.D. Mcquigg, J.A. Kerr, *Photolysis of Formaldehyde as a Hydrogen-Atom Source in Lower Atmosphere*, Science, 175 (1972) 751-&.
- [60] J.D. Rogers, *Ultraviolet-Absorption Cross-Sections and Atmospheric Photodissociation Rate Constants of Formaldehyde*, Journal of Physical Chemistry, 94 (1990) 4011-4015.
- [61] C. Kullig, K. Dittmann, T. Wegner, I. Sheykin, K. Matyash, D. Loffhagen, R. Schneider, J. Meichsner, *Dynamics and Electronegativity of Oxygen RF Plasmas*, Contributions to Plasma Physics, 52 (2012) 836-846.
- [62] R. Toumi, B.J. Kerridge, J.A. Pyle, *Highly vibrationally Excited Oxygen as a Potential Source of Ozone in the Upper-Stratosphere and Mesosphere*, Nature, 351 (1991) 217-219.
- [63] N. Collings, J.A. Harris, K. Glover, *Estimating IC engine exhaust gas lambda and oxygen from the response of a universal exhaust gas oxygen sensor*, Measurement Science & Technology, 24 (2013).
- [64] W.G. Bessler, C. Schulz, V. Sick, J.W. Daily, *A versatile modeling tool for nitric oxide LIF spectra*, Proceedings of the Third Joint Meeting of the U.S. Sections of The Combustion Institute, (2003).
- [65] M. Balat, *Global Status of Biomass Energy Use*, Energy Sources Part a-Recovery Utilization and Environmental Effects, 31 (2009) 1160-1173.
- [66] J.A. Miller, C.T. Bowman, *Mechanism and Modeling of Nitrogen Chemistry in Combustion*, Prog. Energy Combust. Sci., 15 (1989) 287-338.
- [67] B.A. Williams, J.W. Fleming, *Comparative Species Concentrations in Ch<sub>4</sub>/O<sub>2</sub>/Ar Flames Doped with N<sub>2</sub>O, NO, and NO<sub>2</sub>*, Combust. Flame, 98 (1994) 93-106.
- [68] B.A. Williams, J.W. Fleming, *Comparison of Species Profiles between O<sub>2</sub> and NO<sub>2</sub> Oxidizers in Premixed Methane Flames*, Combust. Flame, 100 (1995) 571-590.
- [69] J. Luque, J.B. Jeffries, G.P. Smith, D.R. Crosley, *Combined cavity ringdown absorption and laser-induced fluorescence imaging measurements of CN(B-X) and CH(B-X) in low-pressure CH<sub>4</sub>-O<sub>2</sub>-N<sub>2</sub> and CH<sub>4</sub>-NO-O<sub>2</sub>-N<sub>2</sub> flames*, Combust. Flame, 126 (2001) 1725-1735.
- [70] X. Mercier, L. Pillier, J.F. Pauwels, P. Desgroux, *Quantitative measurement of CN radical in a low-pressure methane/air flame by cavity ring-down spectroscopy*, Comptes Rendus De L Academie Des Sciences Serie Iv Physique Astrophysique, 2 (2001) 965-972.
- [71] B. Zhou, C. Brackmann, Z. Li, M. Alden, *Development and application of CN PLIF for single-shot imaging in turbulent flames*, Combust. Flame, (2014) DOI: 10.1016/j.combustflame.2014.1007.1020.

- [72] P. Glarborg, A.D. Jensen, J.E. Johnsson, *Fuel nitrogen conversion in solid fuel fired systems*, Prog. Energy Combust. Sci., 29 (2003) 89-113.
- [73] W.Y. Li, K.C. Xie, *Energy Sources, Part A: Recovery, Utilization, and Environmental Effects Foreword*, Energy Sources Part a-Recovery Utilization and Environmental Effects, 31 (2009) 1591-1592.
- [74] C.M. Western., University of Bristol Research Data Repository, 2014.
- [75] M. Radojevic, *Reduction of nitrogen oxides in flue gases*, Environmental Pollution, 102 (1998) 685-689.
- [76] K. Kohsehoinghaus, *Laser Techniques for the Quantitative Detection of Reactive Intermediates in Combustion Systems*, Prog. Energy Combust. Sci., 20 (1994) 203-279.
- [77] G.W. Lee, B.H. Shon, J.G. Yoo, J.H. Jung, K.J. Oh, *The influence of mixing between NH<sub>3</sub> and NO for a De-NOx reaction in the SNCR process*, Journal of Industrial and Engineering Chemistry, 14 (2008) 457-467.
- [78] C. Brackmann, B. Zhou, Z.S. Li, M. Alden, *Strategies for Quantitative Planar Laser-Induced Fluorescence of NH Radicals in Flames*, Submitted to 9th Mediterranean Combustion Symposium, (2014).
- [79] R.N. Dixon, *The 0-0 and 1-0 Bands of the A(<sup>3</sup>Π<sub>v</sub>)-X(<sup>3</sup>Σ) System of NH*, Canadian Journal of Physics, 37 (1959) 1171.
- [80] C.R. Brazier, R.S. Ram, P.F. Bernath, *Fourier-Transform Spectroscopy of the A(<sup>3</sup>Π<sub>v</sub>)-X(<sup>3</sup>Σ) Transition of NH*, Journal of Molecular Spectroscopy, 120 (1986) 381-402.
- [81] J. Engstrom, J. Nygren, M. Alden, C.F. Kaminski, *Two-line atomic fluorescence as a temperature probe for highly sooting flames*, Optics Letters, 25 (2000) 1469-1471.
- [82] J. Nygren, J. Engstrom, J. Walewski, C.F. Kaminski, M. Alden, *Applications and evaluation of two-line atomic LIF thermometry in sooting combustion environments*, Measurement Science & Technology, 12 (2001) 1294-1303.
- [83] J. Winefordner, H.W. Latz, *Quantitative Study of Factors Influencing Sample Flow Rate in Flame Photometry*, Analytical Chemistry, 33 (1961) 1727.
- [84] J.H. Gibson, W.E. Grossman, W.D. Cooke, *Excitation Processes in Flame Spectrometry*, Analytical Chemistry, 35 (1963) 266.
- [85] Q.N. Chan, P.R. Medwell, P.A.M. Kalt, Z.T. Alwahabi, B.B. Dally, G.J. Nathan, *Solvent effects on two-line atomic fluorescence of indium*, Applied Optics, 49 (2010) 1257-1266.
- [86] D.V. Shenai-Khatkhate, R.L. DiCarlo, R.A. Ware, *Accurate vapor pressure equation for trimethylindium in OMVPE*, Journal of Crystal Growth, 310 (2008) 2395-2398.

- [87] N.M. Lakin, J.M. Brown, I.R. Beattie, P.J. Jones, *The Identification of Inoh in the Gas-Phase and Determination of Its Geometric Structure*, Journal of Chemical Physics, 100 (1994) 8546-8549.
- [88] B. Grundstrom, *Band spectrum of indium hydride*, Nature, 141 (1938) 555-555.
- [89] M.L. Ginter, *Band Spectrum of Inh Molecule - Characterization of  $A^3\Pi$  State*, Journal of Molecular Spectroscopy, 11 (1963) 301.
- [90] K.F. Freed, *On Hyperfine Structure of Inh and Theory of Hyperfine Structure of Molecules in Hunds Case (C)*, Journal of Chemical Physics, 45 (1966) 1714.
- [91] H.K. Kammler, L. Madler, S.E. Pratsinis, *Flame synthesis of nanoparticles*, Chemical Engineering & Technology, 24 (2001) 583-596.
- [92] P.H. Paul, *Vibrational-Energy Transfer and Quenching of OH  $A^2\Sigma^+(V'=1)$  Measured at High-Temperatures in a Shock-Tube*, Journal of Physical Chemistry, 99 (1995) 8472-8476.
- [93] M. Tamura, P.A. Berg, J.E. Harrington, J. Luque, J.B. Jeffries, G.P. Smith, D.R. Crosley, *Collisional quenching of CH(A), OH(A), and NO(A) in low pressure hydrocarbon flames*, Combust. Flame, 114 (1998) 502-514.
- [94] J.F. VERDIECK, P.A. BONCZYK, *Laser-induced saturated fluorescence investigations of CH, CN and NO in flames*, Proc. Combust. Inst., 18 (1981) 1559-1566.
- [95] C. Brackmann, J. Nygren, X. Bai, Z.S. Li, H. Bladh, B. Axelsson, I. Denbratt, L. Koopmans, P.E. Bengtsson, M. Alden, *Laser-induced fluorescence of formaldehyde in combustion using third harmonic Nd : YAG laser excitation*, Spectrochimica Acta Part a-Molecular and Biomolecular Spectroscopy, 59 (2003) 3347-3356.
- [96] T. Metz, X. Bai, F. Ossler, M. Alden, *Fluorescence lifetimes of formaldehyde ( $H_2CO$ ) in the A1A2-> X1A2 band system at elevated temperatures and pressures*, Spectrochimica Acta Part a-Molecular and Biomolecular Spectroscopy, 60 (2004) 1043-1053.
- [97] D.I. Shin, T. Dreier, J. Wolfrum, *Spatially resolved absolute concentration and fluorescence-lifetime determination of  $H_2CO$  in atmospheric-pressure  $CH_4$ /air flames*, Applied Physics B-Lasers and Optics, 72 (2001) 257-261.
- [98] C. Brackmann, J. Bood, M. Alden, G. Pengloan, O. Andersson, *Quantitative measurements of species and temperature in a DME-air counterflow diffusion flame using laser diagnostic methods*, Combust. Sci. Technol., 178 (2006) 1165-1184.
- [99] Y. Yamasaki, A. Tezaki, *Non-linear pressure dependence of A-state fluorescence lifetime of formaldehyde*, Applied Physics B-Lasers and Optics, 80 (2005) 791-795.

- [100] J.A. Sutton, J.F. Driscoll, *Rayleigh scattering cross sections of combustion species at 266, 355, and 532 nm for thermometry applications*, Optics Letters, 29 (2004) 2620-2622.
- [101] I. Namer, R.W. Schefer, *Error-Estimates for Rayleigh-Scattering Density and Temperature-Measurements in Premixed Flames*, Experiments in Fluids, 3 (1985) 1-9.
- [102] J.F. Driscoll, *Turbulent premixed combustion: Flamelet structure and its effect on turbulent burning velocities*, Prog. Energy Combust. Sci., 34 (2008) 91-134.
- [103] S.B. Pope, *Turbulent Flows*, Cambridge University Press, 2000.
- [104] D.J. Micka, J.F. Driscoll, *Stratified jet flames in a heated (1390 K) air cross-flow with autoignition*, Combust. Flame, 159 (2012) 1205-1214.
- [105] Y.C. Chen, N. Peters, G.A. Schneemann, N. Wruck, U. Renz, M.S. Mansour, *The detailed flame structure of highly stretched turbulent premixed methane-air flames*, Combust. Flame, 107 (1996) 223-244.
- [106] Y.C. Chen, M.S. Mansour, *Simultaneous Rayleigh scattering and laser-induced CH fluorescence for reaction zone imaging in high-speed premixed hydrocarbon flames*, Applied Physics B-Lasers and Optics, 64 (1997) 599-605.
- [107] W. Meier, X.R. Duan, P. Weigand, *Reaction zone structures and mixing characteristics of partially premixed swirling CH<sub>4</sub>/air flames in a gas turbine model combustor*, Proc. Combust. Inst., 30 (2005) 835-842.
- [108] M.J. Dunn, A.R. Masri, R.W. Bilger, *A new piloted premixed jet burner to study strong finite-rate chemistry effects*, Combust. Flame, 151 (2007) 46-60.
- [109] J.E. Temme, T.M. Wabel, A.W. Skiba, J.F. Driscoll, *Experimental investigation of premixed turbulent combustion in high reynolds number regimes using PLIF*, 52nd Aerospace Sciences Meeting, (2014).
- [110] J.A. Wunning, J.G. Wunning, *Flameless oxidation to reduce thermal NO-formation*, Prog. Energy Combust. Sci., 23 (1997) 81-94.
- [111] A. Cavaliere, M. de Joannon, *Mild combustion*, Prog. Energy Combust. Sci., 30 (2004) 329-366.
- [112] A.J. Aspden, M.S. Day, J.B. Bell, *Turbulence-Chemistry Interaction in Lean Premixed Hydrogen Combustion*, Proc. Combust. Inst., (2014) DOI: 10.1016/j.proci.2014.1008.1012.
- [113] H. Carlsson, R.Yu, X.-S. Bai, *Direct numerical simulation of lean premixed CH<sub>4</sub>/air and H<sub>2</sub>/air flames at high Karlovitz numbers*, International Journal of Hydrogen Energy, 2014 (2014) DOI: 10.1016/j.ijhydene.2014.1009.1173.
- [114] J. Sjoholm, J. Rosell, B. Li, M. Richter, Z.S. Li, X.S. Bai, M. Alden, *Simultaneous visualization of OH, CH, CH<sub>2</sub>O and toluene PLIF in a methane jet flame with varying degrees of turbulence*, Proc. Combust. Inst., 34 (2013) 1475-1482.

- [115] A. Fayoux, K. Zahringer, O. Gicquel, J.C. Rolon, *Experimental and numerical determination of heat release in counterflow premixed laminar flames*, Proc. Combust. Inst., 30 (2005) 251-257.
- [116] G. Hartung, J. Hult, C.F. Kaminski, J.W. Rogerson, N. Swaminathan, *Effect of heat release on turbulence and scalar-turbulence interaction in premixed combustion*, Physics of Fluids, 20 (2008).
- [117] S. Bockle, J. Kazenwadel, T. Kunzelmann, D.I. Shin, C. Schulz, J. Wolfrum, *Simultaneous single-shot laser-based imaging of formaldehyde, OH, and temperature in turbulent flames*, Proc. Combust. Inst., 28 (2000) 279-286.
- [118] P.R. Medwell, P.A.M. Kalt, B.B. Dally, *Simultaneous imaging of OH, formaldehyde, and temperature of turbulent nonpremixed jet flames in a heated and diluted coflow*, Combust. Flame, 148 (2007) 48-61.
- [119] C.C. Rasmussen, S.K. Dhanuka, J.F. Driscoll, *Visualization of flameholding mechanisms in a supersonic combustor using PLIF*, Proc. Combust. Inst., 31 (2007) 2505-2512.
- [120] B.O. Ayoolan, R. Balachandran, J.H. Frank, E. Mastorakos, C.F. Kaminski, *Spatially resolved heat release rate measurements in turbulent premixed flames*, Combust. Flame, 144 (2006) 1-16.
- [121] M. Roder, T. Dreier, C. Schulz, *Simultaneous measurement of localized heat-release with OH/CH<sub>2</sub>O-LIF imaging and spatially integrated OH\* chemiluminescence in turbulent swirl flames*, Proc. Combust. Inst., 34 (2013) 3549-3556.
- [122] J.H. Frank, S.A. Kaiser, M.B. Long, *Reaction-rate, mixture-fraction, and temperature imaging in turbulent methane/air jet flames*, Proc. Combust. Inst., 29 (2002) 2687-2694.
- [123] M.J. Dunn, A.R. Masri, R.W. Bilger, R.S. Barlow, *Finite Rate Chemistry Effects in Highly Sheared Turbulent Premixed Flames*, Flow Turbul. Combust., 85 (2010) 621-648.
- [124] D. Beerer, V. McDonell, P. Therkelsen, R.K. Cheng, *Flashback and Turbulent Flame Speed Measurements in Hydrogen/Methane Flames Stabilized by a Low-Swirl Injector at Elevated Pressures and Temperatures*, Journal of Engineering for Gas Turbines and Power-Transactions of the Asme, 136 (2014).
- [125] Y. Huang, V. Yang, *Dynamics and stability of lean-premixed swirl-stabilized combustion*, Prog. Energy Combust. Sci., 35 (2009) 293-364.
- [126] M.R. Johnson, D. Littlejohn, W.A. Nazeer, K.O. Smith, R.K. Cheng, *A comparison of the flowfields and emissions of high-swirl injectors and low-swirl injectors for lean premixed gas turbines*, Proc. Combust. Inst., 30 (2005) 2867-2874.
- [127] D. Littlejohn, A.J. Majeski, S. Tonse, C. Castaldini, R.K. Cheng, *Laboratory investigation of an ultralow NO<sub>x</sub> premixed combustion concept for industrial boilers*, Proc. Combust. Inst., 29 (2002) 1115-1121.

- [128] H. Carlsson, E. Nordström, A. Bohlin, Y. Wu, B. Zhou, Z.S. Li, M. Aldén, P.-E. Bengtsson, X.-S. Bai, *Numerical and Experimental study of Flame Propagation and Quenching of Lean Premixed Turbulent Low Swirl Flames at Different Reynolds Numbers*, Submitted to Combustion and Flame, (2014).
- [129] A. Bonaldo, J.B. Kelman, *Experimental annular stratified flames characterisation stabilised by weak swirl*, Combust. Flame, 156 (2009) 750-762.
- [130] K.J. Nogenmyr, P. Petersson, X.S. Bai, A. Nauert, J. Olofsson, C. Brackman, H. Seyfried, J. Zetterberg, Z.S. Li, M. Richter, A. Dreizler, M. Linne, M. Alden, *Large eddy simulation and experiments of stratified lean premixed methane/air turbulent flames*, Proc. Combust. Inst., 31 (2007) 1467-1475.
- [131] R.K. Cheng, I.G. Shepherd, B. Bedat, L. Talbot, *Premixed turbulent flame structures in moderate and intense isotropic turbulence*, Combust. Sci. Technol., 174 (2002) 29-59.
- [132] I.G. Shepherd, R.K. Cheng, *The burning rate of premixed flames in moderate and intense turbulence*, Combust. Flame, 127 (2001) 2066-2075.
- [133] T. Plessing, C. Kortschik, N. Peters, M.S. Mansour, R.K. Cheng, *Measurements of the turbulent burning velocity and the structure of premixed flames on a low-swirl burner*, Proc. Combust. Inst., 28 (2000) 359-366.
- [134] H. Carlsson, E. Nordström, A. Bohlin, P. Petersson, Y. Wu, R. Collin, M. Aldén, P.-E. Bengtsson, X.-S. Bai, *Large eddy simulations and rotational CARS/PIV/PLIF measurements of a lean premixed low swirl stabilized flame*, Combust. Flame, 161 (2014) 2539-2551.
- [135] K.J. Nogenmyr, C. Fureby, X.S. Bai, R. Petersson, R. Collin, M. Linne, *Large eddy simulation and laser diagnostic studies on a low swirl stratified premixed flame*, Combust. Flame, 156 (2009) 25-36.
- [136] A. Bohlin, E. Nordstrom, H. Carlsson, X.S. Bai, P.E. Bengtsson, *Pure rotational CARS measurements of temperature and relative O<sub>2</sub>-concentration in a low swirl turbulent premixed flame*, Proc. Combust. Inst., 34 (2013) 3629-3636.
- [137] B. Zhou, C. Brackmann, Q. Li, Z. Wang, P. Petersson, Z.S. Li, M. Alden, X.-S. Bai, *Distributed reactions in highly turbulent premixed methane/air flames Part 1: Flame structure characterization*, Combust. Flame, in press, 2014.
- [138] P.D. Ronney, B.D. Haslam, N.O. Rhys, *Front Propagation Rates in Randomly Stirred Media*, Physical Review Letters, 74 (1995) 3804-3807.
- [139] M.J. Dunn, A.R. Masri, R.W. Bilger, R.S. Barlow, G.H. Wang, *The compositional structure of highly turbulent piloted premixed flames issuing into a hot coflow*, Proc. Combust. Inst., 32 (2009) 1779-1786.
- [140] C.C. Huang, S.S. Shy, C.C. Liu, Y.Y. Yan, *A transition on minimum ignition energy for lean turbulent methane combustion in flamelet and distributed regimes*, Proc. Combust. Inst., 31 (2007) 1401-1409.

- [141] S.S. Shy, W.T. Shih, C.C. Liu, *More on minimum ignition energy transition for lean premixed turbulent methane combustion in flamelet and distributed regimes*, Combust. Sci. Technol., 180 (2008) 1735-1747.
- [142] S.S. Shy, C.C. Liu, W.T. Shih, *Ignition transition in turbulent premixed combustion*, Combust. Flame, 157 (2010) 341-350.
- [143] A.J. Aspden, J.B. Bell, S.E. Woosley, *Distributed Flames in Type Ia Supernovae*, Astrophysical Journal, 710 (2010) 1654-1663.
- [144] A.J. Aspden, M.S. Day, J.B. Bell, *Turbulence-flame interactions in lean premixed hydrogen: transition to the distributed burning regime*, Journal of Fluid Mechanics, 680 (2011) 287-320.
- [145] A.J. Aspden, M.S. Day, J.B. Bell, *Lewis number effects in distributed flames*, Proc. Combust. Inst., 33 (2011) 1473-1480.
- [146] J. Savre, H. Carlsson, X.S. Bai, *Tubulent Methane/Air Premixed Flame Structure at High Karlovitz Numbers*, Flow Turbul. Combust., 90 (2013) 325-341.
- [147] A.S. Verissimo, A.M.A. Rocha, M. Costa, *Experimental study on the influence of the thermal input on the reaction zone under flameless oxidation conditions*, Fuel Processing Technology, 106 (2013) 423-428.
- [148] A.S. Verissimo, A.M.A. Rocha, M. Costa, *Importance of the inlet air velocity on the establishment of flameless combustion in a laboratory combustor*, Experimental Thermal and Fluid Science, 44 (2013) 75-81.
- [149] A.E.E. Khalil, A.K. Gupta, *Swirling flowfield for colorless distributed combustion*, Applied Energy, 113 (2014) 208-218.
- [150] V.K. Arghode, A.K. Gupta, K.M. Bryden, *High intensity colorless distributed combustion for ultra low emissions and enhanced performance*, Applied Energy, 92 (2012) 822-830.
- [151] A.E.E. Khalil, A.K. Gupta, *Distributed swirl combustion for gas turbine application*, Applied Energy, 88 (2011) 4898-4907.
- [152] Y. Minamoto, T.D. Dunstan, N. Swaminathan, R.S. Cant, *DNS of EGR-type turbulent flame in MILD condition*, Proc. Combust. Inst., 34 (2013) 3231-3238.
- [153] M. Kopp, M. Brower, O. Mathieu, E. Petersen, F. Guthe, *CO<sub>2</sub>\* chemiluminescence study at low and elevated pressures*, Applied Physics B-Lasers and Optics, 107 (2012) 529-538.
- [154] S. Krishnamurthy, H.P. Broida, *Effect of Molecular Oxygen on Emission Spectra of Atomic Oxygen-Acetylene Flames*, Journal of Chemical Physics, 34 (1961) 1709-&c.

- [155] K.H. Becker, D. Haaks, Tatarczy.T, *Natural Lifetime of Oh (2Σ, ν=0, N=2, J=3/2) and Its Quenching by Atomic-Hydrogen*, Chemical Physics Letters, 25 (1974) 564-567.
- [156] E.M. Bulewicz, P.J. Padley, R.E. Smith, *Spectroscopic Studies of C2, Ch and Oh Radicals in Low Pressure Acetylene+Oxygen Flames*, Proceedings of the Royal Society of London Series a-Mathematical and Physical Sciences, 315 (1970) 129-&c.
- [157] C.T. Bowman, D.J. Seery, *Chemiluminescence in High-Temperature Oxidation of Methane*, Combust. Flame, 12 (1968) 611-&c.
- [158] S.W. Yoo, C.K. Law, S.D. Tse, *Chemiluminescent OH\* and CH\* flame structure and aerodynamic scaling of weakly buoyant, nearly spherical diffusion flames*, Proc. Combust. Inst., 29 (2002) 1663-1670.
- [159] S. Matsuda, J.R. Marquart, D. Gutman, D.J. Fife, I.R. Slagle, *Shock-Tube Study of Acetylene-Oxygen Reaction .4. Kinetic Study of Ch, C2, and Continuum Chemiluminescence during Induction Period*, Journal of Chemical Physics, 57 (1972) 5277-&c.
- [160] C.W. Hand, G.B. Kistiakowsky, *Ionization Accompanying Acetylene-Oxygen Reaction in Shock Waves*, Journal of Chemical Physics, 37 (1962) 1239-&c.
- [161] J. Grebe, K.H. Homann, *Blue-Green Chemi-Luminescence in the System C2H2/O/H - Formation of the Emitters CH(A2-Δ), C2(d<sup>3</sup>Π<sub>g</sub>) and C2H*, Berichte Der Bunsen-Gesellschaft-Physical Chemistry Chemical Physics, 86 (1982) 587-597.
- [162] G.P. Smith, C. Park, J. Schneiderman, J. Luque, *C-2 Swan band laser-induced fluorescence and chemiluminescence in low-pressure hydrocarbon flames*, Combust. Flame, 141 (2005) 66-77.
- [163] A. Ratner, J.F. Driscoll, J.M. Donbar, C.D. Carter, J.A. Mullin, *Reaction zone structure of non-premixed turbulent flames in the "Intensely Wrinkled" regime*, Proc. Combust. Inst., 28 (2000) 245-252.
- [164] Y. Minamoto, N. Swaminathan, *Scalar gradient behaviour in MILD combustion*, Combust. Flame, 161 (2014) 1063-1075.
- [165] J. Sidey, E. Mastorakos, *Visualization of MILD combustion from jets in cross-flow*, Proc. Combust. Inst., 35 (2015) 3537-3545.

# Summary of papers

## Paper I

We demonstrated the feasibility of high-quality single-shot interference-free HCO PLIF in turbulent methane/air flames using a multi-mode alexandrite laser. Conditions to which the present HCO PLIF technique can be applied have been clarified to avoid potential interferences from OH, O<sub>2</sub>, CH<sub>2</sub>O and PAH.

*I conducted experiments together with Johannes Kiefer, and I evaluated experimental data and wrote the manuscript. Others contributed to improve the manuscript.*

## Paper II

A strategy of detecting vibrationally excited O<sub>2</sub> molecule have been developed using a multi-mode alexandrite laser. The possibility for single-shot imaging of hot O<sub>2</sub> has also been demonstrated.

*I conducted experiments together with Johannes Kiefer, and I also contributed to the data evaluation. Johannes Kiefer wrote the manuscript. Others contributed to improve the manuscript.*

## Paper III

This paper reported the development of single-shot CN PLIF and its application in turbulent flames. An improved detection of CN radicals by a factor of 4 has been achieved with the employment of an alexandrite laser in comparison to the conventional dye laser. Broadening and local quenching of the CN layer have been observed in NH<sub>3</sub>-doped CH<sub>4</sub>/air flame.

*The idea of this experiment was initiated through discussion with Marcus Aldén and Zhongshan Li. The experiments were conducted by Christian Brackmann and me. I evaluated experimental data with the help of Christian Brackmann and I wrote the manuscript. Others contributed to improve the manuscript.*

## Paper IV

Characteristics of NH<sub>3</sub> two-photon LIF were investigated, including the excitation-detection scheme, and the dependence of LIF signal on temperature, laser irradiance and pressure. NH<sub>3</sub> distribution in turbulent NH<sub>3</sub>/CH<sub>4</sub>/air flames was visualized using two-photon PLIF simultaneously with CH PLIF for flame front identification.

*I contributed to the simultaneous PLIF measurement of NH<sub>3</sub> and CH together with Christian Brackmann. Christian Brackmann prepared the manuscript, in which I contributed with the part concerning CH measurement.*

## Paper V

A series of LUPJ flames has been investigated by three sets of simultaneous measurements, i.e. CH/CH<sub>2</sub>O/OH set, HCO/CH<sub>2</sub>O/OH set and T/CH<sub>2</sub>O/OH set. Distributed reactions achieved through rapid turbulence mixing were experimentally evidenced for the first time in turbulent premixed flames by the observations of broadened/distributed CH/HCO layer.

*I initiated the idea through discussion with Xue-song Bai. Christian Brackmann and I conducted the experiment. I evaluated the data and prepared the manuscript, and others contributed to it.*

## Paper VI

In addition to the experimental datasets demonstrated in Paper V, LDA measurements were performed to characterize the flow fields of LUPJ flames. The flame structures characteristics and correlations between measured scalars were analyzed in detail. Temperature was shown to be important to sustain distributed reactions, and rapid turbulence transport of radicals was found to be responsible for the occurrence of distributed reactions.

*Qing Li, Zhenkan Wang and I were responsible for LDA measurements. Qing Li evaluated the LDA data to which I also contributed. Christian Brackmann was responsible for CH<sub>2</sub>O spectroscopic simulations to be used for quantification of CH<sub>2</sub>O LIF signal to which I also contributed. I performed CHEMKIN simulations and analyzed the PLIF datasets. I wrote the manuscript. Others contributed to improve the manuscript.*

## Paper VII

Based on the multi-scalar imaging measurements demonstrated in Paper V, the flame structures and correlations between measured scalars in small scales down to 100  $\mu\text{m}$  were illustrated. A possible onset of CH layer broadening was captured and analyzed in detail. The potential of utilizing the multi-scalar imaging system to investigate the small-scale turbulence was discussed.

*The idea was brought up through discussion with Zhongshan Li. Christian Brackmann and I conducted the experiment. I evaluated the data and prepared the manuscript, and others contributed to it.*

## Paper VIII

Multi-scalar imaging (i.e. OH/CH<sub>2</sub>O, CH/OH, CH/CH<sub>2</sub>O) was conducted on low-swirl stabilized lean premixed flames (LSFs). The investigated LSFs were found to span over multiple combustion regimes (i.e. the corrugated flamelet regime, the TRZ regime and the DRZ regime) as evidenced by distinctive changes on the structures of the CH layer. Distributed CH was observed at downstream locations of LSFs. Local quenching of distributed CH layer was also observed due to cold ambient air entrainment. Consistent with the results on LUPJ flames, temperature above  $\sim 1000$  K was shown to be important for the realization of distributed reactions. This provides the other evidence in addition to the one from LUPJ flames that distributed reactions can be a common combustion mode.

*I initiated the idea and conducted measurements with Qing Li and Yong He. Per Petersson contributed to setting up the low-swirl burner. I evaluated the data and prepared the manuscript, and others contributed to it.*

## Paper IX

Strategy for PLIF of NH radicals in flames with the possibility of quantification was developed and demonstrated. NH spectroscopic simulations were performed to facilitate quantification of NH LIF signal. Simultaneous broadening and thinning of the NH layers in turbulent NH<sub>3</sub> flames were observed.

*Christian Brackmann and I conducted the experiment. Christian Brackmann analyzed the experimental data, and I performed the CHEMKIN simulation used for signal quantification. Christian Brackmann prepared the manuscript, in which I contributed to the discussion sections.*